Decision-support strategies to improve radiotherapy outcomes in prostate and gynecological cancer treatment planning

by

Susan Dang
B.Sc., University of Waterloo, 2020

A Thesis Submitted in Partial Fulfillment of the
Requirements for the Degree of

MASTER OF SCIENCE

in the Department of Physics and Astronomy

We acknowledge and respect the Lək̓ʷəŋən (Songhees and Xʷsepsəm/ Esquimalt) Peoples on whose territory the university stands, and the Lək̓ʷəŋən and W̱SÁNEĆ Peoples whose historical relationships with the land continue to this day.

Decision-support strategies to improve radiotherapy outcomes in prostate and gynecological cancer treatment planning

by

Susan Dang
B.Sc., University of Waterloo, 2020

Supervisory Committee

Dr. Manuel Rodriguez Vega, Main Supervisor
(Medical Physics Department, BC Cancer - Victoria)

Dr. Magdalena Bazalova-Carter, Co-Supervisor
(Department of Physics and Astronomy, University of Victoria)

Dr. Isabelle Gagné, Departmental Member
(Medical Physics Department, BC Cancer - Victoria)

Dr. Ibrahim Numanagić, External Member
(Department of Computer Science, University of Victoria)

ABSTRACT

Effective radiotherapy treatment depends on delivering a sufficient dose to the tumour to kill all cancer cells while minimizing radiation exposure to surrounding healthy tissues and nearby sensitive structures known as organs at risk (OARs). Achieving this balance is particularly important in prostate and gynecological cancers where critical structures are located in close proximity to the target. This thesis investigates decision-support strategies that aim to improve the robustness, precision, and overall quality of radiotherapy treatment plans. The research focuses on two clinically distinct applications of radiotherapy involving low-dose rate (LDR) prostate brachytherapy and external beam radiation therapy (EBRT) for gynecological cancers.

In the LDR prostate brachytherapy component, an in-house dose engine was used to simulate seed placement uncertainties associated with procedural variability during implantation. Based on these simulations, the software calculated the probabilities of achieving pre-implant dosimetric constraints, including the planning target volume (PTV) receiving 150% of the prescription dose (PTV V150%) and global coverage metrics. These probabilities were then used to determine threshold values predictive of achieving one of the post-implant objectives, prostate D90%, defined as the dose received by 90% of the prostate volume. The resulting thresholds provided a quantitative framework for assessing plan robustness and guiding data-informed adjustments prior to treatment.

In the EBRT component, the dose gradient optimization performance of the Normal Tissue Objective (NTO) and Concentric Ring Structures (CRS) was systematically evaluated in gynecological cancer treatment plans. Both methods achieved clinical constraints for target coverage and OAR sparing. The NTO demonstrated consistent and reliable performance, while CRS provided enhanced flexibility in shaping the dose gradient in anatomically complex scenarios. These findings contribute to treatment planning by informing the selection of optimization strategies based on case complexity and clinical priorities.

These findings contribute to the development of robust, data-informed planning strategies tailored to the clinical and anatomical challenges of prostate and gynecological cancer radiotherapy treatment. By guiding adjustments to planned seed

placement in LDR brachytherapy and informing dose gradient optimization in EBRT planning, they address the critical need to balance effective tumour coverage with the protection of OARs, ultimately improving plan quality and supporting more consistent patient care.

Contents

List of Tables

List of Figures

ACKNOWLEDGMENTS

I would like to sincerely thank my supervisor, **Dr. Manuel Rodriguez Vega**, for his support and for providing me with the opportunity to pursue graduate studies. His willingness to believe in my potential and offer me a place in the program made it possible for me to undertake this work. I am deeply grateful for the opportunity to complete my studies under his supervision. It is a chapter of my academic journey that I will always look back on with gratitude, as it has left a lasting impact and offered me a chance to grow in ways I will always value.

I would also like to extend my sincere thanks to my committee members, **Dr. Magdalena Bazalova-Carter, Dr. Ibrahim Numanagić, and Dr. Isabelle Gagné**, for their time, guidance, and support throughout the course of this thesis, as well as during my time in the program. Their thoughtful feedback and encouragement were truly appreciated.

I would like to express my appreciation to the **Department of Medical Physics at BC Cancer Victoria** and the **Medical Physics Program at the University of Victoria** for providing a welcoming and collaborative environment throughout my time in the program. I am grateful for the sense of community and the many opportunities for learning and growth that I experienced during my time here. It was a privilege to be part of a community where everyone, including **clinical staff, administrative and technical teams, and my peers in the program**, contributed to a shared commitment to improving patient care. I am especially thankful for the support, kindness, and guidance I received, as well as the friendship and collaboration that made my experience truly meaningful.

To the **Radiation Therapy Service Technicians** and **Catherine Lava**, thank you for bringing lightness to long days and for sharing good food and humour. Most of all, thank you for the subtle reminders, sometimes spoken and sometimes delivered with a perfectly timed eyebrow raise, to stay flexible.

Chapter 1

Introduction

Cancer remains one of the most serious health threats facing the global population, with millions of new cases diagnosed every year. In Canada alone, an estimated 247 100 people were expected to be diagnosed with cancer in 2024, amounting to nearly 675 new cases each day. Over the course of a lifetime, about two in five Canadians are projected to receive a cancer diagnosis, a trend that is expected to continue into 2025.[1,2] Among these many cases, prostate and gynecological cancers are a particular concern. Prostate cancer is the most commonly diagnosed cancer among men, while gynecological cancers, which include ovarian, cervical, endometrial, and uterine cancers, also pose a substantial threat to women's health.[3] Although they occur less frequently than prostate cancer, gynecological cancers are often diagnosed at advanced stages, which can lead to poorer prognoses and fewer treatment options. Given the impact of these cancers, implementing effective treatment strategies is essential not only for improving survival rates but also for enhancing the quality of life of those affected.[4,5] Among the various treatment options available, including surgery and chemotherapy, radiation therapy, often referred to radiotherapy, plays a central role in the treatment of both prostate and gynecological cancers.

Radiation therapy involves the use of ionizing radiation to destroy cancer cells. It can be delivered externally through external beam radiation therapy (EBRT), which uses a linear accelerator (linac) to direct radiation beams at the tumour from outside the body, or internally through brachytherapy, where sealed radioactive sources are placed inside or near the tumour using needles and specialized applicators. In radi-

ation therapy, a key challenge lies in delivering sufficient dose to the tumour while protecting nearby organs at risk (OARs) and healthy tissue. This challenge is especially critical in prostate and gynecological cancers, where multiple OARs are located in close proximity to the tumour. Achieving this balance requires careful treatment planning to ensure that the radiation dose is delivered to the tumour while minimizing exposure to surrounding structures. Despite careful planning, radiation therapy can be limited by dose delivery uncertainties or by the need to compromise between tumour coverage and OAR sparing. These challenges are important considerations during the planning process, as both can significantly affect the quality of the final dose distribution. In particular, anatomical variation, organ motion, and procedural limitations may introduce dose deviations that compromising accuracy and consistency. Additionally, efforts to ensure adequate tumour coverage often result in higher dose to surrounding OARs, especially in anatomically complex regions like the pelvis, where small deviations can increase the risk of OAR toxicity and reduce tumour control. As a result, ongoing research continues to refine planning strategies that improve the precision, robustness, and effectiveness of radiation therapy.

This thesis aims to address these challenges through the investigation and refinement of radiotherapy treatment planning strategies in both prostate and gynecological cancers. In low dose rate (LDR) prostate brachytherapy, sealed radioactive sources come in the form of small seeds that are placed inside the prostate to deliver targeted radiation. Deviations between the planned and actual seed placement can affect dose coverage within the tumour and increase the risk of unnecessary dose to OARs. To evaluate and improve the robustness of these plans, an in-house software tool was used to simulate seed positional uncertainties and assess their impact on dosimetry metrics. In EBRT for gynecological cancers, the proximity of OARs to the tumour requires careful control of dose gradients. This work explores the use of dose gradient optimization tools, including normal tissue objectives and concentric ring structures, to enhance dose conformity and improve OAR sparing. Together, these efforts aim to contribute to the integration of decision-support tools and optimization strategies that enhance the safety, consistency, and effectiveness of radiation therapy treatment plans.

The remainder of this thesis is organized as follows. Chapter 2 provides background information on radiation therapy treatment planning, including key concepts

and techniques relevant to both areas of investigation. Chapter 3 presents the robustness evaluation in LDR prostate brachytherapy utilizing the in-house software to simulate seed placement deviations. Chapter 4 describes the dose gradient optimization work in gynecological cancers treated with EBRT. Finally, Chapter 5 summarizes the findings and discusses the clinical implications and future directions of this research.

Chapter 2

Background

2.1 Principles of Radiation Therapy

Radiation therapy is a common cancer treatment modality that uses ionizing radiation to damage the deoxyribonucleic acid (DNA) of tumour cells, the molecule responsible for carrying their genetic instructions and regulating replication. This damage impairs the tumour cells' ability to divide and survive, ultimately leading to their destruction. Ionizing radiation, which includes electromagnetic radiation such as X-rays and gamma rays, as well as charged particles like electrons, penetrate the body and interact with atoms to cause ionization. This ionization process involves the ejection of electrons from their atomic orbits, producing ions and free electrons. These free electrons can go on to cause further ionizations as they travel through tissue causing atoms and molecules to become chemically unstable, which can lead to their DNA damage.[6] The cumulative energy transferred through these ionization events results in dose deposition, a critical factor in achieving therapeutic outcomes. In radiation therapy, ionizing radiation induces cellular damage through direct or indirect ionization mechanisms. Indirect ionization is typically associated with electromagnetic radiation, which transfers energy to atoms, resulting in the ejection of free electrons that subsequently cause further ionizations. In contrast, direct ionization involves charged particles that interact directly with atomic electrons, causing ionization through Coulomb interactions.[6–8] A thorough understanding of the following processes and interactions are essential for accurate treatment planning, enabling

clinicians to predict how radiation will behave in different tissues and to optimize dose delivery.

2.1.1 Photon Interactions

Photons are commonly used in radiation therapy and achieve both diagnostic and therapeutic effects through indirect ionization. As photons pass through tissue, their intensity is reduced due to absorption or scattering, also known as attenuation. This process can be described quantitatively by the attenuation coefficient, μ, which represents the probability of photon interaction per unit distance in a material.[7] This attenuation occurs as photons interact with atoms in the body, which contributes to the production of high-energy secondary electrons. These electrons are responsible for depositing dose and damaging cancerous tissue. The generation of secondary electrons occurs primarily through three major interactions: the photoelectric effect, Compton scattering, and pair production. The probability of each interaction depends on both the energy of the photon and the atomic number (Z) of the absorbing material.[6–8] This relationship is illustrated in Figure 2.1, which shows how the dominant photon interaction across atomic number and photon energies ranging from kiloelectronvolts (keV) to megaelectronvolts (MeV).[8]

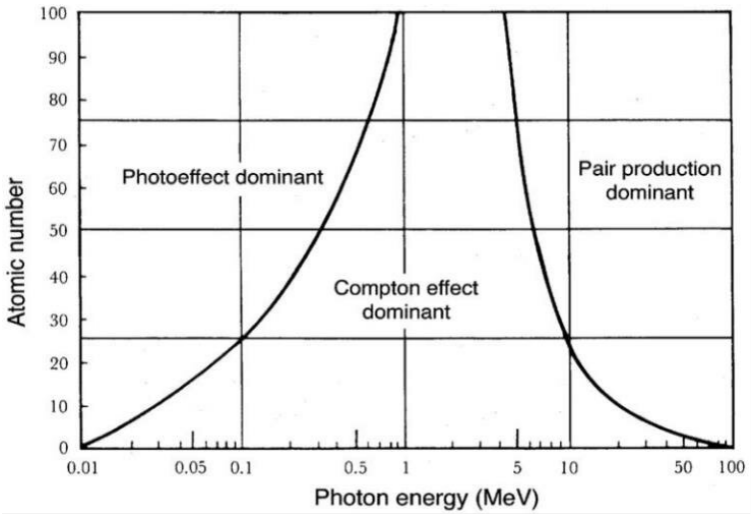

Figure 2.1: Interaction dominance of photons by atomic number and energy. Dominance regions of photon interactions in matter, showing the energy ranges and atomic numbers of the absorbing material where the photoelectric effect, Compton scattering, or pair production are most likely to occur.[8]

2.1.1.1 Photoelectric Effect

The photoelectric effect occurs when a photon is completely absorbed by an atom, resulting in the ejection of an inner-shell electron. Atoms contain electrons arranged in discrete energy levels known as shells, labeled K, L, M or N, starting from the innermost shell (K) and moving outward. These shells represent regions of increasing energy, with the K-shell electrons being the most tightly bound to the nucleus. When a photon interacts with an atom, its energy can be transferred to an electron in one of these inner shells, ejecting it from the atom as a photoelectron. The energy transferred to the electron can be quantified by the equation:

$$E_{\text{Transferred}} = h\nu - E_{\text{Binding}} \tag{2.1}$$

where $h\nu$ is the photon incident energy and E_{Binding} is the binding energy of shell to which the electron is ejected from.[6,8]

Following ejection, the resulting vacancy may be filled by an electron from a higher-energy shell. This de-excitation process leads to the emission of characteristic X-rays, which are specific to the element and providing insight into its atomic structure. Alternatively, these characteristic X-rays may be reabsorbed within the atom, transferring its energy to another outer-shell electron and ejecting it as an Auger electron.[6,8]

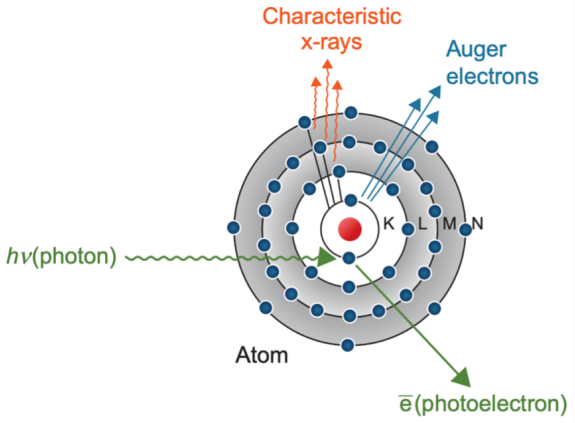

Figure 2.2: Photoelectric effect process. An incident photon transfers its energy to an inner-shell electron, ejecting it as a photoelectron. The resulting vacancy is filled by an higher energy-shell electron, releasing either characteristic X-rays or Auger electrons. [6]

The probability of the photoelectric effect occurring is highly dependent on the atomic number (Z) of the material and the energy (E) of the incident photons. The mass attenuation coefficient for photoelectric is proportional to the ratio, Z^3/E^3, indicating that the effect is more likely with higher atomic numbers and lower photon energies (provided the photon energy is equal to or greater than the binding energy of the electron's shell).[8] This strong dependence on atomic number and photon energy makes the photoelectric effect the dominant interaction at the low photon energies typically used in diagnostic imaging. Its sensitivity to atomic number is particularly important for producing high-contrast images, as tissues with different atomic compositions such as soft tissue and bone, have varying probabilities of photon absorption.[7]

2.1.1.2 Compton Scattering

Compton scattering occurs when a photon interacts with a loosely bound outer shell electron, where the photon's energy and momentum are partially absorbed by this electron. This results in the electron to be ejected out if its orbit as a Compton electron and scattered at an angle, θ, resulting in ionization. Meanwhile, the photon is scattered from the atom at a reduced energy and different angle, ϕ. The reduced energy of the scattered photon, $h\nu'$, can be quantified as:[6]

$$h\nu' = \frac{h\nu}{1 + \alpha(1 - \cos\phi)} \tag{2.2}$$

where hv is the incident photon energy and $\alpha = \frac{h\nu}{m_0 c^2}$ is the rest energy of the electron (0.511 MeV). The kinetic energy of the Compton electron can be defined as:[6]

$$E = h\nu \cdot \frac{\alpha(1 - \cos\phi)}{1 + \alpha(1 - \cos\phi)} \tag{2.3}$$

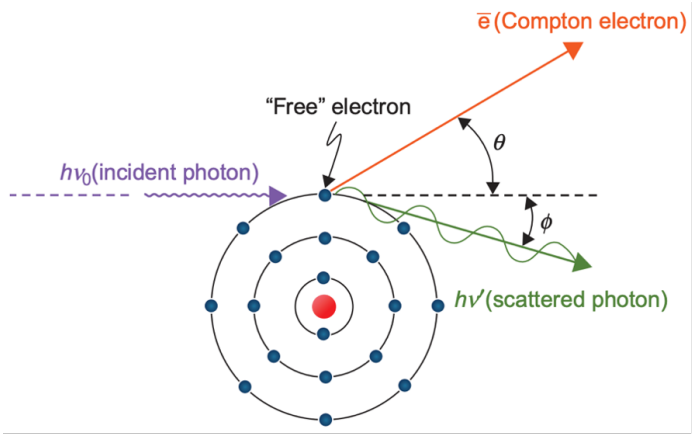

Figure 2.3: Compton scattering process.An incident photon collides with a loosely bound electron, ejecting it as a Compton electron and scattering the photon at a lower energy. [6]

In Compton scattering, the probability of this interaction occurring is largely dependent on the energy of the incident photon rather than the atomic number of the material. However, the density of the material and the electron density also contribute to the likelihood of this interaction.[7] This is because materials with higher densities have a greater number of electrons per unit volume, increasing the chances of photon-electron interactions. While this interaction can occur at all energy ranges, it becomes the predominant interaction at medium to high energies where the photon is less likely to be fully absorbed by the photoelectric effect, leaving it with sufficient energy for repeated scattering events.[8] Compton scattering is the predominant interaction at diagnostic and therapeutic photon energies ranging from approximately 30 keV to 30 MeV in low atomic number (low-Z) tissues such as water and soft tissue.[9]

2.1.1.3 Pair Production

Pair production occurs when a photon with an energy of at least 1.022 MeV interacts with the electromagnetic field of an atomic nucleus, resulting in the creation of an electron-positron pair. As the photon approaches the nucleus, it transfers all of its energy to generate a negatively charged electron (e^-) and a positively charged positron (e^+). These particles are emitted in opposite directions, each receiving a portion of the photon's excess energy, quantified by the equation:

$$E_{\text{Transferred}} = h\nu - 1.022 \text{ MeV} \tag{2.4}$$

where $h\nu$ is the incident photon energy and 1.022 MeV is the combined rest mass energy of the electron-positron pair. The resulting particles then traverse the surrounding medium, losing energy through interactions such as ionization, excitation, and bremsstrahlung radiation. Eventually, the positron interacts with a free electron, producing two annihilation photons (gamma-ray photons), each with an energy of 511 keV, emitted in opposite directions.[6]

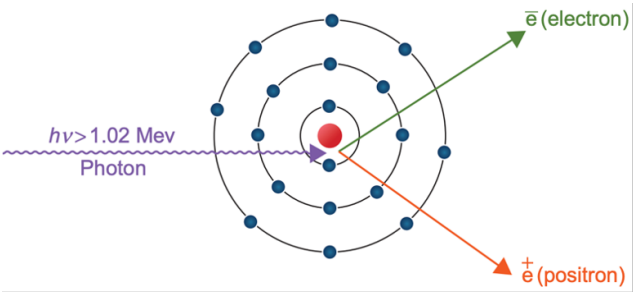

Figure 2.4: Pair production process. A high-energy photon interacts with the atomic nucleus and converts into an electron and a positron.[6]

The probability of pair production depends not only on photon energy but also significantly on the atomic number of the absorbing material. Specifically, it increases proportionally to the square of the atomic number (Z^2), as higher-Z nuclei produce stronger electromagnetic fields that enhance the likelihood of interaction.[8] This effect becomes especially pronounced at photon energies in the greater megaelectron range.

2.1.2 Electron Interactions

Understanding electron interactions is essential in radiation therapy, as electrons contribute to energy deposition in tissue through both direct and indirect mechanisms. In this context, these terms refer to the physical processes by which radiation deposits energy in matter, and should not be confused with the radiobiological concepts of direct and indirect effects, which describe the pathways of DNA damage. As a form of directly ionizing radiation, electrons interact with biological tissue primarily through Coulomb forces, leading to the excitation or ionization of atoms. These electrostatic

interactions displace or excite atomic electrons, resulting in energy deposition. Electrons also play a key role in indirect ionization, which occurs when uncharged photons interact with matter to produce secondary electrons. These secondary electrons then deposit energy in tissue through the same ionization processes.[6]

These electron interactions can be further understood through their types of collisions with tissue atoms. Elastic collisions occur when electrons scatter without significant energy loss, merely changing direction. In contrast, inelastic collisions involve energy transfer to atoms, leading to excitation or ionization, which are processes critical for therapeutic effects. In radiotherapy, it is these inelastic collisions, especially those causing ionization, that are primarily responsible for biological damage within tumour tissues.[6,7]

The extent to which electrons deposit energy as they traverse tissue is described by stopping power, which represents the rate of energy loss per unit path length and is a key parameter for quantifying dose deposition in radiation therapy. The stopping power depends on the electron's kinetic energy, as well as the atomic number and electron density of the medium. The Bethe-Bloch equation provides the foundational basis for calculating stopping power by accounting for the energy loss through its interactions with matter. This energy loss plays a central role in shaping the therapeutic dose delivered to tissue. Additionally, the stopping power consists of two components known as collision stopping power and radiative stopping power. Collision stopping power arises from interactions with orbital electrons, resulting in ionization and excitation, while radiative stopping power results from interactions with atomic nuclei, leading to bremsstrahlung radiation. In most therapeutic energy ranges, collision stopping power is the dominant mechanism, whereas radiative losses become significant primarily at high energies. These interactions will be further discussed in the following sections. [6,8]

2.1.2.1 Collisional Interactions

Collisional interactions occur when incident electrons interact with the orbital electrons of atoms in the medium through Coulomb forces, resulting in energy transfer leading to excitations or ionizations.[8] These interactions can be classified as either soft or hard collisions based on the impact parameter, which is the distance of the

electron from the atom relative to the atomic radius.[10]

In the case of soft collisions, where the incident electron passes an atom at a considerable distance (electron distance from the atom > atomic radius), the interaction may result in the excitation of an atomic electron to a higher energy level.[8] The excited atomic electron eventually returns to its ground state, emitting a photon with energy corresponding to the difference between the electron shells involved (Figure 2.5). Meanwhile, incident electron continues on its path but with reduced energy, having lost a few electron volts (eV) to the atomic electron.[10]

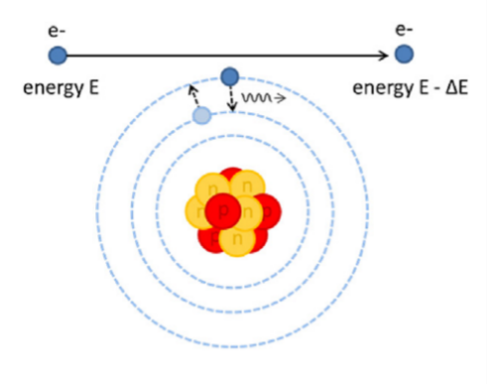

Figure 2.5: Soft collision process causing excitation. An incident electron transfers part of its energy to an atomic electron, exciting it to a higher energy level.[10]

In hard collisions, an electron passing close to an atom can interact with one of its atomic electrons (electron distance from the atom ≈ atomic radius).[8] This close proximity allows the incident electron to transfer a significant portion of its kinetic energy to the atomic electron, effectively ejecting it from its shell and causing ionization. As a result, the incident electron continues on its path but in a different direction, and with reduced energy (Figure 2.6). This type of interaction typically results in more significant tissue damage due to the higher energy transfer involved.[8,10]

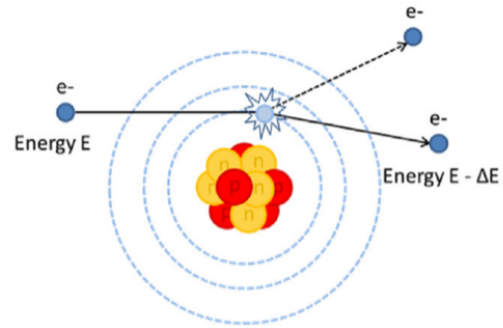

Figure 2.6: Hard collision process causing ionization. An incident electron transfers sufficient energy to eject an atomic electron, resulting in ionization.[10]

The likelihood and intensity of collisional interactions are significantly influenced by the impact parameter, electron energy, and the atomic material's atomic number. Soft collisions, occurring at larger impact parameters, are more frequent due to less stringent alignment requirements between the electron and the atom. Higher electron energies enhance the likelihood and intensity of both soft and hard collisions by allowing electrons to penetrate deeper and increasing their interactions with atomic electrons causing significant damage to tissues. Similarly, greater atomic numbers increase the likelihood and intensity of these collisions due to stronger electromagnetic forces that attract and interact with the electrons more effectively.[6,10]

2.1.2.2 Radiative Interactions

In radiative interactions, electrons lose energy by emitting photons. When an electron passes sufficiently close to the nucleus (electron distance from the atom $<$ atomic radius), the Coulomb fields of the nucleus and the electron interact, causing the electron's path to be deflected.[6,10] While this scenario most often results in elastic scattering, a small percentage of these encounters lead to inelastic scattering. In these instances, the rapid deceleration of the electron causes it to lose energy, which is then emitted as a photon, a process known as Bremsstrahlung, or breaking radiation (Figure 2.7). The energy of the emitted photon can range up to the kinetic energy of the incident electron. The likelihood of radiative interactions occurring increases with the square of the atomic number (Z^2) of the nucleus and also increases with the

electron's energy.[10]

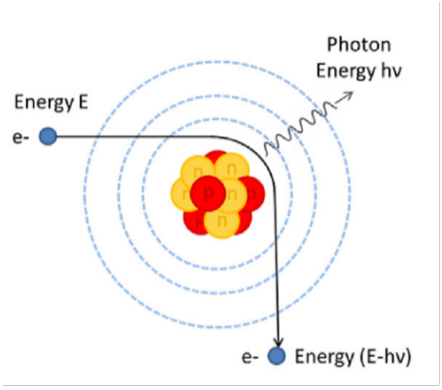

Figure 2.7: Radiative interaction process leading to Bremsstrahlung radiation. An incident electron closely passes by the electric field of the nucleus, emitting a photon in the form of Bremsstrahlung radiation.[10]

2.2 Radiation Therapy Modalities

The foundation of radiation therapy as a medical treatment was established shortly after Wilhem Conrad Roentgen's discovery of X-rays in 1895, where one of the earliest documented clinical applications occurred in 1896, when American physician Emil Grubbe reportedly used X-rays to treat a patient with breast cancer.[11] This marked the early beginnings of what would evolve into external beam radiation (EBRT). The following discovery of radioactivity by Henri Becquerel later that year paved the way for further advances in therapeutic radiation, including the isolation of radium by Pierre and Marie Curie in 1898. The use of radium as a radiation source was soon explored and showed promise in treating conditions like lupus and cancer, introducing the foundational principles of brachytherapy.[12] These early innovations initiated the clinical and technological evolution of radiation therapy, leading to more refined and targeted radiation delivery methods. Advances such as imaging guidance and dose modulation have facilitated modern approaches to be tailored to the tumour location and patient-specific factors, ensuring precise treatment while sparing healthy tissues. The following sections will describe the current implementation and techniques associated with both brachytherapy and EBRT.

2.2.1 Brachytherapy

Brachytherapy, also referred to as internal radiation therapy, involves the placement of sealed radioactive sources directly within or adjacent to the tumour, where the radiation travels a short distance. By positioning the radiation source close to or inside the target volume, brachytherapy enables highly localized dose delivery with rapid dose fall-off, effectively treating the tumour while minimizing exposure to surrounding healthy tissues.[13,14] The steep dose falloff around the source is a defining characteristic of this technique and is governed by physical principles that make brachytherapy particularly effective for treating well-localized tumours.

In brachytherapy, radiation is delivered using radioactive isotopes that emit radiation as they decay over time. The rate of this radioactive decay is characterized by the activity of the source, measured in becquerels (Bq), which describes the number of disintegrations per second. The activity decreases exponentially over time according to the radioactive decay law:

$$A(t) = A_0 \cdot e^{-\lambda t} \tag{2.5}$$

where $A(t)$ is the activity at time t, A_0 is the initial activity, and λ is the decay constant. The decay constant, used to describe how quickly the radioactive source undergoes decay, is calculated as:

$$\lambda = \frac{\ln(2)}{T_{1/2}} \tag{2.6}$$

with $T_{1/2}$ representing the source's half-life.[6] The half-life determines how long the source remains therapeutically active and directly influences the duration of dose delivery in brachytherapy. Understanding this relationship is essential for determining the appropriate isotope based on the desired dose rate and treatment duration. Short-lived isotopes with high initial activity are useful when rapid dose delivery is needed, while long-lived isotopes provide prolonged dose exposure over extended periods.[15]

A defining principle in brachytherapy is the inverse square law, which describes how radiation intensity decreases proportionally to the square of the distance from the source:

$$\text{Intensity} \propto \frac{1}{r^2} \tag{2.7}$$

where r is the distance from the source.[14] This relationship enables high-dose delivery near the source while rapidly sparing surrounding tissues, a critical advantage of brachytherapy in anatomical sites where tumours are adjacent to sensitive structures.

Brachytherapy techniques are generally classified into high-dose rate (HDR) and low-dose rate (LDR) approaches, based on the rate at which radiation is delivered and the duration of source placement. HDR brachytherapy delivers high doses over short periods, typically a few minutes per fraction, where a fraction refers to a single treatment session in a multi-session course, using a temporarily inserted high activity source. In contrast, LDR brachytherapy involves the permanent implantation of low-activity sources which emit radiation continuously over an extended duration ranging from several weeks to a few months, depending on the isotope's half-life and continue to remain in the body even after the majority of radioactive decay has occurred.[13–15] The remainder of this section will focus on LDR brachytherapy based on the work presented in the thesis.

In addition to the activity and half-life of the radioactive isotopes, the photon energy also determines their clinical suitability by influencing tissue penetration, treatment duration, and dose distribution.[6,8] Photon energy affects how deeply radiation can penetrate tissue. Isotopes that emit lower-energy photons are advantageous for treating localized tumours, as the dose remains confined to the immediate area. In LDR brachytherapy, the most commonly used isotopes include iodine-125 (^{125}I), palladium-103 (^{103}Pd), and cesium-131 (^{131}Cs). Iodine-125 emits photons at approximately 28 keV and has a half-life of about 60 days, making it well suited for slowly proliferating tumours such as prostate cancer.[15–17] Palladium-103 has a shorter half-life of 17 days and emits photons around 21 keV, allowing for a faster dose delivery, often preferred for more aggressive disease.[18,19] Cesium-131 emits photons at approximately 30 keV and has a half-life of 9.7 days, offering even more rapid dose delivery and is increasingly used in specific anatomical sites such as ocular or intracranial tumours.[17,20]

LDR brachytherapy is most commonly used in the treatment of localized prostate cancer.[16,17] The procedure is typically performed under general anesthesia and transperineally, in which needles are inserted into the prostate under real-time guidance with transrectal ultrasound (TRUS). A template grid is used to guide needle positioning, and radioactive seeds (individually or in stranded or linked configurations) are

deposited into the prostate according to a pre-implant treatment plan.[17] In some cases, additional seeds, referred to as non-planned supplemental seeds (NPSS), may be implanted at the discretion of the radiation oncologist to improve dose coverage in specific areas.[21] After the procedure, patients recover from the anesthesia and are usually discharged the same day.[17]

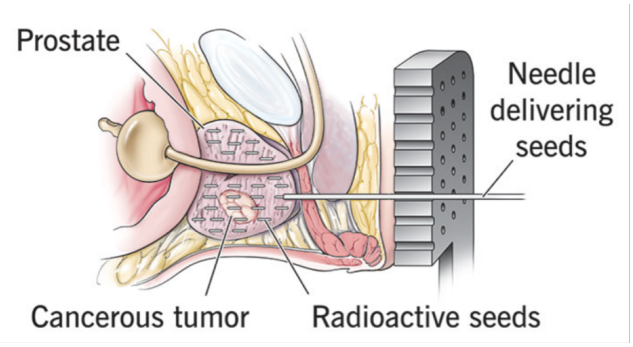

Figure 2.8: Low-dose rate prostate brachytherapy procedure. Radioactive seeds are implanted directly into the prostate using needles inserted through a grid template.[22]

The total radiation dose delivered in LDR brachytherapy results from the cumulative contribution of all implanted seeds. Dose calculations are performed using the TG-43 dosimetry protocol, a standardized formalism that models how radiation is distributed around each source based on its physical and geometric characteristics.[8,23] Further discussion of TG-43 implementation, dosimetric evaluation, and treatment planning will be presented in subsequent sections of this thesis.

2.2.2 External Beam Radiation Therapy (EBRT)

EBRT is the most common form of radiation therapy used to treat various cancers. It is a non-invasive method of delivering high-energy ionizing radiation to the tumour site from outside the patient's body. EBRT is typically delivered in multiple fractions, a process known as fractionation, where the total prescribed dose is divided into smaller doses (fractions) delivered over a series of treatment sessions. This approach allows normal tissues time to repair between treatments while maintaining effective tumour control. The prescribed dose refers to the total amount of radiation recommended by the radiation oncologist to achieve therapeutic effect, usually measured in

Gray (Gy) or centigray (cGy). The specific fractionation regimen depends on tumour type, location, and patient-specific considerations.[6–8]

EBRT is commonly delivered using a linear accelerator, a machine that generates either high-energy photon or electron beams. The process begins with an electron gun, which serves as the source of electrons. It contains a heated cathode filament that releases electrons by heating the metal surface, causing electrons to escape due to increased thermal energy. These electrons are then accelerated toward a focusing anode by a high-voltage potential difference, forming a focused, high-speed electron beam. This electron stream is injected into an accelerating waveguide, where it is further accelerated by microwave energy to reach megavoltage energies suitable for therapeutic applications. The accelerated electrons are then directed by a bending magnet toward a high atomic number (Z) target, typically tungsten, producing high-energy X-rays through bremsstrahlung interactions. The resulting photon beam is shaped to conform to the target volume using a series of components. It first passes through a primary collimator to define the maximum field size and reduce stray radiation. A flattening filter is used to create a uniform dose profile by attenuating the central beam region, whereas flattening filter-free (FFF) mode omits the filter to achieve higher dose rates for specific treatments. After this stage, the beam passes through a monitor ionization chamber, which measures the dose output in real-time and ensures consistent and accurate dose delivery throughout treatment. The beam then reaches the secondary collimation system, which includes jaws and a multi-leaf collimator (MLC). The jaws are movable metal blocks that define the rectangular boundaries of the treatment field and provide additional shielding while the MLC, composed of motorized tungsten leaves that adjust dynamically to match the target's shape. The shaped beam exits the gantry and is directed towards the patient surface.[6,7,24]

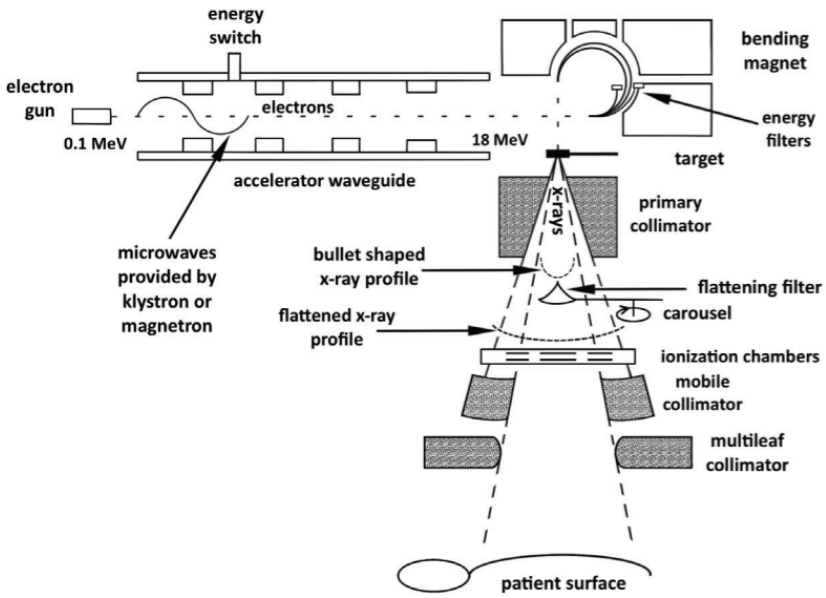

Figure 2.9: Linear accelerator schematic diagram. A high-energy electron beam is accelerated and directed onto a target to produce X-rays, which are shaped and modulated before reaching the patient.[24]

Photon beam energies used in EBRT typically range from 4 MV to 25 MV, with higher energies providing greater tissue penetration and improved percent depth dose (PDD) shown in Figure 2.10.[6,8] Beam energy selection is guided by the depth of the tumour and the surrounding anatomical structures to achieve an optimal therapeutic balance. Lower-energy beams (6 MV) are typically used for superficial or moderately deep targets, as they deposit a higher dose closer to the surface, reducing exposure to deeper tissues. Higher-energy beams (15 to 18 MV) are preferred for deep-seated tumours due to their increased penetration and improved dose uniformity across the target volume.[25] This relationship is characterized by the percent depth dose (PDD), which describes the percentage of the maximum dose delivered at a given depth in tissue relative to the dose at a reference point (typically the depth of maximum dose). PDD curves are used to evaluate how the dose falls off with increasing depth and help determine the appropriate beam energy to ensure adequate coverage of the target while minimizing dose to overlying and adjacent healthy tissues.[6,8]

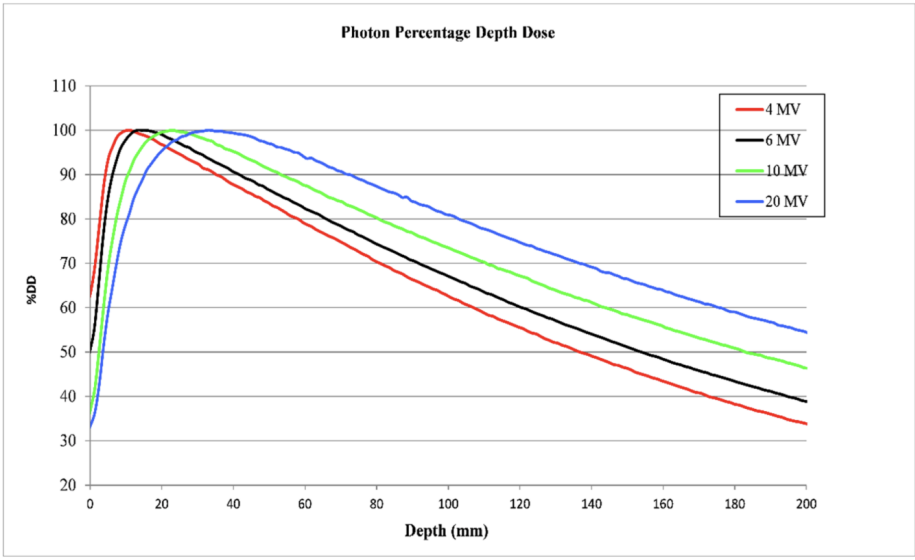

Figure 2.10: Percent depth dose curves for various MV photon beams. Percent depth dose (PDD) distributions in water for a $10\times10\text{cm}^2$ field using 4, 6, 10, and 20 MV photon beams.[26]

Several beam delivery techniques have been developed in EBRT to improve the precision and conformity of dose distributions. Early techniques such as three-dimensional conformal radiation therapy (3D-CRT) use a small number of fixed, stationary beams shaped to the target volume.[27] As technology evolved, more advanced methods like intensity-modulated radiation therapy (IMRT) introduced the ability to modulate beam intensity across each field, allowing for greater control over dose gradients and improved sparing of adjacent organs at risk.[27–29]

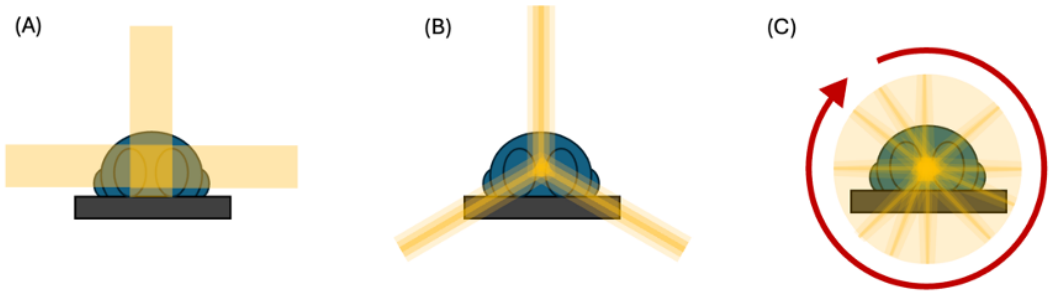

Figure 2.11: External beam radiation therapy techniques. (A) three-dimensional conformal radiation therapy delivers uniform beams from multiple fixed angles. (B) Intensity modulated radiation therapy (IMRT) varies beam intensity across angles for improved dose conformity. (C) Volumetric modulated arc therapy (VMAT) delivers modulated dose continuously as the gantry rotates around the patient.

VMAT delivers radiation in a continuous arc as the gantry rotates up to 360° around the patient. During rotation, the beam shape, dose rate, and gantry speed are simultaneously modulated to deliver a highly conformal dose distribution.[30] This dynamic coordination allows VMAT to sculpt dose with greater flexibility using one or more arcs, compared to fixed-beam techniques. VMAT is particularly well-suited for treating complex target volumes, such as irregularly shaped tumours or those adjacent to critical structures, as seen in gynecological cancers, where steep dose gradients are essential to spare surrounding organs at risk.[31,32] However, the delivery complexity of VMAT requires more sophisticated treatment planning and optimization processes. These aspects of VMAT planning will be discussed in detail in the next section.

2.3 Radiation Therapy Treatment Planning

Radiotherapy treatment planning is essential in cancer care, providing a strategic framework that guides the accurate delivery of radiation across various treatment modalities. The purpose of treatment planning is to devise a strategy that delivers precise radiation doses to the tumour, while simultaneously protecting the surrounding healthy tissues and OARs from unnecessary exposure. The general process of treatment planning begins with detailed imaging to map out the tumour's location and the surrounding anatomy. Based on this imaging, the radiation oncologist (RO)

delineates the target volumes and critical organs at risk. This allows for the development of plans where dose distributions are specifically configured and optimized to achieve the desired therapeutic outcomes, ensuring that each plan is precisely tailored to the individual patient's anatomy and cancer characteristics. Following this, the treatment plan undergoes a thorough evaluation and must be formally approved by the RO before treatment delivery can begin. An overview of this process is illustrated in Figure 2.12. In the following sections, each step of the treatment planning process is explored in more detail. Although these steps are broadly applicable to various types of radiotherapy, the focus is specifically on their implementation in LDR prostate brachytherapy and EBRT for gynecological cancers, detailing the considerations and techniques used in these contexts.

Figure 2.12: Radiation therapy treatment plan workflow. The treatment planning process begins with imaging, followed by delineation of structures, plan design and optimization, evaluation, and final approval by the radiation oncologist (RO).

2.3.1 Medical Imaging

Imaging scans are used to determine the exact location, size, and shape of the tumour, as well as to identify nearby OARs. This information is essential for assessing patient eligibility, selecting appropriate treatment techniques, and determining optimal patient positioning. Common imaging modalities include computed tomography (CT), magnetic resonance imaging (MRI), ultrasound (US), and positron emission tomography (PET), each offering unique advantages depending on the clinical context. By providing a detailed anatomical reference, these images serve as the foundation for developing precise and effective radiotherapy treatment plans.

2.3.1.1 Ultrasound Imaging

In LDR prostate brachytherapy, a volume study is the first step in the treatment planning process, serving to accurately characterize the patient's anatomy and guide seed placement for optimal dose delivery. It provides essential information such as the size, shape, and location of the prostate relative to surrounding critical structures, influencing the number of radioactive seeds required and their spatial distribution. Additionally, the volume study is used to determine the patient's eligibility for treatment by assessing pubic arch interference, which may impede needle access during the implant procedure.[33,34] This study is typically performed using transrectal ultrasound (TRUS) imaging, which captures axial images of the prostate, urethra, and rectum. These images are then used to generate a pre-operative plan that serves as the foundation for the treatment.

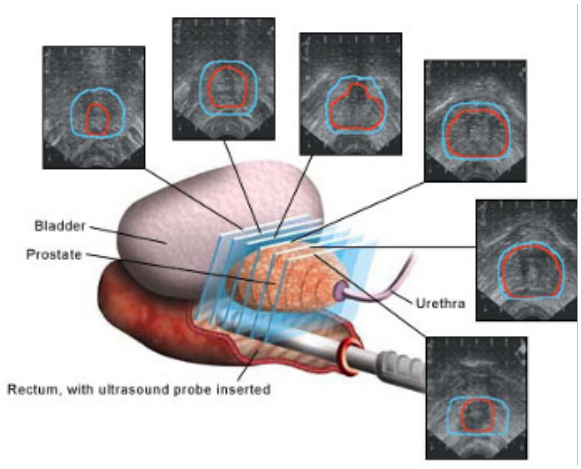

Figure 2.13: Volume study for prostate imaging. Transrectal ultrasound is used to acquire cross-sectional images of the prostate, which are used to determine the prostate's volume and shape for treatment planning.

TRUS imaging relies on fundamental principles of ultrasound (US) physics to visualize internal structures such as the prostate, urethra, and rectum. The technique uses a transducer containing piezoelectric crystals that generate high-frequency sound waves when an electrical current is applied.[35] These ultrasound waves are emitted in short bursts and can be referred to as pulses, rather than continuous waves. These US waves, typically in the range of 4 to 10 megahertz (MHz)for prostate imaging, traveling through the body at various speeds depending on tissue density.[36,37] For

soft tissue, the speed is approximately 1540 m/s.[35] As these US waves propagate through the tissue, they may be reflected, refracted, scattered or attenuated at tissue interfaces with different acoustic properties. Among these interactions, reflection is the most critical for image formation. The extent to which a wave is reflected depends on the difference in acoustic impedance between two adjacent tissues. The acoustic impedance, Z, of a medium is defined as:

$$Z = p \cdot c \tag{2.8}$$

where p is the density of the tissue and c is the speed of sound in the tissue.[35,38] When an US wave encounters an interface with different acoustic impedances, a portion of the wave is reflected back toward the transducer, also known as an echo. The intensity reflection coefficient R, which quantifies the fraction of the incident wave that is reflected, is given by:

$$R = \left(\frac{Z_2 - Z_1}{Z_2 + Z_1} \right)^2 \tag{2.9}$$

where Z_1 and Z_2 are the acoustic impedances of two mediums. Larger differences in impedance result in stronger reflections and brighter signals on the ultrasound image.[38]

To generate a B-mode image, also known as brightness mode or two-dimensional US, the transducer emits ultrasound pulses in multiple directions across the imaging field. This is accomplished either mechanically, by rotating the transducer, or electronically, by steering the ultrasound beam using different elements within the transducer array. Each pulse produces a scan line that represents tissue information along that specific direction. The reflected pulses, or echoes, are received by the transducer and converted back into electrical signals, where real-time images are constructed based on the timing and amplitude of these echoes. The time delay between the pulse and echo determines the depth of the reflecting interface, while the amplitude of the echo influences the brightness of each pixel in the final image. Stronger echoes from dense or highly reflective tissues appear brighter, whereas weaker echoes produce darker pixels, resulting in a two-dimensional grayscale image that conveys tissue contrast and anatomical boundaries.[39]

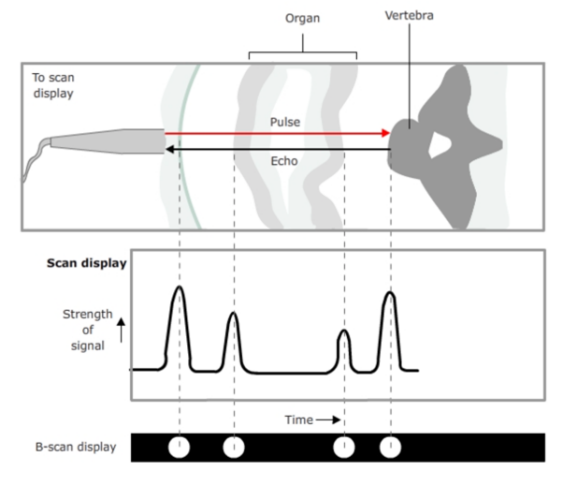

Figure 2.14: Ultrasound B-mode imaging diagram. A pulse of ultrasound is transmitted into tissue, and echoes from different structures are detected and converted into brightness-modulated signals to form a two-dimensional image.[40]

2.3.1.2 Computed Tomography

Computed tomography (CT), commonly referred to as a CT scan, is a widely used imaging modality in radiotherapy planning, providing detailed anatomical visualization and density information essential for accurate treatment planning and design. CT imaging is based on the attenuation of X-rays and the reconstruction of images using computer algorithms. These reconstructed images form the foundation for planning tasks such as structure delineation and dose distribution calculations.

The imaging process begins with X-ray production inside an X-ray tube, which operates using principles similar to linear accelerator-generated radiation but at significantly lower photon energies in the kiloelectronvolt range.[41] In the X-ray tube, a heated filament at the cathode emits electrons through thermionic emission, which are then accelerated across a high voltage potential toward a rotating anode. The anode is composed of tungsten due to its high atomic number (Z = 74), which increases the efficiency of X-ray production though bremsstrahlung interactions and is high melting point to withstand the heat generated during repeated exposure.[6,42] The resulting X-ray spectrum contains a range of photon energies and undergoes filtration to remove low-energy photons that lack sufficient penetrating capabilities, also referred to as beam hardening. This improves image quality and reduces unnecessary radiation

exposure. After filtration, the beam is collimated and directed to the patient.[42]

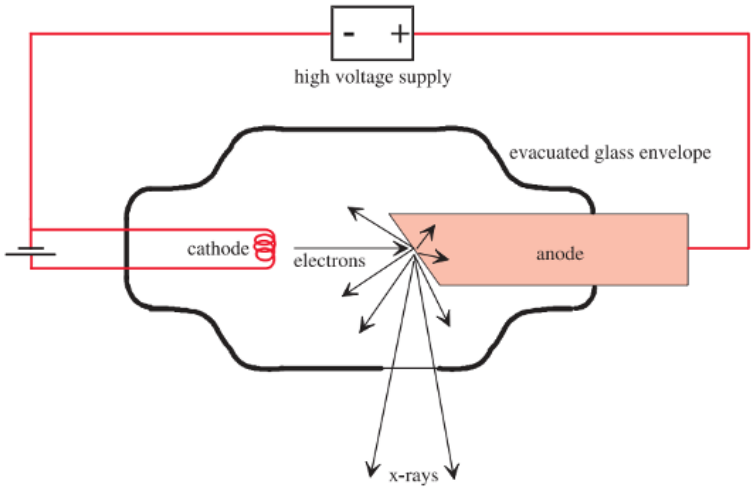

Figure 2.15: X-ray tube schematic diagram. Electrons are emitted from the heated cathode are accelerated toward the anode by a high voltage supply, producing X-rays upon impact.[42]

As X-rays pass through the body, they undergo attenuation primarily due to photoelectric absorption and Compton scattering. The extent of attenuation is described by the linear attenuation coefficient (μ), which depends on the tissue's density, atomic number, and the energy of the incident photons. Higher energy photons are less attenuated, while denser tissues and higher atomic numbers increase attenuation, producing contrast between anatomical structures for image formation.[6]

The attenuated X-ray beam is detected by an array of solid-state detectors positioned opposite the X-ray source. Each detector unit consists of a scintillator, a photodiode, and readout electronics. The scintillator, typically made of high atomic number (Z) materials such as gadolinium oxysulfide (Gd_2O_2S) or cesium iodide (CsI), efficiently absorbs incoming X-ray photons and re-emits the energy as visible light.[43,44] This light is then converted into an electrical signal by the underlying photodiode. The attached electronics collect and digitize these signals where the resulting values reflect the degree of X-ray attenuation along each path through the patient.[43] As the X-ray source and detector array rotate around the patient, electrical signals generated by the attenuated X-ray beam are collected from multiple angles, forming projection data for the reconstruction of individual image slices. By translating the patient couch incrementally through the gantry of the CT, multiple cross-sectional slices can

be acquired sequentially along the body, facilitating full volumetric imaging.

The intensity of the detected signal can be characterized by the exponential attenuation law:

$$I = I_0 e^{-\left(\sum_{i=1}^{n} \mu_i x\right)} \tag{2.10}$$

where I_0 is the initial x-ray intensity signal, I is the signal intensity detected after passing through the patient, μ is the linear attenuation coefficient of the tissue, and x is the tissue thickness. These signals then undergo preprocessing where the measured intensities are converted into line integrals of attenuation coefficients using a logarithmic transformation:

$$p = \ln\left(\frac{I}{I_0}\right) = x\sum_{i=1}^{n} \mu_i \tag{2.11}$$

where p is the projection data corresponding to the x-ray path, I is the detected intensity, and I_0 is the initial intensity.[42] This preprocessing step results in the sum of the linear attenuation coefficients along the x-ray path which are then used in image reconstruction algorithms to generate cross-sectional images of the patient's internal anatomy (Figure 2.16).[42,45]

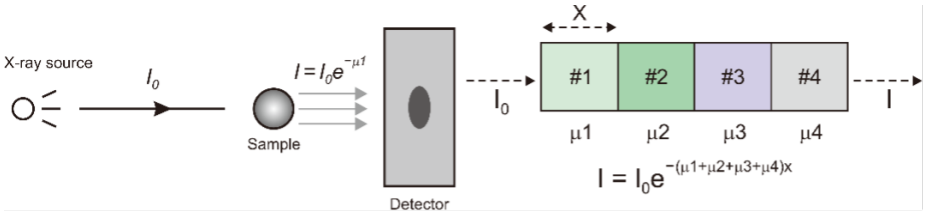

Figure 2.16: Computed tomography signal detection process. An x-ray beam passes through and is attenuated based on the linear attenuation coefficients of the tissues. The transmitted intensity is measured by the detector and used to reconstruct the internal structures.[43]

The CT image reconstruction step combines projection data acquired from multiple angles to generate a final image representing internal anatomy. A commonly used reconstruction method is Filtered Back Projection (FBP), which consists of two main steps, filtering followed by back projection.[42] Filtering is applied first to correct for blurring caused by overlapping intensity contributions during back projection. Without this step, projecting the raw data along the original X-ray paths produces a low

contrast image.

During filtering, each projection is transformed into the frequency domain using the Fourier transform to analyze the frequency components contributing to image detail. A convolution kernel known as a ramp filter is then applied to enhance high-frequency details such as edges while suppressing low-frequency components that cause blurring. This sharpening step is essential for restoring image clarity.[46,47] After filtering, the data are returned to the spatial domain using the inverse Fourier transform. In the back projection step, these filtered projections are distributed back across the image plane along their original X-ray paths. This is repeated for all projection angles, resulting in reconstruction of the attenuation map of the scanned slice.[46–48]

To visualize these differences in tissue density, the attenuation values are converted into Hounsfield Units (HU), a standardized scale used in CT imaging. HU values quantify the attenuation of tissues relative to water, allowing for consistent visualization and differentiation of anatomical structures. The HU for a specific voxel at location (x, y, z) is calculated using the following formula:

$$\mathrm{HU}_{(x,y,z)} = 1000 \times \frac{\mu_{(x,y,z)} - \mu_{\mathrm{water}}}{\mu_{\mathrm{water}}} \tag{2.12}$$

where $\mu_(x, y, z)$ is the linear attenuation coefficient at the voxel location (x, y, z), and μ_{water} is the linear attenuation coefficient for water, which is defined as 0 HU. The Hounsfield scale typically ranges from -1000 HU for air to +1000 HU for bone.[6] This scale allows for clear distinction between tissues such as bone, soft tissue, fat, and air, enhancing the clarity and utility of CT images for treatment planning. The final CT image is displayed in grayscale, with varying shades representing different HU values corresponding to tissue densities.

2.3.2 Structure Delineations

In radiotherapy, the process of delineating structures on imaging datasets is a critical step that significantly influences treatment planning and outcomes. This process involves ROs manually identifying and contouring both tumours and nearby OARs. While traditionally performed manually, recent advancements have seen the imple-

mentation of automated methods, enhancing the efficiency and consistency of this process.[49,50] Accurate identification and delineation of these structures are crucial as they directly impact the efficacy and safety of the treatment. Errors in this process can lead to underdosing of the tumour, potentially resulting in insufficient treatment, or overdosing of OARs, which can increase the risk of toxicity. Moreover, these contours are patient-specific and tailored to the site of the cancer, ensuring that each treatment plan is precisely customized to address the unique challenges presented by each patient's condition.

2.3.2.1 Target Definitions

Contouring the tumour alone is not sufficient for effective radiation therapy due to natural variations in patient anatomy and the potential spread of cancer cells beyond the visible tumour boundaries. To address these challenges, margins are added to the delineated tumour volume. These margins account for movements and microscopic extensions of the cancer, ensuring all potentially affected areas are included in the treatment plan. These considerations are formalized into specific target volumes as established by the International Commission on Radiation Units and Measurements (ICRU), including the gross tumour volume (GTV), clinical target volume (CTV), internal target volume (ITV), and planning target volume (PTV). These target volumes are designed to ensure precise and effective radiation delivery, accounting for the dynamic nature of tumour behavior and patient movement throughout the course of treatment.[51,52] The GTV represents the visible or clinically detectable tumour, as identified on imaging or through clinical examination. The CTV includes the GTV along with a margin for microscopic disease extension, accounting for subclinical tumour spread that may not be visible on images.[51] The ITV accounts for variability in target position due to physiological movements, such as bladder filling or organ motion.[52] The PTV expands the CTV and ITV further to account for setup uncertainties, ensuring that the prescribed dose is consistently delivered to the intended target.[51,52]

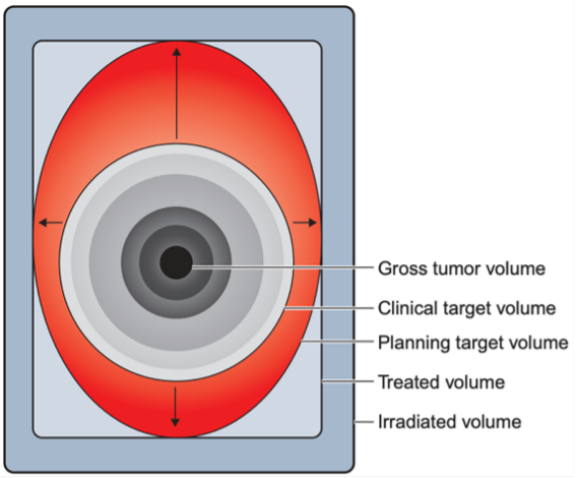

Figure 2.17: Target volumes in radiotherapy. Schematic representation of the gross tumour volume (GTV), clinical target volume (CTV), planning target volume (PTV), treated volume, and irradiated volume as defined by ICRU Report 50.

2.3.2.2 Organs at Risk (OARs)

In addition to defining target volumes, radiation therapy planning also requires careful consideration of the OARs which include healthy tissues and organs that are sensitive to radiation and are located near the treatment area. Accurate identification and protection of these structures are essential to minimize treatment-related side effects and maintain the patient's quality of life. The specific OARs considered vary by treatment site, reflecting the anatomical complexity and varying radiation sensitivities of OARs in different tumour sites.

2.3.2.2.1 OARs for Prostate Cancer

In prostate treatment using LDR brachytherapy, the primary OARs are the urethra and rectum due to their anatomical proximity to the prostate and their susceptibility to radiation exposure from permanently implanted radioactive seeds.[53] The urethra, which runs directly through the center of the prostate, is particularly vulnerable to high radiation doses during brachytherapy. Excessive dose can lead to acute and late urinary toxicities, including increased frequency, urgency, dysuria, urinary retention, or, in some cases, urethral stricture formation.[54–56] The rectum lies imme-

diately posterior to the prostate and is also at risk of receiving unintended radiation exposure where radiation-induced irritation of the rectal wall may result in symptoms such as rectal urgency, bleeding, diarrhea, or radiation proctitis.[57,58]

2.3.2.2.2 OARs for Gynecological Cancer

In EBRT for gynecological cancers, careful attention is given to surrounding OARs due to their close proximity to the uterus and cervix. These OARs include the bladder, bowel, rectum and, sigmoid. Unintended radiation exposure can lead to cystitis, proctitis, or enteritis, with symptoms ranging from urinary and rectal irritation to abdominal discomfort and long-term bowel dysfunction.[59–63] Depending on the extent of the treatment, additional structures such as the kidneys, femurs, and spinal cord may also be considered OARs, particularly in extended-field treatments or cases involving nodal irradiation.[64,65]

2.3.3 Dose-Volume Metrics and Histograms

Dose-volume metrics are fundamental to both the development and evaluation of radiotherapy treatment plans. These quantitative metrics describe the relationship between the radiation dose and the volume of a given target volume or OAR that receives that dose. They serve as the basis for defining treatment objectives, assessing plan quality, and ensuring consistency with clinical goals.

Two common forms of dose-volume metrics are Dx and Vx. The Dx metric represents the minimum dose received by x% or x cm^3 of a structure. The Vx metric represents the percentage or absolute volume receiving at least x Gy or x% of the prescribed dose. Both Dx and Vx can be expressed in relative (percentage) or absolute (volume in cm^3) terms, depending on the clinical context and institutional protocols.

To visualize these metrics, cumulative dose-volume histograms (DVHs) are utilized. These DVH provides a graphical representation of the cumulative dose distribution within a structure.[8,66] The x-axis represents the dose in gray (Gy), while the y-axis represents either the absolute or relative volume of the structure. DVHs are critical for quickly assessing whether the dose distribution meets planning goals

and how much dose is received by their volumes. For target volumes, an ideal DVH is characterized by a steep, right-shifted curve, indicating that a high proportion of the volume receives the prescribed dose with good uniformity. In contrast, for OARs, a desirable DVH appears as a shallow, left-shifted curve, indicating that only a small volume receives high doses.[8] These typical DVH patterns are illustrated in Figure 2.18.

Dose-volume metrics and their associated histograms provide the foundational language used to define planning objectives and evaluate whether a plan satisfies the clinical requirements. They are essential for assessing trade-offs between target coverage and OAR sparing and are used in planning workflows.

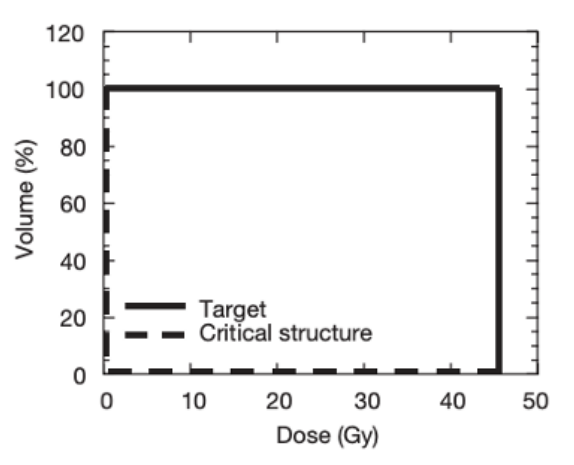

Figure 2.18: Ideal cumulative dose-volume histogram. Example of an ideal cumulative dose-volume histogram where 100% of the target volume receives the full prescribed dose, while the critical structure (organ-at-risk) receives minimal or no dose.[8]

2.3.3.1 Dose-Volume Constraints

Dose-volume constraints serve as quantitative criteria for determining the clinical acceptability of a treatment plan. They establish limits on dose distributions to both target volumes and OARs, aiming to balance effective tumour control with minimized risk of radiation-induced toxicity. These constraints are derived from evidence-based guidelines, institutional protocols and physician experience.

Each constraint defines a threshold using dose-volume metrics such as Dx or Vx,

which specify either a minimum required dose/volume for target structures or a maximum allowable dose/volume for both targets and OARs. Constraints may be expressed in relative terms (as a percentage of structure volume) or absolute terms (in cubic centimeters), depending on the clinical context.

Additionally, constraints can be classified as either hard or soft to help balance tumour coverage with OAR protection. Hard constraints are mandatory constraints that must be met to ensure patient safety, particularly for critical structures like the spinal cord and bowel. Soft constraints are recommended limits that should be met when possible but may be applied more leniently to maintain overall plan quality.[67–71] Together, dose-volume constraints provide a structured basis for evaluating plan quality and ensuring the safe and effective delivery of radiotherapy.

2.3.3.1.1 LDR Prostate Brachytherapy Pre-Implant Dose-Volume Constraints

At BC Cancer Victoria, the evaluation of LDR prostate brachytherapy treatment plans relies on pre-implant dose-volume constraints to assess the anticipated dose distribution based on the planned seed arrangement prior to the implant procedure. Dose constraints are defined for the prostate, which serves as the CTV, as well as the PTV, urethra, and rectum.[53] A summary of these pre-implant dose-volume constraints used for LDR prostate brachytherapy at BC Cancer Victoria is provided in Chapter 3, Table 3.1.

2.3.3.1.2 EBRT for Gynecological Cancers Evaluation Criteria

The dose-volume constraints used at BC Cancer Victoria for evaluating gynecological EBRT treatment plans are guided by the Gynecological Cancer (GEC) guidelines recommended by the European Society for Radiotherapy and Oncology (ESTRO), based on findings from the European MRI-guided Brachytherapy in Cervix Cancer (EMBRACE) studies. Although these guidelines were initially developed for brachytherapy, their principles have been adapted for EBRT.[67–71] Their evidence-based recommendations include hard constraints for target structures to ensure suf-

ficient dose coverage, and maximum dose thresholds for OARs. Additionally, soft constraints are applied to limit OAR volumes receiving specific dose levels, allowing for some flexibility to accommodate individual patient anatomy while maintaining effective tumour control. [64,65] The dose-volume constraints used for gynecological treatment plans are detailed in Chapter 4, Table 4.3.

2.3.4 Treatment Planning Techniques, Systems and Design

Treatment planning techniques in radiotherapy aim to achieve precise dose delivery to the target while minimizing radiation to surrounding normal tissues. This involves both forward and inverse planning approaches, depending on the treatment modality and delivery technique. Forward planning relies on manual beam arrangement and dose shaping, whereas inverse planning uses optimization algorithms to meet specified objectives. Dedicated treatment planning systems (TPS) are used to design and evaluate plans for both LDR brachytherapy and EBRT, where each system has distinct dose calculation methods and optimization tools.

2.3.4.1 Forward Planning

Forward planning is a traditional approach to radiotherapy treatment planning in which the planner manually defines the parameters of the treatment beams to shape the dose distribution. These parameters typically include the number of beams, beam angles, field sizes, weights, and modifiers such as wedges or compensators. The process is iterative, relying on the planner's clinical judgment and experience to achieve a balance between adequate target coverage and sparing of normal tissues. In this approach, the planner manually adjusts beam parameters in an attempt to meet the dose-volume constraints. Each iteration involves manual adjustments followed by recalculation of the dose distribution and review of the DVH to assess whether the plan satisfies clinical constraints.[72,73] As a result, forward planning is generally more time consuming and less flexible in handling complex geometries or multiple competing constraints. It is most commonly used in simpler techniques such as 3D-CRT where less beam shaping and dose variation are needed.[73] Despite its limitations in complex cases, forward planning remains valuable in certain clinical scenarios, particularly

when simplicity, reproducibility, or specific dose distributions are prioritized. It requires a clear understanding of anatomy, radiation physics, and clinical trade-offs to apply dose-volume constraints effectively.[73–75]

2.3.4.1.1 Variseed™ TPS for LDR Brachytherapy

The Variseed™ TPS, developed by Varian Medical Systems, is used at BC Cancer Victoria for the planning and optimization of LDR prostate brachytherapy. The delineated TRUS images are imported into the TPS, where a two-dimensional template grid is applied across the axial image slices to facilitate strategic seed placement within the prostate. This virtual grid replicates the geometry of the physical template used during the procedure, allowing planners to align seed positions with the patient's anatomy in a way that reflects the intraoperative needle insertion setup.

Variseed™ employs a forward planning approach, where the planner manually determines the number, location, and distribution of radioactive seeds before dose calculation based on a set of provincial rules.[53] This process is interactive and iterative, relying on the planner's clinical judgment and understanding of the patient's anatomy. Initial seed placement is based on the prostate's geometry and proximity to critical structures, with the goal of achieving uniform dose coverage while minimizing radiation to OARs.

As each seed is added, removed, or adjusted, Variseed™ recalculates the dose distribution in real time. The system provides immediate visual feedback through isodose lines, color wash overlays, and dose-volume metrics, allowing for the planner to assess the dosimetric impact of each adjustment. This process allows for precise shaping of the dose distribution and allows planners to proactively address areas that may have too much dose or inadequate dose.[76]

2.3.4.2 Inverse Planning

Inverse planning is a modern, algorithm-driven approach to treatment planning, in which the algorithm automatically adjusts some beam parameters to achieve the desired dose distributions. Unlike forward planning, where beam parameters are man-

ually selected, inverse planning allows the planner to define desired dose outcomes, known as optimization objectives, for both target volumes and OARs. The TPS then automatically calculates the optimal beam intensities, parameters and configurations to best satisfy these objectives. While optimization objectives guide the dose distribution during plan generation, dose-volume constraints are still used during the evaluation phase to assess whether the final plan meets clinical requirements. Inverse planning is commonly used with techniques like IMRT and VMAT, which involve extensive dose modulation.[72,73] Given the numerous degrees of freedom in these delivery methods, manual adjustment would be impractical. By leveraging the power of automated optimization, this approach allows for more efficient and accurate optimization of the dose distribution that would be difficult to achieve through manual techniques alone.[75,77] However, the success of inverse planning still depends heavily on the planner's ability to define appropriate objectives and interpret DVHs to ensure that the plan aligns with clinical goals.[75]

2.3.4.2.1 Eclipse™ TPS for EBRT

The Eclipse™ TPS also developed by Varian Medical Systems, is a widely used for EBRT planning and is used at BC Cancer Victoria. It utilizes delineated CT images to create patient-specific treatment plans and supports a wide range of treatments and techniques such as conformal radiation therapy, IMRT, VMAT, proton therapy, and electron beam therapy. For the treatment of gynecological cancers in EBRT, VMAT was used for its ability to precisely sculpt dose around the irregularly shaped target volumes commonly associated with gynecological tumours. Within the Eclipse™ treatment planning system, VMAT planning uses an inverse planning approach, in dose objectives are first defined for each target and OAR structures. Eclipse™ then employs advanced optimization algorithms that iteratively adjust parameters such as gantry speed, dose rate, and MLC positions over one or more continuous arc rotations to achieve the desired dose distribution and objectives.

2.3.4.2.1.1 Photon Optimization

The Eclipse™ features a series of optimization algorithms developed through successive advancements in planning techniques and ongoing updates to its TPS versions to support clinical needs. These include the Dose-Volume Optimizer (DVO), the Progressive Resolution Optimizer (PRO), and the Photon Optimizer (PO).[78–80] Each algorithm builds upon the limitations of the previous one, reflecting advancements in both optimization strategies and radiation beam delivery techniques. DVO was first introduced for IMRT, followed by PRO for VMAT. The PO algorithm is the most recent and currently implemented algorithm for both IMRT and VMAT planning.[81] This section provides a detailed overview of the PO algorithm used in Eclipse™ version 18.0. The PO algorithm streamlines the treatment planning process through a series of steps that begins with the application of a 3D voxel-based grid over the patient's CT imaging dataset. This grid is used consistently for structure delineation, optimization, and dose calculation, promoting spatial accuracy and consistent DVH evaluation (Figure 2.19). The in-plane voxel resolution (x and y directions) is determined by the user-defined resolution, typically 1.25 mm or 2.5 mm. This resolution defines the size of each voxel on a single axial slice and is selected based on the desired balance between anatomical detail and computational efficiency. Finer resolutions (1.25 mm) allow for more precise structure delineation, especially for small or irregularly shaped targets, while coarser resolutions (2.5 mm) reduce computational time at the cost of spatial detail. The z-axis resolution is refined by dividing the image slice spacing by a factor of 1, 2, or 4 to approximate the desired voxel thickness that improves spatial consistency with the x-y resolution.[78]

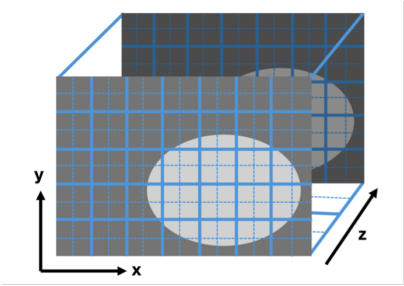

Figure 2.19: Three-dimensional voxel grid for Eclipse™ treatment planning. The grid shows x–y and z resolution used in radiotherapy for structure delineation, optimization, and dose calculations.

With the voxel-based grid established, optimization objectives for both targets and OARs are defined within the optimizer. These objectives are translated into a mathematical cost function, which quantifies how closely the dose distribution aligns with the optimization objectives. the PO applies a weighted quadratic penalty to the structure, calculated as:

$$\text{cost}(D) = \frac{1}{2}\, w \times (D - D_{\text{target}})^2 \tag{2.13}$$

where D is the delivered dose, D_{target} is the intended dose defined by the objective, and w is a weight derived from the priority assigned to that objective. The weight is typically scaled in proportion to the fifth power of the priority value ($w \propto p^5$) ensuring higher-priority objectives have greater influence during optimization. To prevent larger structures from dominating the cost function, weights are further normalized by structure volume. Additionally, a tolerance margin is defined around the objective, with increased penalties applied to voxels falling outside the acceptable dose range.[78]

During the optimization process, the PO algorithm generates initial fluence maps, which represent the intensity of radiation across each beam or control point. These fluence maps are used to calculate the dose distribution across the voxel grid using a Fourier transform-based dose calculation algorithm.[78] The resulting dose distribution is evaluated against the defined optimization objectives using the cost function, which applies weighted quadratic penalties to voxels that deviate from their ideal dose values. The total cost, derived from the cumulative penalties across all objectives, guides the optimizer to iteratively adjust the fluence patterns.

Rather than directly modifying machine parameters such as gantry speed or dose rate, the optimizer instead adjusts the monitor units per degree (MU/deg). This indirect control ensures compliance with the machine's operational constraints such as the minimum and maximum gantry speeds and maximum dose rate. As the optimization proceeds through multiple resolution levels, the PO algorithm incrementally incorporates more stringent machine limitations to ensure the resulting plan is not only dosimetrically optimal but also physically deliverable by the linear accelerator.[78] Through this iterative process of dose evaluation, parameter adjustment, and constraint enforcement, the optimizer gradually converges on a solution that minimizes the total cost while satisfying both the clinical objectives and the operational limits of the treatment machine.

2.3.4.2.1.1.1 Optimization Objectives

Optimization objectives are formulated using dose-volume metrics and are categorized as mean, upper, or lower objectives.[78,79] Mean objectives control the average dose delivered to a structure and are particularly relevant for parallel organs where toxicity is related to the volume of functional subunits exposed to radiation. In contrast, upper objectives are designed to limit the dose received by a volume and are especially important for serial organs where even small regions receiving excessive dose can lead to significant functional impairment.[82] Upper objectives can also be applied to target structures to avoid overdosage and ensure dose uniformity. Lower objectives are typically used for targets to ensure a minimum dose is delivered to a specified volume, thereby maintaining adequate coverage. Within the optimization process, penalties are applied to voxels that deviate from these objectives. Structures that receive insufficient dose are penalized under lower objectives, while those receiving excessive dose are penalized under upper objectives. Each objective is assigned a priority value, which indicates its relative importance and guides the optimization algorithm in balancing competing clinical goals.[78,79] The specific optimization objectives used at BC Cancer Victoria are outlined in Chapter 4, Table 4.1.

2.3.4.2.1.2 Dose Gradients

While optimization objectives are essential for achieving adequate target coverage and sparing OARs, they may not be sufficient on their own to ensure optimal dose distributions. One important consideration is the dose gradient, which describes how quickly the radiation dose decreases outside the target volume. Controlling the dose gradient helps reduce radiation to nearby healthy tissues and OARs while still delivering the prescribed dose to the target.

A steep dose gradient provides better sparing of adjacent normal tissues by confining the high-dose region to the tumour, which is especially important when targets are located near critical structures.[83,84] However, overly steep dose gradients can result in inhomogeneous dose distributions or elevated dose regions (hotspots) near the periphery of the PTV. This is clinically undesirable because the PTV often includes a margin of healthy tissue surrounding the GTV to account for setup uncertainties and organ

motion. When hotspots form in these peripheral regions, they can expose healthy tissue to unnecessarily high doses, increasing the risk of radiation-induced toxicities such as necrosis.[84] In clinical practice, it is preferable to confine these hotspots within the GTV, where higher doses are more tolerable and potentially more effective for tumour control. On the other hand, a shallow gradient promotes better dose uniformity within the target but may increase exposure to surrounding healthy tissue and organs at risk (OARs).[84,85] Balancing these trade-offs is key to achieving clinically acceptable plans, as illustrated in Figure 2.20.

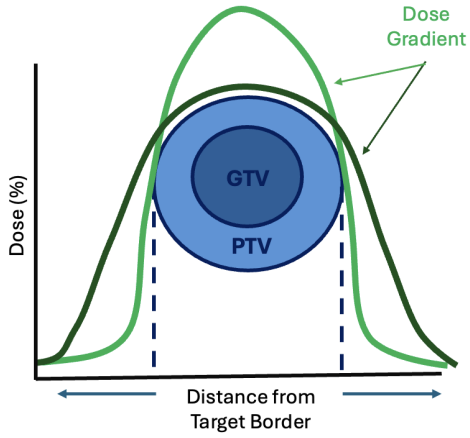

Figure 2.20: Comparison of steep and shallow dose gradients around the target, composed of the gross tumour volume (GTV) and planning target volume (PTV). Steeper gradients confine the high-dose region more tightly to the target, enhancing normal tissue sparing, while shallower gradients promote better dose uniformity within the target but result in greater exposure to surrounding tissues.

In inverse planning, dose gradients can be defined alongside the optimization objectives through built-in tools within the TPS or by manually defining dose structures. These methods allow planners to optimize these dose gradients to fine-tune the trade-off between tumour control and OAR protection. Two commonly used techniques include the use of Normal Tissue Objectives (NTO) and concentric rings, each offering different advantages for shaping the dose distribution in challenging anatomical regions.

2.3.4.2.1.2.1 Normal Tissue Objective (NTO)

One commonly used tool for optimizing dose gradients is the Normal Tissue Objective (NTO), an optimization tool exclusive to the Eclipse™ TPS. The NTO is designed to penalize doses above a specified threshold function is delivered outside the PTV. This threshold is modeled using an exponential decay function:

$$f(x) = \begin{cases} f_0 e^{-k(x-x_{\text{start}})} + f_\infty \left(1 - e^{-k(x-x_{\text{start}})}\right), & x \geq x_{\text{start}} \\ f_0, & x < x_{\text{start}} \end{cases} \tag{2.14}$$

where the parameters are manually defined by the planner within the TPS, as shown in Figure 2.21. The start distance, x_{start}, specifies the distance from the PTV boundary at which the dose fall-off begins and the penalty function becomes active. The start dose (f_0) represents the maximum allowable dose, expressed as a percentage of the prescription dose, at the start distance from the PTV. The end dose (f_∞) defines minimum dose percentage at greater distances from the PTV, establishing a lower bound for the threshold function. The fall-off rate (k) controls the steepness of the dose gradient, with higher values producing a more rapid reduction in dose outside the target volume. Typical fall-off values range from 0.1 to 0.5 mm^{-1}, values closer to 0.3 mm^{-1} or higher are often used to enforce a steeper dose fall-off. Additionally, the NTO is assigned a priority value, which determines its relative weighting in relation to other optimization objectives during optimization.[78,79] These user-defined parameters establish the threshold function, which specifies the maximum allowable dose at varying distances from the PTV. This function guides the PO in evaluating each voxel outside the PTV, where any voxel receiving a dose that exceeds this threshold is penalized. The penalization is applied continuously at the level of individual voxels, allowing for distance-based control of the dose gradient.

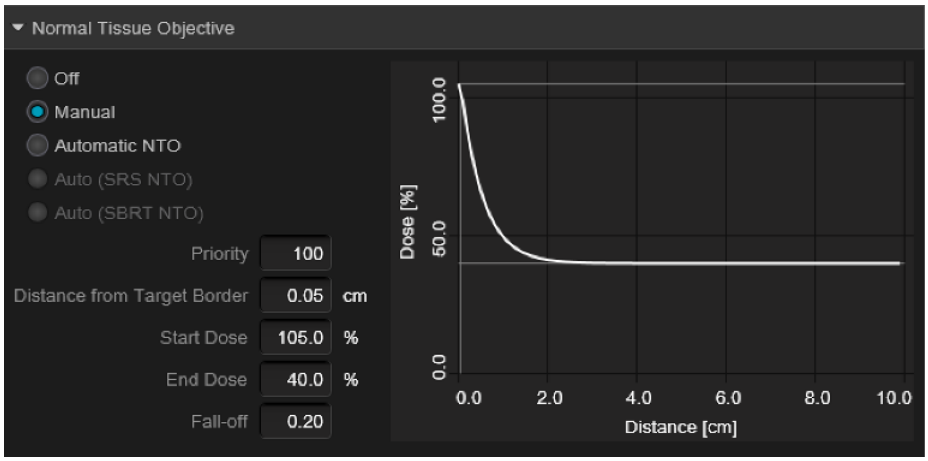

Figure 2.21: Normal tissue objective interface in Eclipse™ treatment planning system. The Eclipse™ treatment planning system provides options to set the Normal Tissue Objective (NTO) to off, automatic, or manual modes. In manual mode, parameters such as start dose, end dose, distance from the target border, and fall-off can be defined by the user to shape the dose gradient in normal tissue.

2.3.4.2.1.2.2 Concentric Ring Structures (CRS)

Concentric ring structures (CRS) are commonly used in treatment planning to control the dose gradient outside the target volume, particularly in systems that do not have built-in tools like the NTO. These structures are manually created by the planner as a series of ring volumes that surround the PTV, each assigned specific dose objectives to guide the optimizer in shaping the dose fall-off. This approach allows for user-defined spatial control of dose distribution using predefined structure volumes. Dose objectives are typically assigned in a descending pattern, where inner rings are permitted higher doses and outer rings are limited to lower doses, creating the dose gradient. This configuration encourages a controlled reduction in dose as the distance from the target increases. The optimization priority assigned to each ring dictates how strongly the constraint is enforced relative to other planning objectives.[86–88]

In creating CRS, several key parameters must be defined by the user, including the number of rings, the thickness of each ring, the spacing between rings, the dose constraints applied to each, and their relative optimization priorities. These parameters collectively influence the shape and steepness of the dose gradient outside the PTV. The number of rings determine the granularity of gradient control, with more

rings allowing for finer modulation but increasing optimization complexity.[86,87] Ring thickness and spacing affect how rapidly the dose falls off with distance where thinner and more closely spaced rings enable sharper gradients, while thicker rings result in broader, smoother transitions.[89] Careful tuning of these parameters allows planners to tailor the dose distribution in anatomically complex regions, making concentric ring structures a flexible and effective tool for dose gradient management.

2.3.5 Dose Calculation Models and Algorithms

Dose calculations are a critical component of radiotherapy treatment planning, as they determine the spatial distribution of radiation dose within the patient. These calculations are performed both during and after optimization and are essential for assessing plan quality and ensuring safe, effective treatment delivery. The specific dose calculation method depends on the treatment modality and planning system. In LDR brachytherapy, Variseed™ employs standardized formalisms to calculate dose based on the spatial arrangement of radioactive seeds. For EBRT systems like Eclipse™ simplified algorithms are applied during optimization for real-time beam adjustments, followed by more advanced models for final dose calculation. The following section describes the dose calculation models and algorithms used in Variseed™ and Eclipse™.

2.3.5.1 Variseed™ Final Dose Calculation: TG-43 Formalism

The TG-43 formalism is standardized dosimetric model used for calculating dose distributions in brachytherapy. Developed by the American Association of Physicists in Medicine (AAPM) Task Group 43 (TG-43) in the mid 1990s, it provides a consistent methodology for calculating the dose distribution around brachytherapy sources.[8,23] This formalism is implemented within the Variseed™ TPS to calculate dose distributions based on the spatial arrangement of radioactive seeds.[89] Widely adopted in clinical practice, this formalism assumes a homogeneous water-equivalent medium and uses source-specific parameters to calculate the dose delivered in tissue.[8,23] To compute the dose distribution around a seed, the TG-43 formalism calculates the dose rate at defined spatial points, characterized by the radial distance (r) and polar

angle (θ) from the center of the seed, as illustrated in Figure 2.22.[8,89,90] The dose rate at a given point is expressed by the following equation:

$$D(r,\theta) = S_k \cdot \Lambda \cdot \frac{G(r,\theta)}{G(r_0,\theta_0)} \cdot g(r) \cdot F(r,\theta) \tag{2.15}$$

where each term accounts for a specific physical or geometric factor influencing the dose distribution.[8,23,89] In this equation, the air-kerma strength, S_k, defines the source strength and is calculated as the air-kerma rate multiplied by the square of the distance from the source. The dose rate constant, Λ, is a source-specific parameter that converts the air-kerma strength into dose rate in water at a reference location, typically 1 cm from the source on the transverse axis.[90] The geometry function, $G(r,\theta)$, accounts for the geometric spread of radiation from the source while neglecting attenuation and scatter. It describes how radiation intensity changes as a function of distance and angle, following the inverse square law. This function is based on either a point-source or line-source approximation and is normalized to a reference value, $G(r_0,\theta_0)$, typically taken at 1 cm and 90°. The radial dose function, $g(r)$, adjusts for the effects of radiation attenuation and scatter in water. It models how the dose decreases with distance beyond what is expected from geometry alone. Lastly, the anisotropy function, $F(r,\theta)$, models the variations in dose depending on direction. It accounts for the effects of source encapsulation and self-shielding, which typically reduce the dose near the ends of the seed along its longitudinal axis.[8,23] Once the dose rate $D(r,\theta)$, Variseed™ calculates the total dose delivered from a single seed by multiplying the dose rate by the isotope's average life (AL) expressed in hours:

$$D(r) = D(r,\theta) \times AL \tag{2.16}$$

The average life in hours is calculated as:

$$AL = \frac{1.0}{\ln(2)} \times 24 \times T_{1/2} \tag{2.17}$$

where $T_{1/2}$ is the half-life of the radionuclide in days. This accounts for the cumulative dose delivered over the entire decay period of the isotope, representing the total energy deposited in tissue from continuous radioactive emission.[89]

To obtain the cumulative dose distribution within the treatment volume and OARs, Variseed™ applies the principle of superposition by summing the dose contri-

butions from all individual seeds across the 3D calculation grid. This dose distribution forms the basis for forward planning by enabling both qualitative and quantitative evaluation of dose coverage to target volumes and OARs.[89]

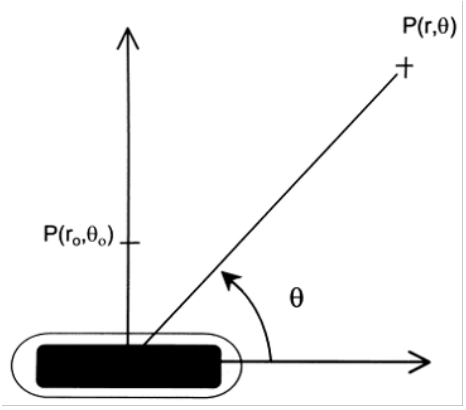

Figure 2.22: Polar coordinate system for brachytherapy. It is used to describe the spatial relationship between a point of interest and a brachytherapy source, defined by radial distance (r) and angle (θ) for dose distribution calculations.[88]

2.3.5.2 Eclipse™ Optimization Dose Calculation Algorithms

During the optimization phase in Eclipse™, the TPS uses fast, approximate dose calculations to guide the optimizer. These approximate dose calculations are performed using the either the Multi-Resolution Dose Calculation (MRDC) or Fourier Transform Dose Calculation (FTDC) algorithm, which are optimized for speed. For VMAT and IMRT optimizations in Eclipse™ version 18.0 using the Photon Optimizer (PO), the Fourier Transform Dose Calculation (FTDC) algorithm is employed.[78,79]

To estimate dose during optimization, FTDC performs a convolution between the attenuated fluence and a scatter kernel, which represents how dose spreads from a single photon interaction in water. This scatter kernel is built from pre-calculated point spread functions (PSFs) derived from Monte Carlo simulations. Rather than performing convolution directly in the spatial domain, where points are convolved and added one by one across the grid, the FTDC uses the Fast Fourier Transform (FFT) to speed up the process. The FFT transforms both the fluence and the scatter kernel into the frequency domain, where convolution is simplified to a faster multiplication process. In this domain, low frequencies represent gradual, smooth variations in dose

intensity across space, while high frequencies represent rapid, sharp changes. After multiplication, an inverse FFT converts the data back to the spatial domain to provide the estimated primary dose.

In addition to the FTDC, planners typically perform an intermediate dose calculation during optimization. This step incorporates more realistic modeling of the dose distribution by accounting not only for the primary dose (D_P), but also for secondary scatter photons (D_S) from the treatment head and electron contamination (D_E) from stray electrons along the beam path. The secondary photon dose is estimated using a simplified model based on the primary fluence and predefined beam parameters, while the electron contamination dose is derived from a predefined curve representing the energy deposited by stray electrons along the beam path. These three components are summed to generate the intermediate dose distribution:

$$D = D_P + D_S + D_E \tag{2.18}$$

This intermediate calculation is typically based on a simplified version of the Anisotropic Analytical Algorithm (AAA), and provides a more accurate representation of the dose distribution than FTDC, without requiring the time of a full final dose calculation. Once optimization is complete, a final, high-resolution dose calculation is performed using AAA or Acuros XB for clinical evaluation and plan approval.[78,79]

2.3.5.3 Eclipse™ Final Dose Calculation: Anisotropic Analytical Algorithm (AAA)

Final dose calculations are performed to ensure accurate and clinically acceptable dose distributions by using advanced algorithms that account for tissue heterogeneity, scatter, and detailed beam modeling. In Eclipse™, two commonly used algorithms are the Anisotropic Analytical Algorithm (AAA) and Acuros XB, both of which model dose contributions from primary photons, scattered photons, and scattered electrons. While both are used for final dose calculation, they differ in how they model radiation transport and their ability to handle heterogeneities within the patient.

AAA is more commonly used in clinical practice due to its balance between computational efficiency and sufficient accuracy in most anatomical regions. However,

Acuros XB is available as an alternative when higher dose accuracy is needed, particularly in highly heterogeneous regions such as cases regarding the thoracic cavities where variations in tissue density significantly affect dose distribution. Acuros XB achieves this by directly solving the Linear Boltzmann Transport Equation (LBTE), providing a more rigorous and detailed modeling of radiation transport through these heterogeneities.[91–93] Although it is more computationally intensive, it is particularly beneficial in scenarios where conventional algorithms like AAA may oversimplify dose deposition. This section focuses on AAA, as it was used to calculate the final dose distributions for all EBRT gynecological treatment plans presented in this thesis.

The AAA models the incident photon fluence as a collection of narrow, individual pencil beams, each delivering dose along its own path. For each pencil beam, the dose is calculated by convolving the beam fluence with a dose-spread kernel, which describes how energy is deposited in surrounding tissue. These kernels are pre-generated using Monte Carlo simulations. AAA calculates the dose as the sum of three components: the primary photon dose, the scattered photon dose, and the electron contamination dose. The primary photon dose is modeled based on photon interactions at the target. The scattered photon dose, also referred to as the secondary photon source, is modeled from photons scattered within parts of the treatment head, such as the flattening filter and collimators. The electron contamination dose accounts for electrons scattered from hardware components like the MLC and jaws. As each pencil beam passes through the patient, AAA accounts for tissue heterogeneity by scaling the dose-spread kernels according to local electron density and radiological depth. This ensures accurate modeling of dose attenuation and scatter in heterogeneous tissues, such as bone or lung. The contributions from all pencil beams and all dose components are then superimposed across the 3D calculation grid to generate the final dose distribution used in clinical treatment evaluation.[78]

2.4 Post-Implant LDR Prostate Brachytherapy Evaluation

Following the implantation procedure, CT images are acquired for post-implant evaluation. These images are delineated by the RO and assessed in Variseed^{TM} to assess

the resulting dose distribution delivered. This step is critical, as it often reveals discrepancies between the planned and actual seed placements and dose distributions. These differences arise from a variety of factors, including anatomical changes, seed migration, or technical variations and uncertainties during the implant procedure.[94–99]

At BC Cancer Victoria, the post-implant constraints are detailed in Chapter 3, Table 3.2. These constraints are more permissive compared to the pre-implant constraints to account for the inherent uncertainties and variations that may occur during implantation procedure. Although these post-implant constraints are generally met, the resulting dose distribution often deviates from the planned distribution.

2.4.1 BrachyVIC-3D

To address the discrepancies between planned and actual seed positions in LDR brachytherapy, BrachyVIC-3D, an in-house developed Python-based dose calculation engine, was developed. This software provides a virtual environment to simulate and analyze procedural uncertainties during seed implantation, predicting their impact on prostate dosimetry. Its core function is to evaluate how variations in seed placement affect dose distribution and to calculate the probabilities of achieving specific pre-implant dose-volume objectives. These outputs offer critical insights into the potential success of the treatment plan, enhancing decision-making in clinical settings.

BrachyVIC-3D initiates its workflow by importing a treatment plan developed in Variseed^{TM}, utilizing the planned seed arrangements as the foundation for simulation. In LDR brachytherapy, seeds are typically stranded together within each needle, causing them to shift in a similar manner during implantation. To reflect this, the software simulates procedural uncertainties by applying random radial and longitudinal shifts to each seed strand relative to the needle's path. These shifts represent potential needle deflections that can occur due to intraoperative factors such as patient movement or variations in tissue density that deviate from the intended placement. As a result, the simulation produces coordinated seed displacement that realistically mimics the variability observed during actual clinical procedures. Following these shifts, the dose distribution is recalculated based on the new seed positions using the AAPM TG-43 formalism. This recalculation produces updated dose-volume metrics for the pre-implant dosimetry objectives, reflecting the impact of positional variations on the

resulting dose distribution.

To obtain a representative estimate of the dose distribution under procedural variability, BrachyVIC-3D performs 100 simulation iterations. For each structure's dose-volume constraints, the mean dose-volume metric and corresponding standard deviation are calculated based on the values obtained from all iterations. These values are then used to determine the probability of achieving each pre-implant dosimetry objective, using the probability density function of the normal distribution, defined as:

$$f(x \mid \mu, \sigma^2) = \frac{1}{\sqrt{2\pi\sigma^2}} e^{-\frac{1}{2}\left(\frac{x-\mu}{\sigma}\right)^2} \tag{2.19}$$

where x is the specific pre-implant dosimetry constraint, μ is the mean dose-volume metric, and σ is the standard deviation calculated from the 100 iterations. As illustrated in Figure 2.23, the software interface displays the initial dose-volume metrics imported directly from the Variseed$^{\text{TM}}$ plan, providing a baseline for comparison. Following the simulation, the interface presents the mean and standard deviation for each pre-implant dosimetry objective, along with the corresponding probability of achieving that objective.

In this thesis, the work presented in Chapter 3 investigates the functionality and application of BrachyVIC-3D as a probabilistic tool for assessing the robustness of treatment plans against uncertainties in seed placement during LDR prostate brachytherapy. By incorporating BrachyVIC-3D into the treatment planning workflow, clinicians can gain greater confidence in the feasibility and effectiveness of achieving the proposed dosimetric constraints.

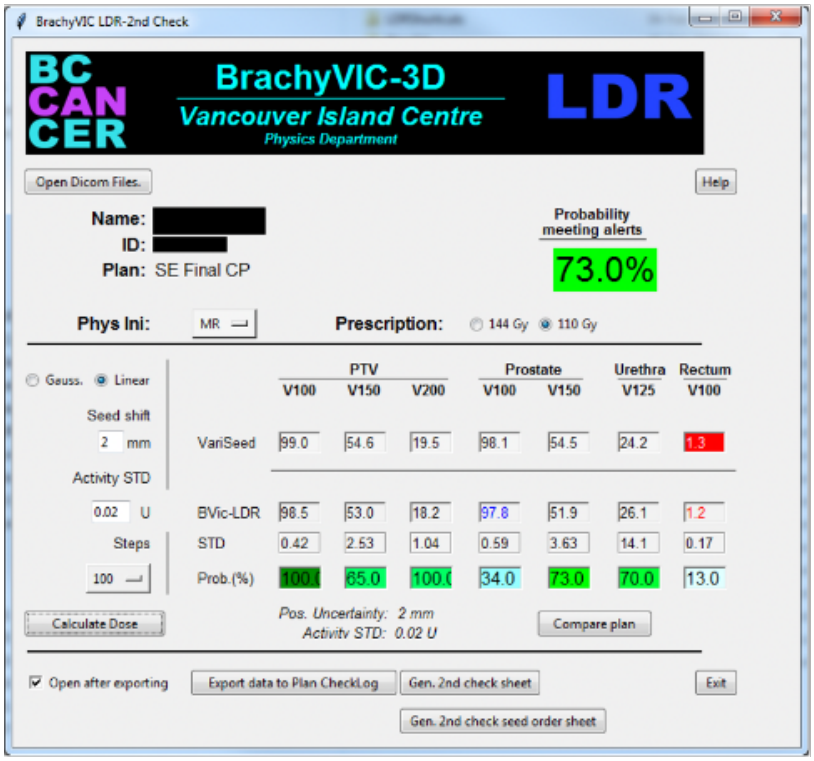

Figure 2.23: BrachyVIC-3D software interface. The interface displays the initial dosimetric parameters imported from the Variseed^{TM} plan, along with the mean dose-volume metrics and corresponding standard deviations calculated from 100 simulated iterations. These values are used to estimate the probability of meeting clinical constraints under seed placement uncertainty.

2.5 Application of Machine Learning Techniques in Clinical Decision Making

Machine learning (ML) involves the development of algorithms capable of learning from and making predictions or decisions based on data. This technology has been increasingly utilized in medical physics to enhance various aspects of patient care. ML algorithms and techniques have been used to analyze vast datasets of treatment plans, identifying patterns that optimize therapy parameters for personalized care. These algorithms enhance the precision of treatment by predicting tumour responses and tailoring radiation doses to maximize tumour control while minimizing exposure to healthy tissues.

Furthermore, ML contributes to the automation of radiation therapy planning tasks such as structure delineation, significantly reducing clinician workloads and enhancing the efficiency of treatment planning.[100,101] By extracting insights from previous treatment data, ML not only improves the accuracy and effectiveness of radiation therapy but also have been shown to streamline clinical workflows.[102,103] This leads to more efficient clinical operations and better patient outcomes, as treatments are more accurately targeted and adapted to individual needs. Overall, the integration of ML into radiotherapy represents a transformative advancement in cancer care, promoting more effective and adaptive treatment strategies.

2.5.1 Defining the Problem

Defining the problem is a foundational step in any ML project. It establishes the nature of the learning task and guides the selection of appropriate models, data processing techniques, and evaluation strategies. Machine learning problems are generally categorized based on how the model learns from the data. The three main types of learning are supervised learning, unsupervised learning, and reinforcement learning. These types differ primarily in the kind of data provided to the algorithm and the nature of the feedback during training.[104]

In supervised learning, the model is trained using a dataset composed of input and output pairs. Each input, also known as features, is linked to a known label or outcome, referred to as targets. The goal is to learn a function that can accurately predict the label for new, unseen features. In unsupervised learning, the data are not labeled, and the objective is to discover hidden patterns or groupings within the data, such as clusters or underlying structures. Reinforcement learning takes a different approach, where an agent learns to make decisions by interacting with an environment and receiving feedback in the form of rewards or penalties.[103,104]

This work focuses specifically on supervised learning, and more precisely, on the task of classification. Within supervised learning, tasks can be divided into regression, where the target variable is continuous, and classification, where the goal is to assign inputs to discrete categories or labels. For example, regression might be used to predict a patient's age based on medical data, whereas classification would be used to determine whether the patient has a particular disease.

In classification tasks, the model learns to assign each input to one of several possible classes. This can involve binary classification, where there are two classes, or multiclass classification, where more than two categories are involved. Evaluating the performance of a classification model typically involves metrics based on true positives, true negatives, false positives, and false negatives, depending on the context and importance of different types of misclassifications.[105]

2.5.2 Data Preprocessing

Data preparation and preprocessing are crucial steps in the machine learning workflow, as the quality and structure of the data directly impact ML performance. An important early consideration in this process is the selection of input features. These features should not only demonstrate statistical significance but also possess clinical relevance especially in healthcare applications, where model interpretability and practical utility are essential. Once relevant features and targets are identified based on the problem definition, the data undergoes preprocessing, which involves cleaning the data by handling missing values, removing duplicates, and correcting inconsistencies. Features may be normalized or standardized to ensure comparability across different scales, and categorical variables are encoded into numerical formats. Additionally, the dataset is split into training, validation, and test subsets to enable proper model development and evaluation. Thoughtful and effective data preparation ensures that the learning algorithm receives accurate, meaningful, and representative input, enabling the development of robust and clinically useful ML applications.[104,105]

2.5.2.1 Data Splitting

To develop machine learning models that generalize well to unseen data, the dataset is typically divided into separate subsets which include training, validation, and test sets. Ensuring that these splits are representative of the overall dataset helps prevent biases and gives a true measure of the model's predictive power. Each subset serves a distinct role in the model development process.

The training set, which usually comprises about 70% to 80% of the dataset, is the primary component used to develop the machine learning model.[106] This proportion

provides the algorithm with input-output pairs from which it learns patterns and relationships. The model repeatedly fine-tunes its internal parameters to reduce prediction errors based on this data. The quality and representativeness of the training data are crucial because the model's performance is significantly influenced by what it learns during this phase.

The validation set, typically making up 10 to 20% of the dataset, acts as an independent dataset not encountered during training.[106] It provides feedback on how well the model generalizes and is crucial during model development for fine-tuning hyperparameters and monitoring for overfitting. Hyperparameters are specific settings that vary between models and control aspects of the training process, such as the learning rate or the model's complexity. Proper tuning of these settings allows for the improvement of the model's ability to generalize beyond the training data. Overfitting occurs when a model learns the noise in the training data rather than just the underlying patterns, leading to poor performance on new, unseen data.[105] Using the validation set to evaluate the model's performance, this allows for the refinement of the current model, ensuring it performs well on both seen and unseen data.

The test set, which is composed of about 10% to 20% of the dataset, is reserved until the very end of the ML model development process.[106] It provides an unbiased evaluation of the final model's performance. While the validation set may indirectly influence model design through its use in tuning and selecting models, the test set acts as a definitive measure to assess how well the trained model is expected to perform in practical applications. Performance results based on the test set are typically reported as indicators of the model's generalization ability.

2.5.3 Classification Model Evaluation Metrics

Performance evaluation of classification models in clinical settings is essential for ensuring their reliability and effectiveness. Common metrics such as accuracy, precision, recall (sensitivity), specificity, false positive rate, and F1-score are used to assess how well a model distinguishes between positive and negative cases.[104,106] These metrics are derived from four basic classification outcomes: true positives (TP), true negatives (TN), false positives (FP), and false negatives (FN).[107] TP and TN represent correctly identified cases, while FP and FN indicate misclassifications with poten-

tially important clinical consequences. Derived from these four outcomes, the metrics are discussed in greater detail in Chapter 3, where they are applied to assess model performance across LDR prostate brachytherapy treatment planning.

2.5.4 Threshold-Based Decision-Making in Binary Classifi- cation

In clinical research and practice, decision-making is increasingly supported by statistical and machine learning (ML) techniques, which provide frameworks for evaluating the potential benefits and risks of different treatment strategies and interventions. These methods are essential across a wide range of applications, including early disease detection, diagnosis, treatment response evaluation, and prognosis estimation. By applying advanced analytical approaches grounded in statistical theory, clinicians and researchers can extract meaningful insights from complex datasets, account for variability in patient responses, and make predictions with greater confidence.[108] Machine learning can be understood as an extension of classical statistical methods, using computational tools to scale, automate, and refine data-driven decision-making.

Although this thesis does not employ machine learning algorithms in the traditional sense, it adopts a statistical decision-making framework to solve a binary classification problem. Specifically, a clinical predictor variable was analyzed using Receiver Operating Characteristic (ROC) curve analysis, and the optimal decision threshold was determined using the Youden Index. Classification performance was evaluated using standard metrics such as accuracy, precision, recall, and F1-score. This approach supports the development of interpretable, clinically actionable thresholds using robust statistical principles that are closely aligned with the foundations of machine learning.

Threshold-based classification is a fundamental approach in clinical decision-making, particularly in binary scenarios such as determining the presence or absence of disease or assessing treatment success versus failure.[109,110] This method applies a threshold to a model's predicted probabilities, converting its continuous outputs into discrete classes. For example, if a model predicts the probability of disease being present and its value exceeds a predefined threshold, the outcome is classified as present. If its probability falls below the threshold, it is classified as absent. This approach allows for probabilistic outputs to be used in clinical decisions, which is essential in healthcare

settings where treatment pathways are based on definitive categorizations.[110]

2.5.4.1 Receiver Operating Characteristic Curve Analysis

The Receiver Operating Characteristic (ROC) curve is a fundamental tool for evaluating the performance of binary classification models in both clinical research and machine learning. In clinical settings, ROC curve analysis is particularly valuable when evaluating models for diagnostic tests, screening tools, or treatment response prediction. It provides a graphical representation of a model's ability to distinguish between two classes across a range of decision thresholds. Specifically, the ROC curve plots the TPR also known as recall or sensitivity, against the false positive rate (FPR).[111–116]

Each point on the ROC curve corresponds to a different threshold used to classify predictions as positive or negative. As the threshold is varied, the TPR and FPR change accordingly, generating the curve (Figure 2.24). The lower left corner of the graph (0, 0) represents a model that predicts all outcomes as negative (no sensitivity, no FP), while the upper left corner (0, 1) represents an ideal model with 100% sensitivity and 0% false positives. The diagonal line from (0, 0) to (1, 1) represents random guessing, where any model performing along this line has no discriminative power.[117]

A model with a curve that curves toward the top-left corner of the ROC space demonstrates better classification performance, as it reflects higher sensitivity for a given level of false positives. The area under the curve (AUC) serves as a scalar summary of this performance. An AUC of 1.0 indicates perfect discrimination, meaning the model correctly distinguishes between all positive and negative cases. An AUC of 0.5 suggests no discriminative ability, equivalent to random guessing. An AUC below 0.5 implies that the model performs worse than random guessing.[117,118] Higher AUC values reflect stronger classification performance, making it a key metric for selecting models in both clinical decision-making and machine learning applications.

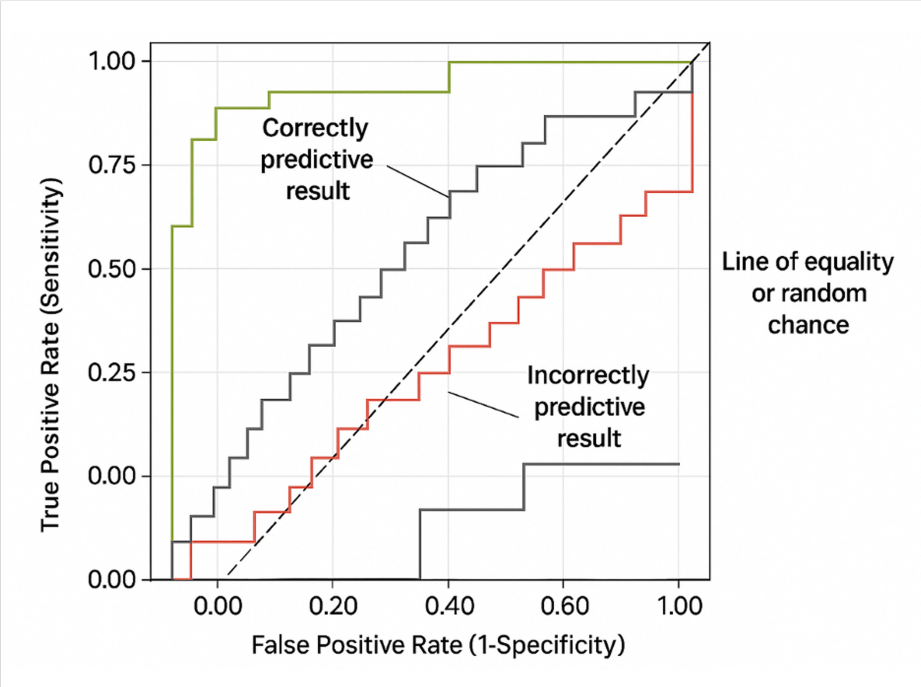

Figure 2.24: Receiver Operating Characteristic (ROC) curves of various sensitivities and specificities. ROC curves represent the trade-off between sensitivity (true positive rate) and 1-specificity (false positive rate) for predictive models. The green curve represents a perfectly predictive model, the grey curve reflects a moderately predictive model, and the red curve indicates poor predictive performance. The black dashed line represents the line of equality or random chance.[114]

2.5.4.2 Youden Index

The Youden Index, also known as Youden's J statistic, is a commonly used metric in the evaluation of diagnostic and predictive models, particularly in clinical settings. It combines sensitivity (true positive rate) and specificity (true negative rate) into a single value, assessing the overall effectiveness of a model.[118,119] By identifying the point on the ROC curve that maximizes the difference between TP and FP rates, the Youden Index helps determine the optimal threshold for distinguishing between two classes. The index is calculated as:

$$J = \text{Sensitivity} + \text{Specificity} - 1 \tag{2.20}$$

with values ranging from 0 to 1. A value of 1 indicates perfect classification with no false positives or false negatives, while a value of 0 suggests that the model performs no better than random guessing.[112]

In the context of ROC curve analysis, the Youden Index identifies the point that maximizes the vertical distance between the ROC curve and the diagonal line representing random performance. This point corresponds to the threshold where the sum of sensitivity and specificity is maximized, offering a balanced trade-off between the two metrics.[112] The Youden Index is particularly useful when sensitivity and specificity are equally important, making it well-suited for clinical scenarios where both false positives and false negatives carry significant consequences. By selecting the threshold that maximizes the Youden Index, clinicians can make more objective and reliable decisions based on statistically optimal classification performance.

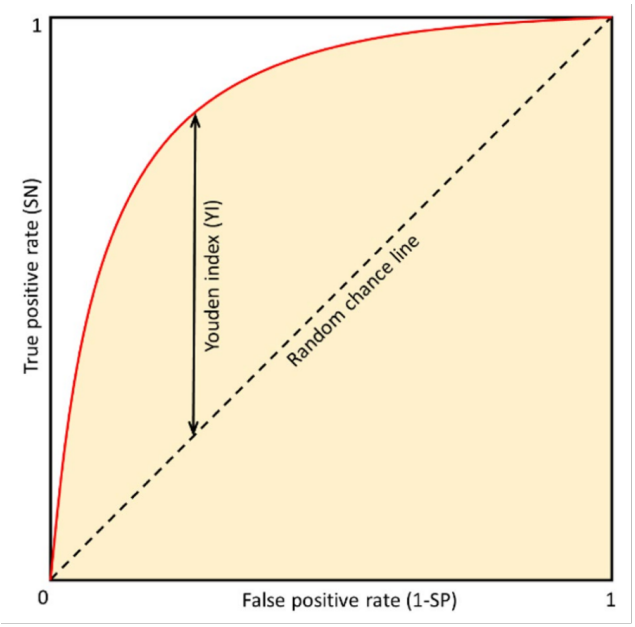

Figure 2.25: Youden index on receiver operating characteristic (ROC) curve. The red curve reflects a high-performing model, while the black dashed line represents the line of equality or random chance. The Youden index identifies the optimal threshold that maximizes the difference between the true positive rate and false positive rate.[117]

Chapter 3

Assessing dosimetric uncertainty in prostate LDR brachytherapy: the impact of seed position variability on treatment outcomes

3.1 Introduction

Prostate cancer is the highest incident non-skin cancer among Canadian men and the third most common cause of cancer-related mortality. In 2023, it was estimated that 25 900 men would be diagnosed with prostate cancer representing 21% of all new cancer cases, whereas 4 900 men would die from prostate cancer representing 10% of all cancer-related deaths in Canada alone.[121]

Currently a variety of viable management strategies are available for prostate cancer, depending on the stage and grade of the prostate cancer.[121] These approaches include active surveillance, surgery, systemic therapies, and radiation therapies. Nonetheless, radiation therapy is one of the most commonly utilized forms of treatment, as it is highly effective and well tolerated with wide eligibility. Radiation therapy may include external beam radiation therapy, and/or brachytherapy. The goal of both is to maximise dose to the tumour while minimising does to healthy tissues and or-

gans at risk (OAR). For prostate cancers, low-dose rate brachytherapy (LDR) may be more favourable due to its high rates of disease control, efficiency, and favourable quality of life profile, with low rates of urinary incontinence, bowel toxicity, and sexual dysfunction.[119,122–125] LDR brachytherapy involves the implantation of permanent radioactive seeds, usually iodine-125 or palladium-103 into the prostate gland, exposing the tumour to radiation over a prolonged period of time.

Ensuring accurate seed placement is essential for successful treatment outcomes. The effectiveness of LDR brachytherapy is typically evaluated by post-implant dosimetry constraints, such as Prostate D90% (the dose covering 90% of the prostate) and V100% (the volume of the prostate receiving 100% of the prescribed dose), which reflect the actual dose distribution after implantation. Pre-implant planning aims to maximize radiation coverage to the tumour while minimizing exposure to organs at risk (OARs). To achieve this, several steps are taken to distribute the seeds in a safe and optimal manner for the patient. The process begins with prostate volume study, conducted using a transrectal ultrasound to create a three-dimensional image of the prostate, which determines its exact size and shape. The volume study also serves to determine patient eligibility, as the pubic arc may obstruct access to the prostate in some cases.[33]

Using the images from the transrectal ultrasound (US), the prostate is contoured for the LDR brachytherapy treatment plan. This step precedes the strategic positioning of radioactive seeds within the planning target volume (PTV) that maximizes radiation dose to the target volume, while protecting the adjacent healthy tissues. Various predefined dose-volume constraints for both the target and organs at risk (OARs) guide the placement of the radioactive seeds within the target, ensuring a uniform distribution of the prescribed dose within the treatment planning system (TPS).[53,126,127] Dose calculations for seed placement adhere to the AAPM Brachytherapy TG-43 formalism, allowing for precise visualization and calculation of the three-dimensional dose distribution, optimizing treatment delivery.[23] Once the treatment plan is developed, it is reviewed by the radiation oncologist (RO) for approval or revision.

During the seed implantation procedure, the patient is anesthetized and positioned in a manner similar to that used during the volume study. The RO uses the treatment plan to guide the insertion of pre-loaded needles manually through a standard needle

template via the perineum, to deposit the radioactive seeds into the prostate.[16,127] The procedure is image-guided, using both real-time trans-rectal ultrasonography and on-demand fluoroscopy. Based on the RO's discretion, additional seeds also referred to as non-planned supplemental seeds (NPSS), may be inserted to compensate for any seed placement discrepancies observed during the procedure. This flexibility permits real-time adjustments to ensure adequate coverage, leading to deviations not only in the number of seeds used compared to the initial treatment plan but also in the planned dosimetry, as the actual dose distribution may differ due to these adjustments.

After implantation, the arrangement of the seeds and the dose distribution are typically evaluated using post-implant computerized tomography (CT) images. These images are used to assess post-implant dosimetry constraints, which are typically more permissive than the pre-implant dosimetry constraints, which are typically more permissive than the pre-implant dosimetry constraints. Although these post-implant constraints are generally met, there are instances when they cannot be achieved due to the difficulties or misplacement during implantation procedure. This can lead to significant discrepancies between the actual placement and the planned placement of the seeds and therefore the post-implant dose distribution.

The accuracy of seed placement is heavily influenced by factors such as the reproducibility of the patient's position and anatomical variations. Replicating the exact position from the volume study in the operating room can be challenging. Furthermore, during anesthesia, relaxation of the pelvic muscles may cause internal shifts in the position of the prostate, rectum, or bladder, differing from their positions during the prostate volume study when the patient is conscious. Additionally, studies have demonstrated that anatomical changes can influence the delivered dose distribution in external beam radiation treatments.[128–132] Given these observations, variations in prostate volume may occur between the initial volume study and the actual implantation procedure, particularly in patients undergoing both external beam radiotherapy and LDR brachytherapy boost. It is also possible for the prostate volume to change during and post- procedure due to prostate edema caused by needle trauma.[133,134] Studies indicate that patients with smaller prostates are more likely to experience significant post-implantation edema.[94,95] Discrepancies in seed positioning can additionally be attributed to the implant procedure itself, which demands considerable manual dexterity and skill from the RO. The skill of an RO is crucial in

the precise placement, retraction and injection of the pre-loaded needles during seed implanation.[96] As such, it is not uncommon for seeds to be deposited a few millimeters away from the intended coordinates. Lastly, uncertainties associated with image guidance systems also contribute to seed position during the implantation procedure. Several studies have examined the uncertainties of trans-rectal ultrasound geometry and their effects on needle placement and dosimetry.[97–99]

Accurate placement of radioactive seeds is crucial for delivering an effective dose to the prostate in LDR brachytherapy. However, various factors such as discrepancies in patient anatomy, positioning variations, and differences between planned and actual seed positions can significantly affect the final dose distribution. These uncertainties undermine the ability to consistently replicate the intended seed position and dose distribution seen in planning. This study seeks to establish a method for quantifying the likelihood of achieving post-implant dosimetry constraints, which are critical for evaluating target coverage. By applying a probability-based approach, this study aims to assess seed position uncertainty and use probability thresholds as predictive tools to enhance the reliability of treatment plans in meeting the post-implant dosimetry constraint, prostate D90%, in prostate LDR brachytherapy.

3.2 Materials and methods

3.2.1 Study population

This study included 172 prostate cancer patients previously treated with LDR brachytherapy at BC Cancer-Victoria, British Columbia, between 2019 to 2022. Patients were treated with prescribed doses of either 110 Gy or 144 Gy, utilizing Iodine-125 (^{125}I) radioactive seeds implanted within the prostate.

Volume studies were performed on all patients, involving the acquisition of transverse US images of the prostate from the base to the apex at 5 mm intervals. Prior to developing the treatment plan, the RO manually contoured the prostate within these images. These contours underwent review by the brachytherapy group as part of the institutional peer-review process.

Treatment plans were manually generated by physicists using Variseed™ (version 9.0) a Varian Medical System's commercial planning software for LDR brachytherapy. These plans were based on the US images obtained from the volume study and employed a modified peripheral loading technique. The planning process followed the protocols established by BC Cancer-Victoria, incorporating specific seed activity characteristics and patterns to customize each plan to the unique patient's anatomy and dosimetric requirements.[53]

For post-implant assessment, the dosimetry was evaluated using CT images acquired immediately after the implant procedure (Day 0). The seed locations on the CT images were determined by the software and adjusted, if necessary, by the physicist. The prostate, rectum, and urethra were then manually contoured by the radiation oncologist who performed the implant. These images were not registered with the initial US images.

3.2.2 Pre-implant and post-implant dosimetry constraints

Pre-implant dosimetry constraints used to generate treatment plans are defined from dose-volume histograms (DVH) of the targets and OARs. These dosimetry constraints are indicated by Vx%, representing the volume (expressed as a percentage or in cubic centimeters) of the target structures or OARs that receive x% of the prescribed dose, and Dx%, which refers to the dose that covers x% of the volume.

Detailed specifications of the pre-implant and post-implant dosimetry constraints are outlined in Table 3.1 and Table 3.2, respectively. Table 3.1 presents the pre-implant dosimetry constraints for the PTV, prostate, and OARs, while Table 3.2 details the post-implant constraints to assess treatment efficacy.

Table 3.1: Summary of pre-implant dosimetry constraints for low dose rate prostate brachytherapy.

Target/OAR	Pre-implant dosimetry constraints
Planning target volume (PTV)	V100% $\geq$ 98%
	V150% = 50 – 60%
	V200% $\leq$ 21%
Prostate (CTV)	V100% $\geq$ 99%
	V150% = 56 – 65%
	V200% $\leq$ 22%
Urethra	V125% $\leq$ 30%
	V150% $\leq$ 5%
	D50% $\leq$ 120%
Rectum	V100% $\leq$ 1cm^3

Table 3.2: Summary of post-implant dosimetry constraints for low dose rate prostate brachytherapy.

Target/OAR	Post-implant dosimetry constraints
Prostate (CTV)	V100% $\geq$ 90%
	V150% = 45 – 65%
	D90% = 100 - 125%
Urethra	D50% $\leq$ 120%
Rectum	D100% $\leq$ 1cm^3

3.2.3 Python-based in-house dose calculation engine

A Python-based in-house dose calculation engine (BrachyVIC-3D) was developed to determine the probability of achieving each pre-implant dosimetry constraint when seed position uncertainties during implantation are simulated. The DICOM plan file generated in Variseed^{TM} was exported to the BrachyVIC-3D software, where the seed positions were randomly shifted 2 mm and 3 mm linearly in the radial and longitudinal direction of the needle to reflect typical procedural variations and the anatomical constraints of the prostate region.

Following the shifts, the software calculates the three-dimensional dose distribution based on the AAPM TG-43 formalism. Under this formalism, both BrachyVIC-3D and Variseed^{TM} employ the point-source approximation when calculating dose, which may introduce some additional uncertainty in the delivered dose. This process is repeated 100 times to achieve statistical standard deviation, with each iteration recalculating the dose distribution. At the end of the 100th iteration, BrachyVIC-3D calculates the mean value and standard deviation of each pre-implant dosimetry constraints as depicted in Figure 3.1.

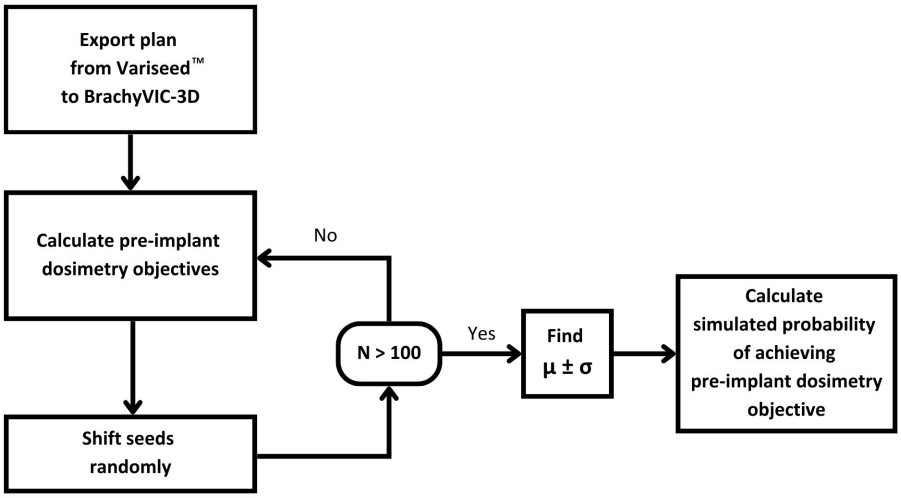

Figure 3.1: Python-based in-house software (BrachyVIC-3D) architecture. Treatment plans are exported from Variseed^{TM} to BrachyVIC-3D software. The software calculates the pre-implant dosimetry constraints followed by shifting the seeds to simulate the variations in seed placement that occurs during implantation. After 100 simulations (N), the mean (μ) and standard deviation (σ) of each pre-implant dosimetry objective is calculated to determine the probability of achieving the pre-implant dosimetry constraints.

The probability of achieving that pre-implant dosimetry constraint was determined through the probability density function of the normal distribution, as shown:

$$f(x \mid \mu, \sigma^2) = \frac{1}{\sqrt{2\pi\sigma^2}} e^{-\frac{1}{2}\left(\frac{x-\mu}{\sigma}\right)^2} \tag{3.1}$$

where x represents the pre-implant dosimetry constraint, μ is the mean dose value, and σ is the standard deviation, both calculated from the 100 iterations for that constraint. This function was used to model the likelihood of achieving the specific

pre-implant dosimetry constraint based on the distribution of dose values. The global probability of achieving all target pre-implant dosimetry constraints was also calculated by assigning equal weights to the individual probabilities of achieving PTV V100%, PTV V150%, prostate V100%, and prostate V150%, respectively.

Simulations beyond 100 iterations provided little additional benefit, as the standard deviation after 100 iterations was already less than 1%. The entire simulation process, including shifting seed positions and recalculating dose, was completed in approximately 25 seconds per treatment plan (in a regular PC) and was performed after the treatment plan was created as part of the pre-implant quality assurance process.

Probabilities of achieving pre-implant dosimetry constraints for both the PTV and prostate, and the global probability for each patient treatment plan, were extracted for the study. The probability distributions for each pre-implant dosimetry constraint and the global probabilities were evaluated to identify any recognizable patterns that could aid in predicting the successful achievement of post-implant dosimetry constraints.

3.2.4 Threshold determination

To identify the optimal probability thresholds that would predict the likelihood of achieving post-implant dosimetry constraints, patient treatment plans were divided into training, validation, and testing sets. Seventy-five percent of treatment plans (129 patients) were allocated for training and validation, while 25% (43 patients) was used for testing. The optimal probability thresholds were first determined using the training and validation sets, followed by an assessment of their reliability using the testing set. To ensure a robust evaluation, the training and validation data were shuffled 20 times, with each iteration randomly splitting the data into 75% for training and 25% for validation, minimizing the bias and variability.

The probability thresholds for selected pre-implant dosimetry constraint probabilities were determined using Receiver Operating Characteristic (ROC) curve analysis.[111–115] The ROC curve was generated by plotting the true positive rate (sensitivity) against the false positive rate (1-specificity) across various threshold values, thereby visualizing the trade-offs between sensitivity and specificity at different probability thresh-

olds. Sensitivity referred to the ability of a threshold to correctly identify cases that successfully achieved post-implant dosimetry constraint, prostate D90% = 100 – 125% (true positives):[113]

$$\text{Sensitivity} = \frac{\text{True Positives}}{\text{True Positives} + \text{False Negatives}} \tag{3.2}$$

Specificity measured the ability of the threshold to correctly identify cases that did not achieve the post-implant constraint (true negatives):[113]

$$\text{Specificity} = \frac{\text{True Negatives}}{\text{True Negatives} + \text{False Positives}} \tag{3.3}$$

This approach enabled the assessment of each pre-implant dosimetry constraint's probability in terms of its ability to predict the likelihood of achieving specific post-implant dosimetry constraint, prostate D90%. The discriminative power of the probability thresholds for each constraint was assessed by generating receiver operating characteristic (ROC) curves and computing the corresponding area under the curve (AUC). ROC curve shapes were evaluated to assess the trade-off between sensitivity and specificity, while the AUC served as a quantitative measure of the threshold's ability to distinguish between plans that met and did not meet the post-implant constraint. AUC values range from 0 to 1, where an AUC of 0.5 indicates no discriminative power, and an AUC closer to 1.0 reflects excellent discriminative ability.[112–115]

In conjunction with the ROC curve, the Youden Index was calculated at each threshold along the curve. The Youden Index was used to determine the point on the curve that maximizes the sum of sensitivity and specificity on the ROC curve. Mathematically, the Youden Index (J) is defined as:[118]

$$J = \text{Sensitivity} + \text{Specificity} - 1 \tag{3.4}$$

where the threshold corresponding to the maximum value of J was selected as the optimal threshold.[112,118,135–137] By analyzing the shape and AUC of the ROC curve, along with calculating the Youden Index, the optimal probability threshold was assessed.

3.2.5 Threshold validation, testing and evaluation metrics

For each iteration, the dataset was shuffled and split into training and validation sets to ensure robust and consistent threshold determination. The ROC curve and Youden Index were applied to the training data to identify the optimal threshold for predicting post-implant dosimetry success. This threshold was then validated on the validation set, where its performance was evaluated using metrics such as accuracy, precision, recall, and F1-score.

Accuracy was defined as the proportion of treatment plans where the threshold correctly simulated whether or not the plan would achieve the post-implant dosimetry constraint, prostate D90%, relative to the total number of plans. It was calculated as:[138]

$$\text{Accuracy} = \frac{\text{True Positives} + \text{True Negatives}}{\text{True Positives} + \text{True Negatives} + \text{False Positives} + \text{False Negatives}} \tag{3.5}$$

Precision measured the proportion of treatment plans that were simulated to meet the threshold and were correctly classified as having achieved prostate D90%, defined as:[138]

$$\text{Precision} = \frac{\text{True Positives}}{\text{True Positives} + \text{False Positives}} \tag{3.6}$$

Recall (or sensitivity) assessed how well the threshold correctly identified treatment plans that successfully achieved prostate D90%:[138]

$$\text{Recall} = \frac{\text{True Positives}}{\text{True Positives} + \text{False Negatives}} \tag{3.7}$$

The F1-score balanced precision and recall provide a single measure of how well the threshold predicts the achievement of post-implant constraint, prostate D90%. This metric is crucial when the threshold may predict many plans as successful (high recall), but some of those plans do not actually achieve prostate D90% (lowering precision):[138]

$$F_1 = 2 \times \frac{\text{Precision} \times \text{Recall}}{\text{Precision} + \text{Recall}} \tag{3.8}$$

This process was repeated for 20 iterations to minimize bias, with the dataset being reshuffled and re-split in each cycle. The mean threshold from these 20 iterations was selected as the final threshold for each pre-implant dosimetry constraint probability to ensure generalizability. The mean thresholds were then applied to the test set. Testing ensured that the thresholds were reliable and effective on unseen patient data, providing confidence in their ability to guide treatment planning decisions.

3.3 Results

Table 3.3: Summary of pre-implant target dosimetry constraints achievements.

Pre-implant dosimetry constraints	Criteria	Number of patients met	Percentage met	Number of patients not met	Percentage not met
Prostate V100%	$\geq$ 99%	124	96.12%	5	3.88%
Prostate V150%	56 - 65%	104	80.62%	25	19.38%
PTV V100%	$\geq$ 98%	127	98.45%	2	1.55%
PTV V150%	50 - 60%	99	76.74%	30	23.26%
PTV V200%	$\leq$ 21%	122	94.57%	7	5.43%

Table 3.3 presents the number of patients who met or did not meet the target pre-implant dosimetry constraints. More than 95% of patients achieved the minimum required coverage for prostate and PTV V100%, demonstrating strong adherence to these target constraints. In contrast, the success rate dropped to approximately 75 - 80% for prostate and PTV V150%, indicating that these metrics are more susceptible to variations in seed placement and the associated uncertainties. For PTV V200%, 94.57% (122 patients) met the constraint, while 5.43% (7 patients) did not. Majority of the patients have shown to have met the dosimetry constraints, though prostate V150% and PTV V150% showed higher proportion of patients not meeting the target coverage compared to the other metrics.

Table 3.4: Summary of post-implant target dosimetry constraints achievements.

Post-implant dosimetry constraints	Criteria	Number of patients met	Percentage met	Number of patients not met	Percentage not met
Prostate V100%	$\geq$ 90%	123	95.35%	6	4.65%
Prostate V150%	45 - 65%	91	70.54%	38	29.46%
Prostate D90%	100 - 125%	112	86.82%	17	13.18%

Table 3.4 summarizes the achievement of post-implant dosimetry constraints for the prostate. A similar percentage of patients met the prostate V100% post-implant constraint as compared to the pre-implant constraint. However, the percentage of patients achieving prostate V150% post-implant was approximately 10% lower than those meeting the pre-implant target, despite the less stringent nature of the post-implant dosimetry constraints.

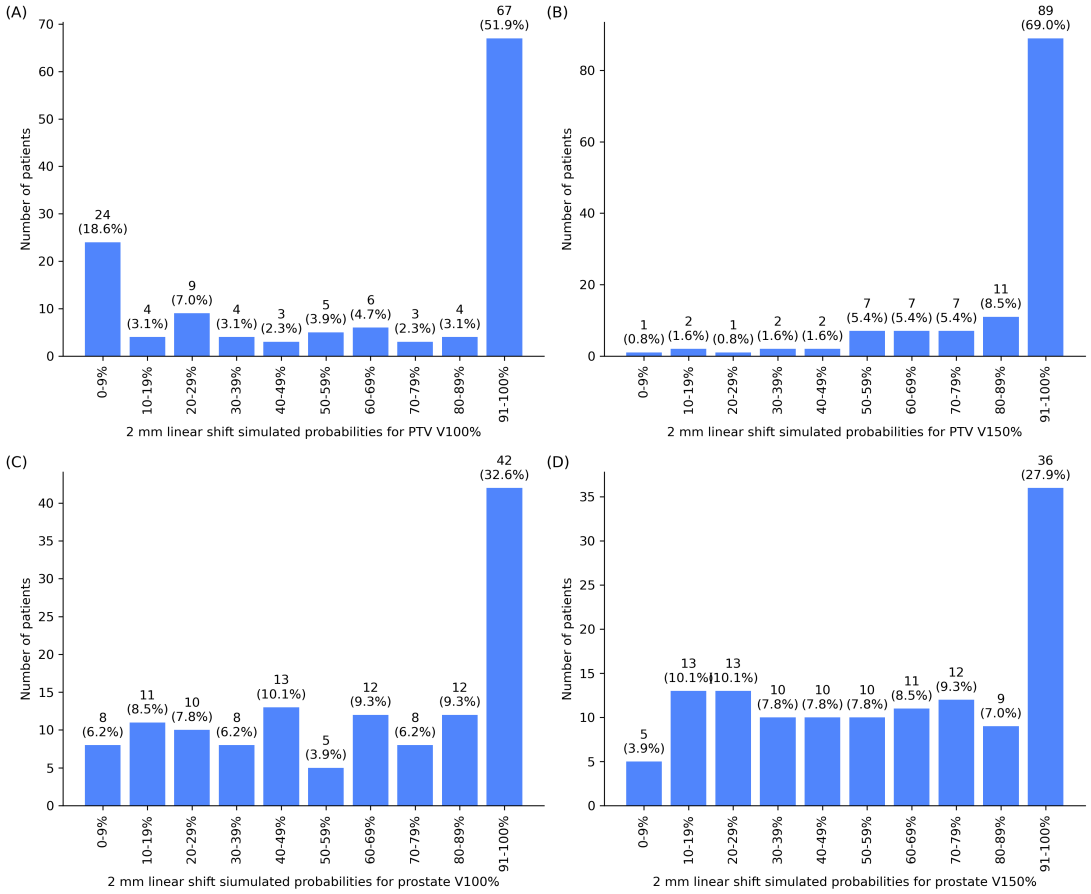

Figure 3.2: Python-based in-house software distribution of simulated probabilities for a 2 mm linear shift in seed displacement in achieving pre-implant dosimetry constraints for (A) PTV V100%, (B) PTV V150%, (C) Prostate V100%, and (D) Prostate V150%. Each bar represents the number of patients corresponding to specific probability intervals.

The distribution of simulated probabilities for achieving pre-implant target dosimetry constraints under a 2 mm seed shift is shown in Figure 3.2. For PTV V100% (Figure 3.2A), the majority of patients (51.9%) had probabilities in the 91 - 100% range, though a notable portion (18.6%) fell within the lowest 0 - 9% range, indicating a degree of sensitivity to seed placement variability. In contrast, PTV V150% (Figure 3.2B) demonstrated an exponential-like distribution, with a sharp concentration of probabilities in the 91 - 100% range, where 69.0% of patients achieved this threshold. This indicates that the PTV V150% constraint may be less sensitive to uncertainties in seed placement and is a more reliable metric for assessing the successful achievement of post-implant dosimetry constraints. Prostate V100% (Figure 3.2C)

had a more scattered distribution, with only 32.6% of patients in the 91 - 100% range. Similarly, prostate V150% (Figure 3.2D) showed a relatively even distribution, with 27.9% of patients in the highest probability range. The exponential-like concentration of probabilities for PTV V150% highlights its robustness to seed placement variability suggesting it could serve as a reliable predictor for post-implant dosimetry constraints, whereas the more scattered distributions for PTV V100%, Prostate V100%, and Prostate V150% indicate that these metrics are more sensitive to seed placement variability.

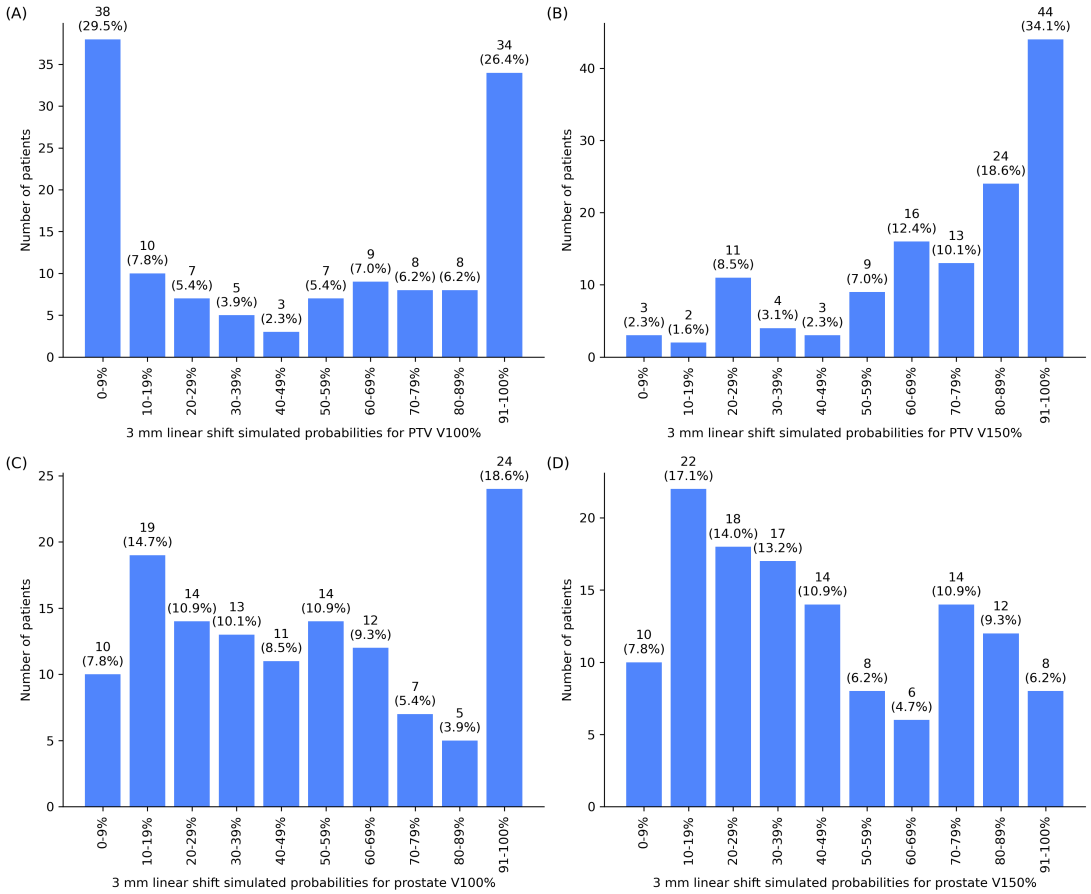

Figure 3.3: Distribution of simulated probabilities for a 3 mm linear shift in seed displacement in achieving pre-implant dosimetry constraints for (A) PTV V100%, (B) PTV V150%, (C) prostate V100%, and (D) prostate V150%. Each bar represents the number of patients corresponding to specific probability intervals.

A 3 mm linear shift was also simulated and the resulting BrachyVIC-3D probabilities for the pre-implant dosimetry constraints are depicted in Figure 3.3. Figures Fig-

ure 3.3A and Figure 3.3C show a more scattered distribution of probabilities for PTV V100% and Prostate V100%, with 26.4% and 18.6% of patients, respectively, achieving simulated probabilities in the 91-100% range. Prostate V150% (Figure 3.3D) also exhibited a dispersed distribution, with only 6.2% of patients reaching the highest probability range. However, PTV V150% (Figure 3.3B) still demonstrated an exponential-like distribution, with 34.1% of patients in the 91 - 100% range, reinforcing its stability and reliability under seed placement uncertainties, even with a larger shift. This further emphasizes that PTV V150% may be an acceptable indicator for predicting successful achievement of post-implant dosimetry constraints.

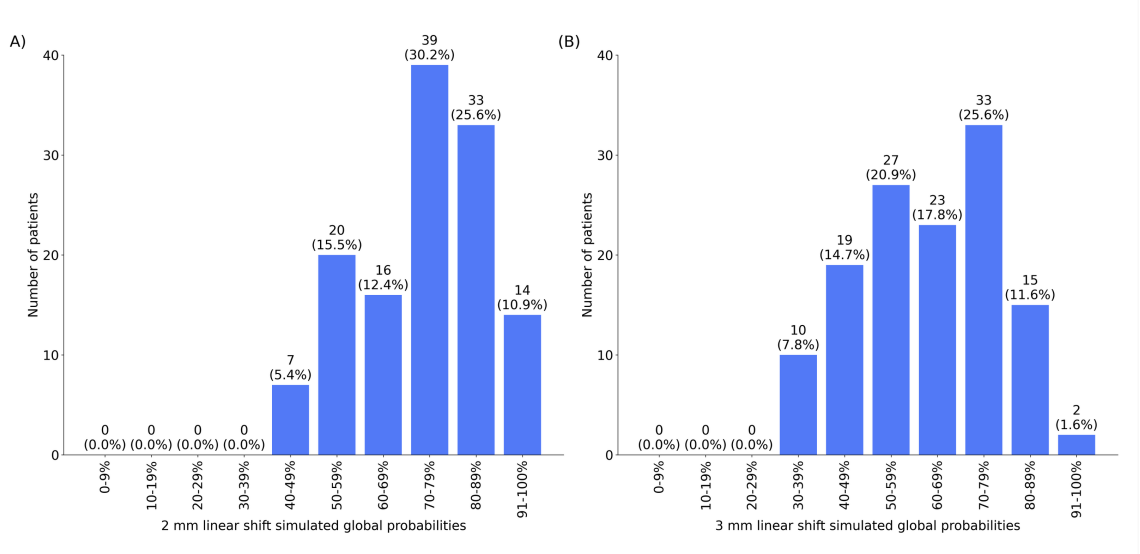

Figure 3.4: Distribution of simulated global probabilities for (A) 2 mm linear shift in seed displacement in achieving all pre-implant target dosimetry constraints and (B) 3 mm linear shift in seed displacement in achieving all pre-implant target dosimetry constraints. Each bar represents the number of patients corresponding to specific probability intervals.

Figure 3.4 presents the simulated global probabilities for achieving all pre-implant dosimetry constraints under 2 mm and 3 mm linear shifts. In the case of the 2 mm shift (Figure 3.4A), the distribution showed a strong concentration of probabilities between 70 - 89%, with 30.2% of patients in the 70 - 79% range and 25.6% in the 80 - 89% range, exhibiting a bell-shaped or normal-like distribution. For the 3 mm shift (Figure 3.4B), the distribution shifted slightly, with a broader spread and fewer patients achieving high probabilities. The majority of patients fell within the 50 - 79% range. This shift indicates a more dispersed distribution, with only 1.6% of patients achieving

probabilities in the 91 - 100% range under the 3 mm shift, suggesting increased variability in achieving global dosimetry constraints as seed placement uncertainty increases.

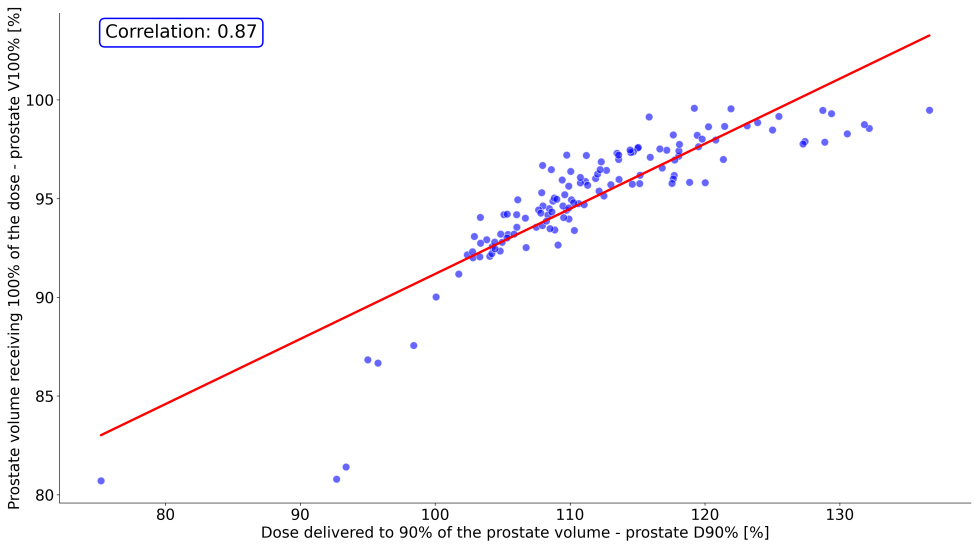

Figure 3.5: Correlation between post-implant dosimetry constraints, prostate V100% and prostate D90% dosimetry constraints. The linear regression fit is represented by the red line.

The correlation between the dose delivered to 90% of the prostate volume (D90%) and the prostate volume receiving 100% of the prescribed dose (V100%) was evaluated, yielding a strong positive correlation coefficient of 0.87, as shown in Figure 3.5. This high degree of correlation suggests that either metric can be reliably used as a predictive endpoint for the optimal probability thresholds. Given the strong correlation, predicting one variable allows for the accurate estimation of the other, thus offering flexibility in choosing the most appropriate dosimetric measure based on clinical preferences or specific treatment goals. Both prostate D90% and V100% represent strong indicators of treatment quality, and this correlation further validates the robustness of using either metric as the primary target for evaluating treatment quality.

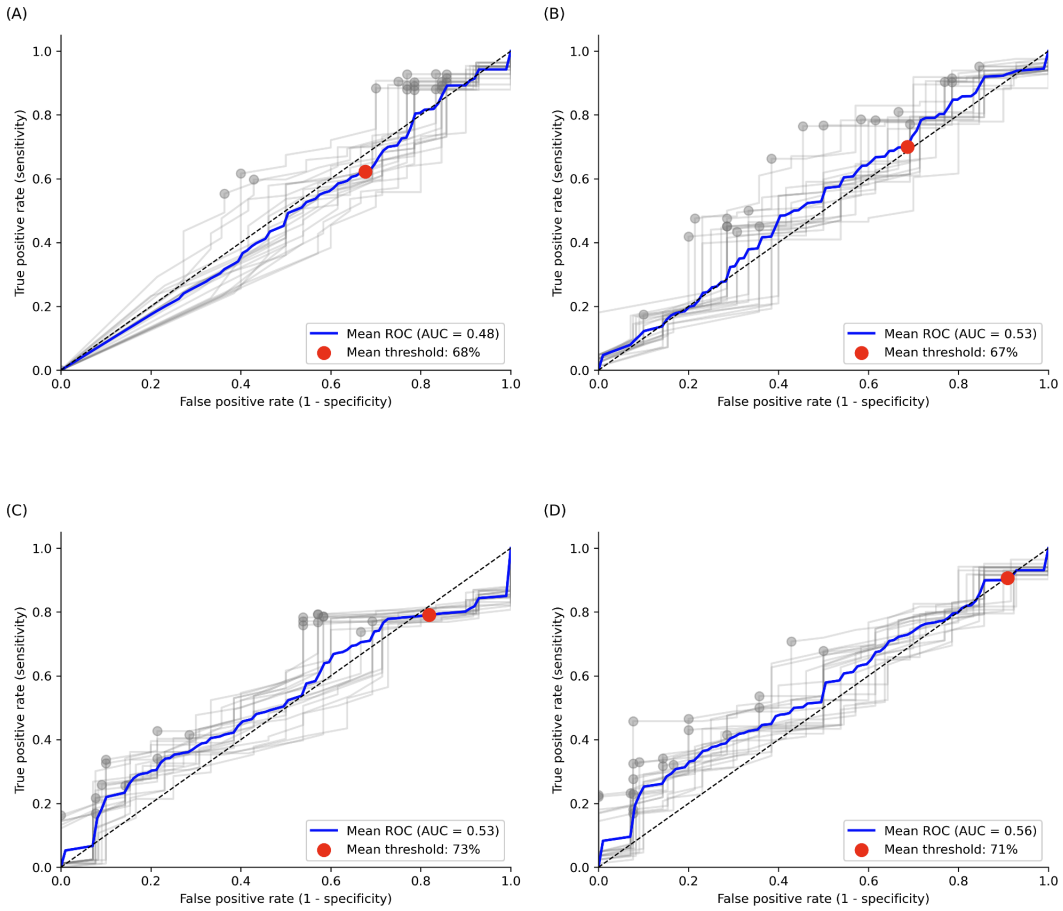

Figure 3.6: Receiver Operating Characteristic (ROC) Curves for predicting the achievement of post-implant dosimetry objective, prostate D90% thresholds using (A) 2 mm simulated probabilities for PTV V150%, (B) 3 mm simulated probabilities for PTV V150%, (C) 2 mm simulated global probabilities and (D) 3 mm simulated global probabilities. Grey lines represent the ROC curves from 20 different iterations, and the grey dots indicate the thresholds from each iteration. The blue curves represent the mean ROC across all iterations, and the red dot marks the mean threshold. The dotted line represents the line of no discrimination, indicating a model's performance equivalent to random chance.

Figure 3.6 displays the Receiver Operating Characteristic (ROC) curves for predicting post-implant D90% thresholds across different dosimetric parameters and seed shift conditions.Figure 3.6A shows the ROC curve for 2 mm simulated probabilities for PTV V150%, with a mean AUC of 0.48 and a mean threshold of 68%. Figure Figure 3.6B reflects the 3 mm simulated probabilities for PTV V150%, with a higher mean AUC of 0.53 and a mean threshold of 67%. Figure 3.6C depicts the 2 mm sim-

ulated global probabilities, with an AUC of 0.53 and a mean threshold of 73%, while Figure 3.6D shows the 3 mm simulated global probabilities, achieving the highest AUC of 0.56 and a mean threshold of 71%. In each subplot, the blue lines represent the mean ROC curve across 20 iterations, and the red dots highlight the mean threshold values. These results illustrate the variation in predictive performance for different simulated probabilities for the pre-implant dosimetry constraints.

Table 3.5 provides a comprehensive overview of threshold performance based on simulated probabilities for achieving the post-implant dosimetry constraint, prostate D90%, under 2 mm and 3 mm linear seed shifts for PTV V150% and global probabilities. The 2 mm linear shift for PTV V150% demonstrated the best overall performance, with a mean threshold value of 67± 13%. It achieved an accuracy of 0.72 ± 0.15, precision of 0.85 ± 0.07, recall of 0.80 ± 0.15, and an F1-score of 0.82 ± 0.12. The relatively low variability in performance metrics for this threshold suggests that it provides a robust balance between correctly identifying plans that meet prostate D90%.

Table 3.5: Summary of descriptive statistics for identifying optimal threshold probabilities for post-implant dosimetry constraints (prostate D90%) based on 20 iterations of training and validation sets.

Evaluation Metric	Mean	Median	Minimum	Maximum	Standard Deviation
2 mm linear shift simulated probabilities for PTV V150%					
Threshold value	68%	60%	60%	96%	13%
Accuracy	0.72	0.79	0.36	0.85	0.15
Precision	0.85	0.87	0.65	0.93	0.07
Recall	0.80	0.86	0.40	0.93	0.15
F1-score	0.82	0.88	0.53	0.92	0.12
AUC	0.48	0.48	0.39	0.56	0.05
3 mm linear shift simulated probabilities for PTV V150%					
Threshold value	67%	68%	24%	98%	24%
Accuracy	0.56	0.56	0.27	0.82	0.18
Precision	0.86	0.87	0.75	1.00	0.06
Recall	0.58	0.57	0.12	0.90	0.25
F1-score	0.66	0.68	0.20	0.90	0.19
AUC	0.53	0.53	0.44	0.62	0.05
2 mm linear shift simulated global probabilities					
Threshold value	73%	72%	62%	89%	12%
Accuracy	0.50	0.56	0.21	0.79	0.19
Precision	0.87	0.88	0.75	1.00	0.07
Recall	0.50	0.58	0.10	0.86	0.27
F1-score	0.59	0.70	0.19	0.87	0.24
AUC	0.53	0.53	0.46	0.58	0.04
3 mm linear shift simulated global probabilities					
Threshold value	71%	73%	57%	78%	6%
Accuracy	0.57	0.58	0.36	0.73	0.09
Precision	0.87	0.85	0.77	1.00	0.07
Recall	0.60	0.61	0.36	0.77	0.12
F1-score	0.70	0.71	0.49	0.83	0.09
AUC	0.56	0.56	0.50	0.64	0.04

For the 3 mm linear shift simulated probabilities for PTV V150%, the mean

threshold value was 67 ± 24%. Accuracy for this threshold dropped to 0.56 ± 0.18, with a recall of 0.58 ± 0.25, but precision remained high at 0.86 ± 0.06. For the global probabilities, the 2 mm shift had a mean threshold of 73 ± 12%, with lower accuracy (0.50 ± 0.19), recall (0.50 ± 0.27), and an F1-score of 0.59 ± 0.24. The 3 mm global shift exhibited slightly better performance, with a mean threshold of 71 ± 6%, accuracy of 0.57 ± 0.09, and an F1-score of 0.70 ± 0.09. These results suggest that the 2 mm PTV V150% threshold provides the most reliable predictor of post-implant prostate D90% success, with lower variability and better overall performance compared to global probabilities.

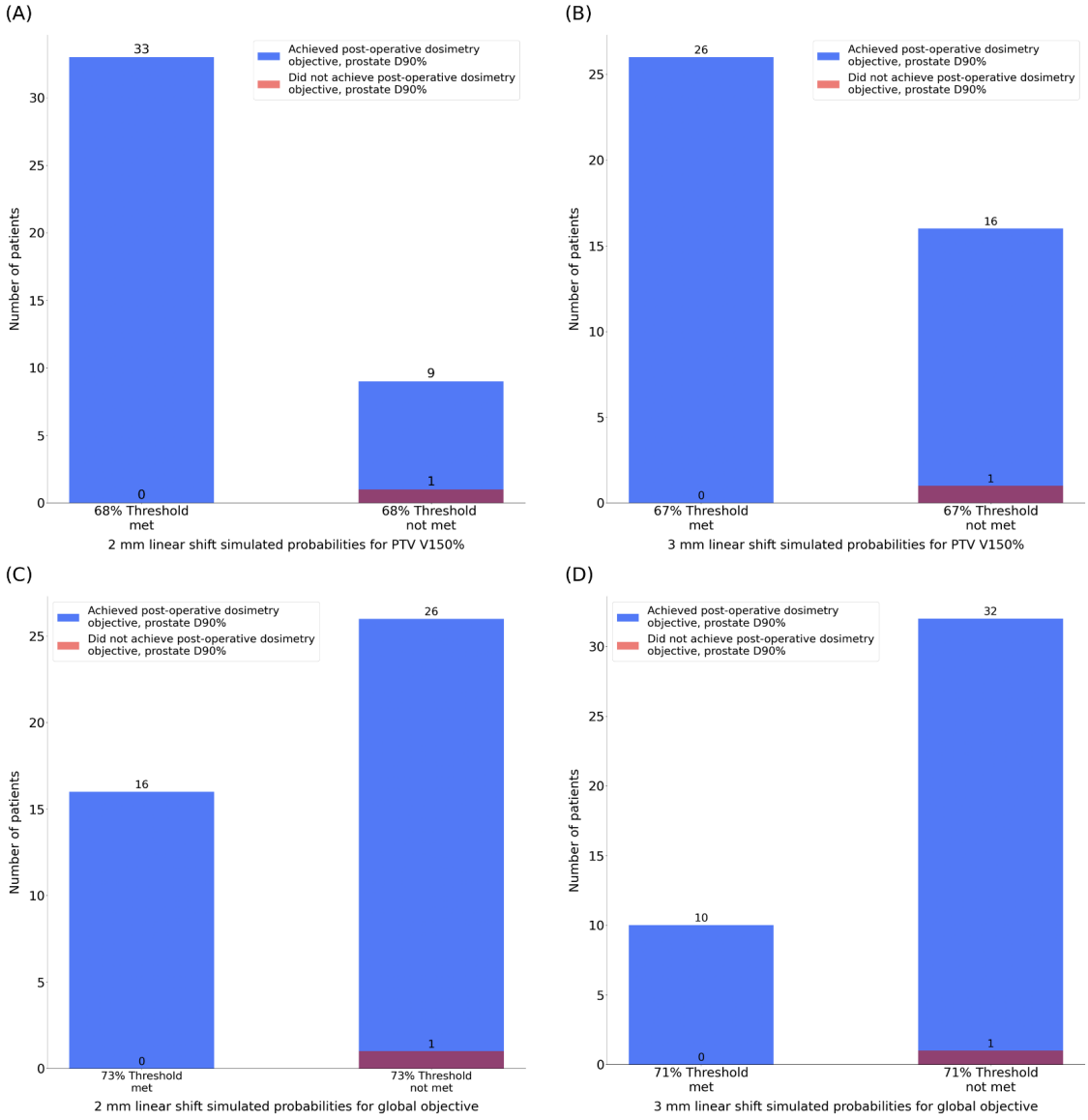

Figure 3.7: Testing thresholds for post-implant dosimetry objective prostate D90% achievements with (A) 67% threshold for 2 mm simulated probability for PTV V150%, (B) 66% threshold for 3 mm simulated probability for PTV V150%, (C) 73% threshold for 2 mm simulated global probability, and (D) 71% threshold for 3 mm simulated global probability.

Figure 3.7 shows the results of threshold testing for 2 mm and 3 mm linear shifts, examining both PTV V150% and global simulated probabilities. The 2 mm PTV V150% probability threshold (Figure 3.7A) demonstrated the best balance between specificity and sensitivity, where all 33 patients who met the threshold successfully

achieved the post-implant constraint, with no false positives. However, the threshold failed to correctly identify 9 patients who successfully achieved the post-implant constraint, classifying them as false negatives. In comparison, the 3 mm PTV V150% probability threshold (Figure 3.7B) identified fewer patients, failing to identify 16 patients who achieved the constraint, suggesting that the 2 mm threshold is less restrictive while maintaining high predictive accuracy. The global constraint thresholds (Figure 3.7C and Figure 3.7D) showed similar trends, with the 2 mm global probability threshold missing 26 patients and the 3 mm global probability threshold missing 32 patients that both global thresholds identified fewer successful cases. Overall, the 2 mm PTV V150% probability threshold is identified as the optimal threshold, providing perfect specificity and a manageable number of false negatives, making it the most effective for predicting the likelihood of achieving post-implant dosimetry constraint.

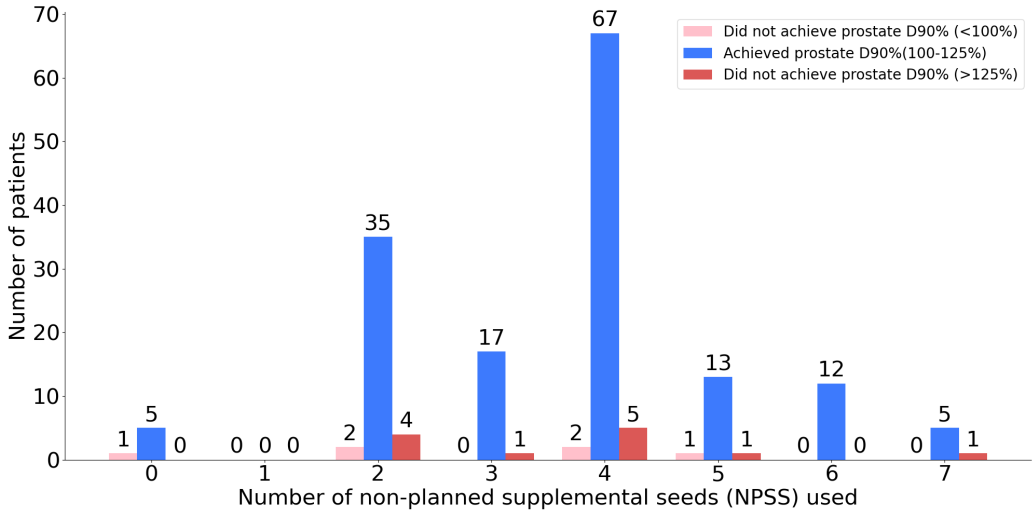

Figure 3.8: Distribution of patients based on non-planned supplemental seeds (NPSS) used and post-implant dosimetry objective, prostate D90%, achievement. The blue bars represent patients who achieved the prostate D90% (100-125%), the pink bars represent patients who did not achieve prostate D90% ($< 100\%$), and the red bars represent patients who exceeded the prostate D90% objective ($> 125\%$).

Figure 3.8 demonstrates the distribution of patients based on the number of NPSS used and their corresponding achievement of the prostate D90% constraint. The data show no clear correlation between the number of NPSS used and the success of achieving the D90% target. The results indicate no significant correlation between the number of NPSS used and the likelihood of meeting or exceeding the prostate D90%

constraint. While most patients fell within the target range (100 - 125%) across all NPSS categories, a small number of patients did not achieve the D90% target, particularly at NPSS counts of 0, 1, 3, and 5. Across all NPSS categories, patients in each group (below 100%, between 100 - 125%, and above 125%) are distributed without a consistent trend. This suggests that the number of NPSS used does not significantly impact the likelihood of meeting or exceeding the D90% dosimetry goal.

3.4 Discussion

3.4.1 Predictive performance of threshold values and their clinical relevance

LDR prostate brachytherapy using pre-implant dosimetric metrics, specifically the probabilities calculated from our in-house dose calculation engine can be used to determine the reliability of achieving post-implant constraints. These probabilities represent the likelihood of meeting the pre-implant dosimetry constraints and the probability of achieving all pre-implant target dosimetry constraints represented as the global probability. Specifically, probabilities calculated for PTV V150% and the global probabilities regarding a 2 mm and 3 mm linear shift were found to be strong predictors, as they showed reliable predictive probability distributions. The threshold values identified in this study provide critical insights into predicting post-implant dosimetry constraint, prostate D90%, achievement.

For a 2 mm linear shift in simulated probability for PTV V150%, the optimal threshold was 68 ± 13%, while for a 3 mm linear shift, the threshold was slightly higher at 67 ± 24%. In terms of global probabilities, the 2 mm linear shift had a threshold of 73 ± 12%, and the 3 mm linear shift global probability threshold was 71 ± 6%. These threshold values offer a reliable means of predicting the achievement of post-implant dosimetry constraint prostate D90%, particularly the 2 mm PTV V150% threshold performing the best overall shown in Figure 3.7A. This threshold shows the greatest potential for clinical application due to its accuracy and stability in predicting the achievement of post-implant dosimetry constraint prostate D90% compared to the other thresholds. However, it is important to recognize that popu-

lation data serves as a foundational guide rather than an absolute directive. While the thresholds provide valuable insights on the treatment plan's reliability of achieving prostate D90%, clinical decisions must still incorporate individual patient factors. Personalizing the treatment plan based on specific patient anatomy and procedural considerations remains essential for optimizing treatment quality.

3.4.2 Generalizability of methodology and thresholds

When interpreting the results of the identified dosimetric thresholds, it is crucial to recognize that while these thresholds offer predictive value for achieving post-implant dosimetry constraint, they are not foolproof. Specifically, there are cases where patients who ultimately achieved the prostate D90% constraint did not meet the simulated threshold. For instance, the threshold for a 2 mm linear shift in PTV V150% is set at 68 ± 13%, and while it provides a precision of 85%, there remains a subset of patients who successfully achieved the prostate D90% constraint without meeting this threshold. This implies that the threshold, while useful in predicting dosimetric success, can miss some true positives (i.e., patients who achieve D90%), highlighting the possibility of false negatives. In such cases, the sensitivity of the threshold is less than ideal because not all patients who achieve the D90% constraint is captured by the threshold.

Similarly, the threshold for a 3 mm linear shift in PTV V150% is 67 ± 24%, with a precision of 86%. However, as with the 2 mm shift, patients who did achieve the post-implant dosimetry constraint occasionally fell below the threshold, resulting in false negatives. The thresholds for global probabilities at 2 mm and 3 mm shifts also exhibit this pattern, with thresholds of 73 ± 12% and 71 ± 6%, respectively, and precisions of 87%.

These false negatives indicate that relying solely on threshold values could result in missing patients who actually achieve their dosimetry constraints. Therefore, although the thresholds demonstrate strong predictive power, particularly in terms of precision, clinicians must be aware that some patients who achieve post-implant success may not meet the threshold, reinforcing the importance of incorporating clinical judgment and individual patient factors into treatment planning. The occurrence of such false negatives highlights the need for a more comprehensive evaluation beyond

just the threshold predictions to ensure optimal patient outcomes.

3.4.3 The role of prostate D90% as a dosimetric indicator

Both prostate D90% and V100% were considered as potential dosimetric endpoints in this analysis, given their strong clinical relevance. A strong correlation was observed between them ($r = 0.87$), indicating a close association and suggesting that either metric could serve as a predictive measure for treatment evaluation. However, this relationship may not be strictly linear and could follow an alternative trend particularly at lower dosimetric values. As such, further data and analysis would be valuable to better characterize the nature of this relationship.

Despite their correlation, D90% was selected as the primary focus in this study due to a higher number of patients failing to meet this constraint compared to V100%. This provided a more informative basis for establishing thresholds, as the greater number of failed D90% cases allowed for a more conservative and better determination of an optimal threshold. Although D90% is widely recognized as a critical metric, its higher failure rate in this cohort made it the more practical choice for assessing post-implant dosimetry achievement.The role of prostate D90% as a dosimetric goal in LDR brachytherapy, however, continues to prompt critical evaluation. Several studies have questioned the consistency of D90% as a reliable predictor of treatment success across different clinical contexts.[139–141] Yi Su et al. reinforced the importance of maintaining an appropriate seed count to moderate variability in prostate D90%.[139] Their findings complement our observations, suggesting that even minor deviations in D90% can still preserve treatment efficacy, provided that a strategic seed placement plan is followed. This flexibility within defined dosimetric constraints highlights the adaptability of our in-house dose engine to accommodate procedural variability, ensuring robust treatment outcomes without overly rigid criteria.

Morris WJ et al. further complicate the discussion regarding the utility of D90% as an indicator of treatment success, noting that while lower D90% values are associated with higher recurrence risks, the broad application of D90% as a predictor of disease-free survival is limited.[140] Their findings advocate for a nuanced, institution-specific approach to D90%, emphasizing the shift toward personalized medicine in oncology. This aligns with our findings, suggesting that dosimetric parameters like D90% should

be integrated with clinical outcomes and institutional practices rather than viewed in isolation.

Additionally, Todor et al. demonstrated that slight deviations in seed placement do not necessarily compromise treatment efficacy, reinforcing the idea that D90% should be interpreted with flexibility.[141] This underscores the need for treatment strategies that balance precision in achieving target dosimetry with adaptability to accommodate patient-specific factors. The minor variations in D90% observed within our study indicate the inherent uncertainties of seed placement, which, despite careful planning, remain a challenge in achieving consistent dosimetry. These uncertainties in seed position highlight the importance of tailored approaches that prioritize patient-specific outcomes while avoiding rigid adherence to dosimetric targets that may risk overdosing critical structures.

3.4.4 Non-Planned Supplemental Seeds (NPSS)

The decision to use NPSS during seed implantation, guided by the RO's expertise, offers crucial flexibility in addressing areas that might not receive adequate coverage due to procedural uncertainties. Although NPSS is intended to enhance dose coverage, our findings suggest that the number of NPSS used does not significantly correlate with the achievement of the prostate D90% constraint (Figure 3.8). Regardless of whether few or many NPSS are used, the likelihood of meeting the D90% dosimetric goal remains relatively unchanged. This indicates that the number of seeds alone does not strongly influence dosimetric success, highlighting the greater importance of factors such as the RO's judgment, seed placement strategy, and the positioning of seeds relative to others in achieving optimal dosimetric outcomes.

While NPSS can improve coverage, caution is necessary to avoid exceeding dosimetric constraints for both the target and organs-at-risk (OARs). These findings align with broader research, such as that by Yi Su et al., which emphasizes the importance of optimizing seed quantity to reduce variability in dosimetric parameters like prostate D90%.[139] The number and placement of seeds, both planned and supplemental, play a critical role in the overall success of treatment, underscoring the need to carefully consider these factors throughout the implantation process. However, our in-house software only accounts for seed shifts and not the addition of extra

seeds, suggesting that NPSS may affect the probability of achieving prostate D90% by altering the final dosimetry distribution.

3.4.5 Limitations and future directions

The implications of our findings on simulated probabilities for pre-implant dosimetric constraints and their precision in achieving post-implant dosimetry constraint, prostate D90%, highlight the importance of considering the generalizability of our in-house developed software and methodologies to other clinical settings. While the probabilistic approach and the relationships identified between seed placement accuracy and dosimetry constraints are broadly applicable to radiation oncology, the specific thresholds and probability percentages identified may vary across different institutions. This variability can arise from differences in equipment, treatment protocols, imaging techniques, planning algorithms, RO expertise, and patient anatomy, which may affect the direct application of our results elsewhere. Additionally, differences in how ROs approach seed placement, as well as institutional preferences regarding the use of NPSS, could lead to variability in treatment outcomes, further emphasizing the need for localized refinement of the thresholds identified in this study.

An important consideration in interpreting these findings is the imbalance in our patient cohort. The majority of patients in the cohort successfully achieved the post-implant dosimetry constraints, resulting in a smaller number of failed cases (patients not meeting prostate D90% or V100% constraints). This group imbalance can significantly affect the AUC of the ROC curves by compromising the threshold's ability to effectively differentiate between patients who achieve prostate D90% and those who do not. When one group predominates, the threshold's sensitivity to the minority group is diminished, leading to disproportionately high false positive rates or an inadequate representation of true negative rates, which generally will result in lower AUC scores as evidenced in Table 3.5. Furthermore, this imbalance can influence the precision and sensitivity of the thresholds, as fewer examples of failure may limit the robustness of predictions for patients at risk of not achieving these constraints. The predictive models may therefore be biased toward identifying successful outcomes, and the thresholds may not generalize as effectively to cohorts with a more balanced distribution of outcomes. This highlights the need for caution when applying

these thresholds in other settings or patient populations, as different distributions of successes and failures could impact the effectiveness of the simulated probabilities evidenced in Table 3.5, where 20 different training sets were used. It is suggested that each institution train a dataset using pre-implant and post-implant plans tailored to their own cases. Future studies should aim to incorporate more balanced datasets to improve the generalizability and accuracy of the predictive thresholds across diverse clinical environments.

While our probabilistic model demonstrates promise, it is important to acknowledge that more advanced and powerful modeling approaches exist for characterizing uncertainty. These include Bayesian frameworks, ensemble learning techniques, or deep learning models that incorporate uncertainty quantification. Such methods may offer improved performance in handling small datasets and imbalanced classes. These approaches will be explored in future studies to further enhance predictive accuracy and clinical applicability.

3.5 Conclusions

The in-house LDR brachytherapy dose calculation software demonstrated its capability to generate reliable 3-D dose distributions, using seed positions to calculate the probability of achieving specified post-implant dosimetry constraints. Our findings indicate that the pre-implant probability threshold for achieving the post-implant dosimetry constraint, prostate D90%, is 68 $\pm$ 13% for a 2 mm linear shift when considering the PTV V150% simulated probability. This threshold provides a reliable predictor of treatment plan success, with a precision of 85%, meaning that plans achieving this threshold have an 85% likelihood of successfully meeting the prostate D90% constraint. While this threshold offers a robust tool for optimizing the reliability of achieving the post-implant dosimetry constraint, it is essential to acknowledge the inherent uncertainties and variability associated with seed placement and procedural factors. The standard deviation highlights the variability in predicting outcomes, underscoring that while the identified threshold provides valuable guidance, it does not guarantee success in achieving prostate D90%. Incorporating this 2 mm PTV V150% threshold into clinical practice can enhance the decision-making process during treatment planning, allowing radiation oncologists and medical physicists

to make informed adjustments based on real-time data. However, the achievement of post-implant dosimetry constraints continues to depend heavily on the clinical judgment of the radiation oncologist, who must balance probabilistic thresholds with patient-specific anatomical and procedural considerations.

Chapter 4

Enhancing dose gradients in gynecological cancer treatment planning: impact of normal tissue objectives and concentric ring structures on dose gradients in volumetric modulated arc therapy planning

4.1 Introduction

Radiation therapy is essential for the effective treatment of gynecological cancers, which are particularly challenging due to the close proximity of the reproductive organs to critical structures like the bladder, rectum, and bowel. Considering that 1 600 Canadian women are expected to be diagnosed with cervical cancer and approximately 8 600 are expected to be diagnosed with uterine and endometrial cancer this year, there is a critical need for highly effective treatment strategies[142]. These strategies

must be meticulously created to ensure effective tumour targeting while minimizing damage to surrounding healthy tissues. The complexity of these tumours, coupled with their significant impact on women's health, emphasizes the need for advanced radiation therapy techniques that balance treatment efficacy with patient safety.

External beam radiation therapy (EBRT) is one of the common treatment modalities for managing gynecological cancers. Recent advancements in EBRT have led to the development of several techniques that optimize dose distributions and enhances organ-at-risk (OAR) sparing, which are particularly beneficial for these cancers. Techniques such as intensity-modulated radiation therapy (IMRT), volumetric modulated arc therapy (VMAT), and image-guided radiation therapy (IGRT) have shown to have high precision in dose delivery.[143–146] These methods, coupled with accurate patient positioning, have been shown to ensure precise control over where radiation doses are delivered, effectively targeting tumours while minimizing risk to OARs.[147,148] Guidelines such as the Gynecological Cancer (GEC) guidelines by the European Society for Radiotherapy and Oncology (ESTRO), particularly the European MRI-guided Brachytherapy in Cervix Cancer (EMBRACE), emphasize the significance of these strategies. These guidelines have provided comprehensive recommendations for cervical cancer, focusing on treatment outcomes, dosimetry, and comparisons of different radiotherapy techniques.[67–70] By following these guidelines, the delicate balance between delivering effective tumour doses and sparing OARs can be better managed, helping to prevent severe side effects such as radiation cystitis, enteritis, and proctitis. These complications can significantly impact a patient's quality of life.[59–63] Through these comprehensive guidelines and techniques, treatment plans can be created to achieve the most favorable therapeutic outcomes, emphasizing the importance of precision.

In addition to advanced delivery techniques and evidence-based guidelines, radiotherapy planning techniques have been developed to optimize dose gradients around the tumour while minimizing exposure to surrounding healthy tissues. Dose gradient optimization ensures a steep fall-off in radiation doses outside the target, balancing tumour coverage with OAR sparing. Two key methods used in this process are the Normal Tissue Objective (NTO) and concentric ring structures (CRS). The NTO, a feature in Varian's Eclipse^{TM} treatment planning system, allows precise control over the dose gradient by adjusting parameters such as start dose, distance from the target

(DFT), and fall-off rate.[78,79] CRS, also known as dosimetric shells, involves creating concentric regions around the target, with each ring assigned a specific dose objective to refine the dose gradient.[86,87] These planning techniques are particularly vital in gynecological treatment plans, where the proximity of multiple OARs requires meticulous optimization to ensure both treatment efficacy and patient safety. Research has shown that manual optimization of NTO parameters leads to superior target coverage and reduced doses to OARs compared to automatic settings.[149,150] This thoughtful application of the NTO can significantly enhance treatment outcomes, especially in complex cases involving tumours in the endometrium, cervix, prostate, lung, and brain.[149–154] However, the effectiveness of the NTO is contingent upon the tumour site and clinical needs, requiring continuous refinement to determine the optimal combination of parameters for each specific location. Establishing these optimal settings provides a reliable starting point for treatment planning, potentially minimizing the need for further adjustments and allowing for more efficient, tailored therapeutic strategies. While many studies have focused on varying the fall-off parameter in combination with high start doses and shorter start distances to achieve aggressive dose distributions, it may also be valuable to explore less stringent combinations.[150,152,154] Using a lower start dose with a larger start distance could result in a more gradual dose fall-off, potentially enhancing OAR sparing while still maintaining adequate tumour coverage.

Similarly, CRS has shown to be highly effective in enhancing radiotherapy treatment planning by improving dose control and sparing OARs.[86,87,155] Studies have also demonstrated the use of CRS to improve the conformity of the radiation dose to the cervical targets, which are often characterized by complex geometries.[156,157] Additionally, CRS has shown significant benefits in lung cancer cases treated with stereotactic body radiotherapy (SBRT), where sharp dose fall-offs are critical for delivering high while protecting surrounding tissues.[86] Furthermore, research has explored optimal shell parameters, such as ring width, number of rings, and dose fall-off rates, revealing their impact on treatment plan quality and target conformity.[86,88,158] These findings support the effectiveness of CRS in achieving safer and more precise radiotherapy outcomes by optimizing dose gradients. While both NTO and CRS have been shown to be effective at optimizing dose gradients, a systematic comparison of their relative performance remains to be conducted.

This study focuses on systematically evaluating the strengths and limitations of the NTO and CRS in optimizing dose gradients for gynecological cancer treatment plans. By comparing these two optimized approaches, the study provides a detailed and systematic analysis of their optimal parameters, advantages, and limitations in achieving precise dose gradients that ensure target coverage while sparing adjacent OARs. The findings aim to improve the precision and safety of external beam radiotherapy (EBRT) in clinical practice, ultimately enhancing radiotherapy outcomes for patients with gynecological cancers.

4.2 Materials and methods

4.2.1 Patient cohort and treatment

Fifteen patients with gynecological tumours previously treated at BC Cancer Victoria, British Columbia were retrospectively selected for this study. Representing approximately 12–15% of the clinic's annual gynecological cancer cases, this cohort reflects a diverse range of treatment complexities including cervical, endometrial, and uterine tumours. Each patient was prescribed a total dose of 45 Gy, delivered using volumetric modulated arc therapy (VMAT). Treatment plans used two full 360° arcs at 6 MV and were optimized for TrueBeam linear accelerators (Varian Medical Systems).

All treatment plans were created and optimized using the Eclipse^{TM} treatment planning system (TPS), version 18.0 (Varian Medical Systems). The Photon Optimizer (PO), version 18.0, was utilized for plan optimization while final dose calculations were performed using the Anisotropic Analytical Algorithm (AAA), version 18.0. No plans were paused or adjusted during optimization. Treatment plans were optimized using manual NTO and CRS. Plans optimized without any CRS or NTO were used as a baseline for comparison. In Eclipse^{TM}, the normalization factor is applied to the dose distribution after optimization to ensure that the target meets the prescribed dose coverage. All plans were normalized so that 95% of the prescribed dose covered 98% of the planning target volume (PTV) after optimization and final dose calculation.[64]

4.2.2 Target optimization objectives

Within the optimizer, optimization objectives were established to ensure adequate dose coverage to the target volumes, incorporating both upper and lower dose-volume optimization objectives used at the institution.[64,65] Target structures include: the planning target volume (PTV), clinical target volume (CTV) and internal target volume (ITV). Target structures with 'n' and 'p' refer to nodal and primary target volumes, respectively, indicating whether the structure is associated with lymph node regions or the primary tumour site. Optimization structures, prefixed with "z" (zCTVn45, zITVp45, zPTVn45, zPTVp45, and zPTV45), were derived using Boolean operations to existing target structures as supporting structures for optimization and evaluation purposes.[64,65] Each structure was assigned specific dose-volume optimization objectives with corresponding priorities to enhance the dose distribution summarized in Table 4.1.

Table 4.1: Optimization parameters for different structures.

Optimization Structure	Objective	Volume (%)	cGy	Priority
zCTVn45	Upper	0	4815	120
	Upper	25	4725	70
	Upper	50	4650	70
	Lower	100	4500	100
zITVp45	Upper	0	4725	130
	Upper	25	4700	70
	Upper	50	4650	70
	Lower	100	4500	100
zPTVn45	Upper	0	4635	130
	Lower	99	4500	100
zPTVp45	Upper	0	4725	120
	Lower	99	4500	100
zPTV45	Upper	0	4725	120
	Lower	99	4500	100
PTV	Upper	0	4725	120
	Upper	0	4500	0*

4.2.3 Normal Tissue Objective (NTO)

The NTO, a tool within Varian's TPS, Eclipse^{TM} controls the radiation dose distribution in the treatment plan to protect surrounding healthy tissues. It can be defined as a continuous penalty function, f(x), which specifies the dose constraints at a distance, x, from the planning target volume (PTV) border, as shown:[78,79]

$$f(x) = \begin{cases} f_0 e^{-k(x-x_{\text{start}})} + f_\infty \left(1 - e^{-k(x-x_{\text{start}})}\right), & x \geq x_{\text{start}} \\ f_0, & x < x_{\text{start}} \end{cases} \tag{2.14}$$

The start dose, f_o, is the maximum dose level (%) that should not be exceeded, serving as an upper limit outside the PTV region. Conversely, the end dose, f_∞, is the minimum acceptable dose level (%) outside the PTV region, functioning as a lower limit. The start distance, x_{start}, is the distance from the target (DFT) border at which the NTO begins to enforce dose penalties (cm). The dose fall-off, k, is the rate at which the dose decreases (mm^{-1}). The priority, p is the importance of the NTO within the hierarchy of optimization objectives in the TPS optimizer.

For plans optimized with manual NTO, a priority setting of 100 was established, and an upper objective with a priority of 0 was applied to the target. This upper objective was necessary as the NTO requires an upper objective to optimize the treatment, specifically utilizing the lowest upper objective set for the target.[78,79] Two manual NTO configurations were examined: NTO #1 with $x_{\text{start}} = 0.05$ cm, $f_o = 105\%$ and $f_\infty = 40\%$, and NTO #2 with $x_{\text{start}} = 0.3$ cm, $f_o = 95\%$ and $f_\infty = 40\%$. The dose fall-off (k) was adjusted across a range of values: 0.15, 0.2, 0.25, 0.3, 0.35, and 0.4 mm^{-1}. These two functions can be seen in Figure 4.1, showing their theoretical function derived from Equation 2.14.

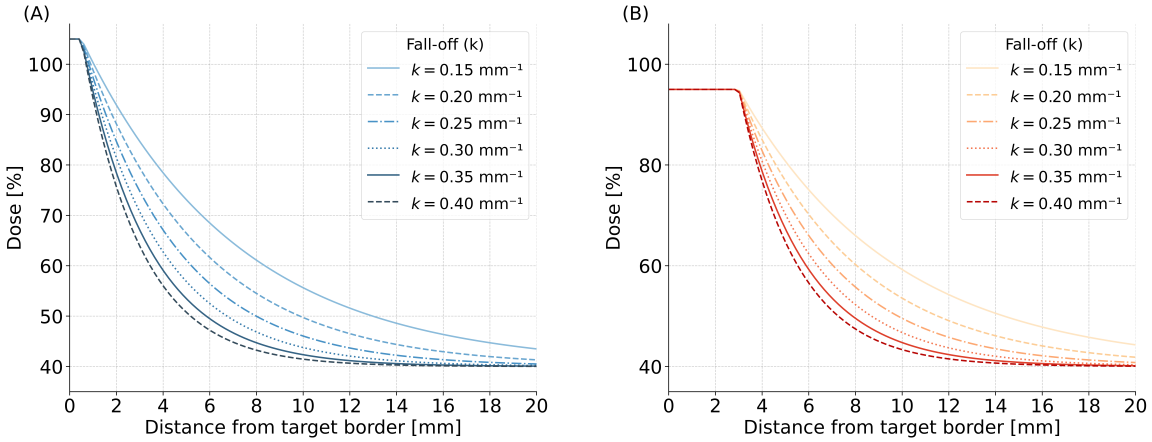

Figure 4.1: Dose fall-off profiles for normal tissue objective (NTO) configurations. (A) NTO #1 with $x_{\text{start}} = 0.05$ cm, $f_o = 105\%$ and $f_\infty = 40\%$, and (B) NTO #2 with $x_{\text{start}} = 0.3$ cm, $f_o = 95\%$ and $f_\infty = 40\%$. The dose fall-off rate (k) was varied across values of 0.05, 0.1, 0.15, 0.2, 0.25, 0.3, 0.35, and 0.4 mm^{-1}, illustrating the impact of fall-off rate on dose gradients relative to the target border.

4.2.4 Concentric Ring Structures (CRS)

Concentric ring structures (CRS) were implemented to control the dose gradient as five distinct concentric regions surrounding the target volume. Each ring had a fixed radial width of 4 mm, selected to provide sufficient spatial resolution for the gynecological anatomy while maintaining consistent dose gradient control and a manageable optimizer load. The ring configuration is shown in Figure 4.2.

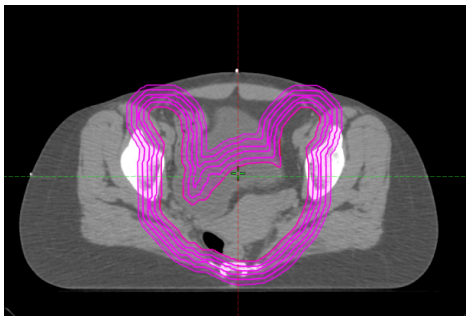

Figure 4.2: Application of CRS in Eclipse$^{\text{TM}}$ treatment planning system optimizer. Rings are contoured around the planning target volume where each ring is assigned a mean dose objective.

To evaluate the ability to control and optimize the dose gradient in the surrounding normal tissue, mean dose objectives were applied to each ring. All rings were assigned a priority of 100. Rings closer to the PTV were assigned higher mean dose objectives, while those farther away received lower mean dose objectives. The mean dose objectives for each ring were calculated based on an exponential decay function:

$$D(x) = D_0 e^{-kx} \tag{4.1}$$

where Do is the prescription dose, x is the mean distance (mm) between rings, and k (mm^{-1}) is the decay constant. The decay constant k was determined by the predefined fall-off rate being examined, calculated as follows:

$$k = \frac{\text{predefined fall-off rate}}{D_0} \tag{4.2}$$

The predefined fall-off rates examined included 0.5, 1.0, 1.5, 2.0, 2.5, and 3.0 Gy/mm, representing a range of potential dose gradients achievable in practice. In this initial evaluation, each predefined fall-off rate was uniformly applied across all rings to assess its impact on the dose gradient and treatment efficacy. These preliminary results informed the designed of a more refined optimization strategy using a piecewise function.

In this subsequent phase, combinations of predefined fall-off rates and corresponding mean dose objectives were systematically applied across the concentric rings. Specifically, steeper fall-off values were assigned to rings proximal to the target to preserve adequate target coverage, while shallower fall-off values were employed in the outer rings to avoid excessive dose build-up and ensure smoother dose gradients. Ring priorities were also adjusted to further optimize dose distribution. The balance between target conformity and hot spot mitigation was primarily achieved through the systematic adjustment of mean dose objectives defined by the piecewise function, while optimization priorities were modified to reinforce the intended dose gradient across the CRSs.

Table 4.2: Summary of concentric ring structure fall-off combinations.

Ring #	Parameter	Combination #1	Combination #2	Combination #3
Ring 1 (2 mm from target border)	Fall-off Used (Gy/mm)	–	2.5	3.0
	Mean Dose (cGy)	3780	4027	3938
	Priority	100	85	85
Ring 2 (6 mm from target border)	Fall-off Used (Gy/mm)	–	2.5	2.5
	Mean Dose (cGy)	2690	3224	3224
	Priority	100	95	95
Ring 3 (10 mm from target border)	Fall-off Used (Gy/mm)	–	2.25	2.25
	Mean Dose (cGy)	2120	2729	2729
	Priority	100	100	100
Ring 4 (14 mm from target border)	Fall-off Used (Gy/mm)	–	2.25	2.25
	Mean Dose (cGy)	1980	2235	2235
	Priority	100	95	95
Ring 5 (18 mm from target border)	Fall-off Used (Gy/mm)	–	2.0	2.0
	Mean Dose (cGy)	1881	2022	2022
	Priority	100	80	80

Three specific combination strategies were implemented to optimize the dose gradient. Combination #1 consisted of CRS that replicated the optimal NTO function to verify whether if similar dose gradients could be achieved. Combination #2 utilized a combination predefined fall-off values, specifically chosen based on their success in meeting the evaluation criteria. Building on this, Combination #3 introduced modifications to the initial ring, creating a steeper initial dose gradient to more effectively meet the established evaluation criteria. Table 4.2 provides a detailed summary of the specific fall-off values, their corresponding mean dose objectives, and the priorities assigned to each ring within each combination.

4.2.5 Evaluation of NTO and CRS

4.2.5.1 Criteria for optimum configurations of NTO and CRS

The optimal configurations for both the NTO and CRS were determined using the same evaluation criteria: conformity, maximum dose to the target, and target dose coverage. In addition, normalization and modulation factors were analyzed for each configuration to ensure clinically feasible plans with efficient delivery. These evalua-

tion criteria are summarized in Table 4.3.

Table 4.3: Dose-volume constraints for gynecological structures.

Structure/Organ	Criteria
Conformity Index #1 (C1)	≤ 1.1
Conformity Index #2 (C2)	≤ 1.55
Planning Target Volume (PTV)	$D_{max} < 4815$ cGy
	$D_{95\%} \geq 4275$ cGy
Clinical Target Volume (CTV)	$D_{98\%} \geq 4410$ cGy
Internal Target Volume (ITV)	$D_{98\%} \geq 4410$ cGy
Bladder	$V_{40Gy} < 60\%$
	$V_{30Gy} < 80\%$
Bowel	$V_{40Gy} < 300$ cm^3
	$V_{30Gy} < 650$ cm^3
Rectum	$V_{40Gy} < 75\%$
	$V_{30Gy} < 95\%$
Sigmoid	$V_{40Gy} < 80\%$

Two conformity indices were used to assess the PTV coverage by the prescribed dose. [67,70,152] Conformity index 1 (C1) is defined as the ratio of the volume receiving 95% of the prescribed dose to the target volume. Conformity index 2 (C2) is defined as the ratio of the volume receiving 80% of the prescribed dose to the target volume. Values of ≤ 1.1 and ≤ 1.55 respectively, were considered acceptable:[64,65,69]

$$C_1 = \frac{V_{95\%}}{V_{TV}} \qquad C_1 \leq 1.1 \tag{4.3}$$

$$C_2 = \frac{V_{80\%}}{V_{TV}} \qquad C_2 \leq 1.55 \tag{4.4}$$

Target dose constraints require the maximum dose to the PTV to remain below 4815 cGy while also ensuring that 95% of the PTV receives at least 4275 cGy. Addi-

tionally, at least 98% of the CTV and ITV should receive $\geq$ 4410cGy.[64,65,67,70] Since all plans were normalized to the dose coverage goal (V95% = 98% of the target), the mean doses to the CTV, ITV, and PTV served as surrogates for the coverage objective, providing a reliable measure of how effectively each configuration met the target coverage requirements.

Operational factors were also considered to ensure clinical feasibility and delivery efficiency. The normalization factor was examined to reflect the extent of scaling required for the optimizer to meet clinical dose constraints. A normalization factor close to 1.0 indicates that the desired dose distribution was achieved with minimal adjustment, while values that deviate significantly from 1.0 may suggest suboptimal optimization or the presence of trade-offs between competing planning goals. The modulation factor (MF) was assessed as a measure of delivery efficiency and plan complexity. It is defined as the ratio of the total number of monitor units (MU) to the prescribed dose per fraction:[159,160]

$$\text{Modulation Factor (MF)} = \frac{\text{Total Monitor Units}}{\text{Prescribed Dose per Fraction}} \tag{4.5}$$

The MF reflects the degree of intensity modulation required to achieve the desired dose distribution. Higher MF values indicate increased plan complexity, with more modulation and segmental variation, which may lead to longer delivery times and reduced treatment efficiency. For gynecological treatment sites, MF values between 3.0 and 4.0 are typically expected.[161]

4.2.5.2 Statistical analysis of optimal NTO and CRS

Statistical analysis was conducted on the resulting plans using the optimal configurations for the NTO and CRS. The Wilcoxon signed-rank test was used to evaluate differences in conformity, maximum dose to the target, target dose coverage, normalization, and modulation factors. Additionally, these optimal configurations were validated against dose-volume constraints for OARs, including the bladder, bowel, rectum, and sigmoid. The evaluated volume metrics for the OARs were Bladder, Bowel and Rectum V40Gy and V30Gy as well as Sigmoid V40Gy.[64,65,67,70] Detailed dose-volume metrics are provided in Table 4.3. It should be emphasized that this analysis represents a benchmarking and comparative evaluation of established dose

optimization strategies. No novel algorithmic methods were introduced in this work.

4.3 Results

4.3.1 Normal Tissue Objective (NTO) evaluations

The performance of NTO #1 and NTO #2 were evaluated to identify the most effective NTO configuration across a range of fall-off values, based on the criteria outlined in Table 4.3. These criteria were centered on target metrics including conformity indices, maximum dose, and target mean doses. Early in the analysis, fall-off values of 0.05 and 0.1 mm^{-1} were identified as providing no significant gradient-enhancing benefits compared to higher fall-off values for both NTO configurations. This finding directed the analysis toward evaluating the efficacy of higher fall-off values in achieving the specified criteria.

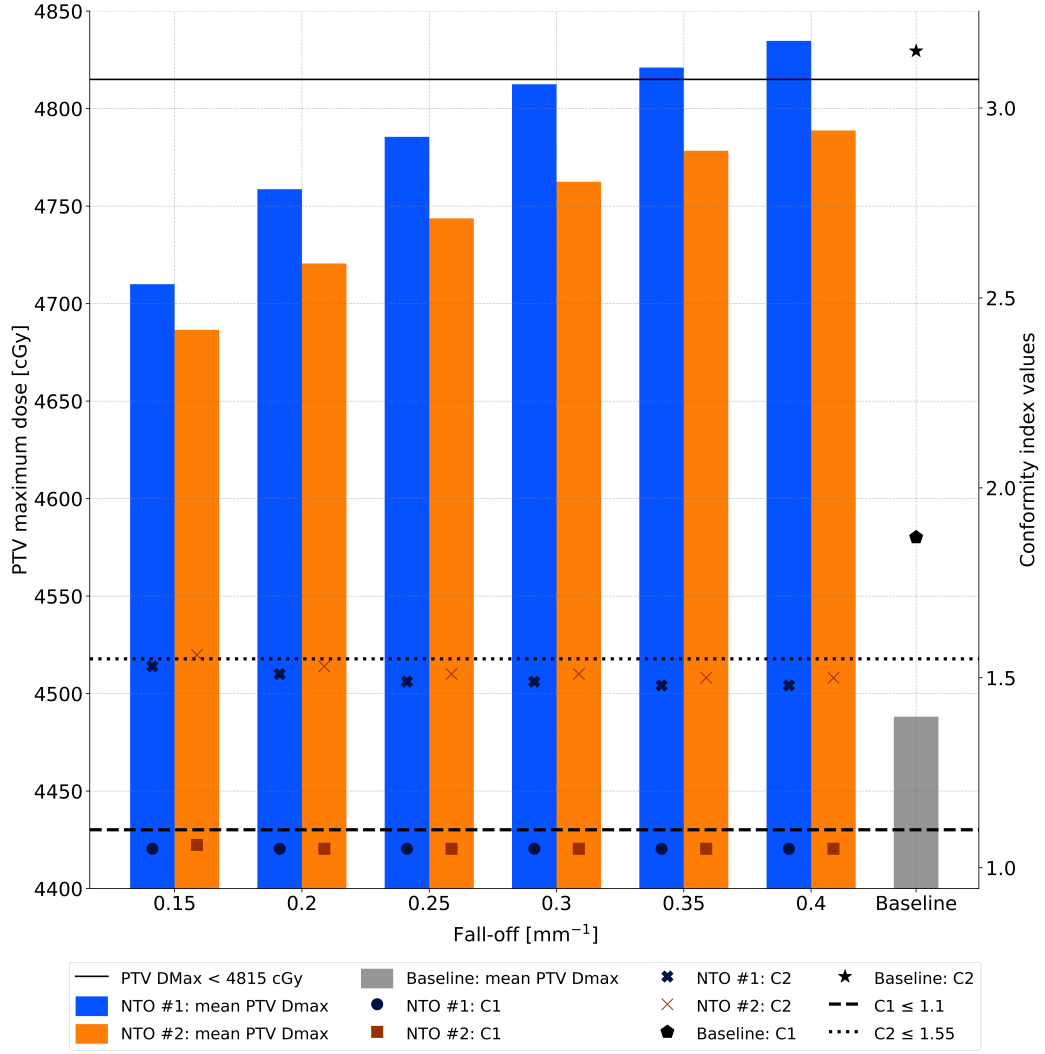

Figure 4.3: Comparison of planning target volume (PTV) maximum dose and conformity indices (C1 and C2) across various fall-off rates using Normal Tissue Objective (NTO) configurations. Bars represent the mean PTV maximum dose for NTO #1 and NTO #2. Scatter points indicate conformity indices, with circles and squares representing C1 and Xs representing C2. Clinical goals are denoted by solid and dashed lines: PTV maximum dose (< 4815 cGy), C1 (≤ 1.1), and C2 (≤ 1.55). The baseline results are shown for reference. This figure illustrates the trade-offs between dose conformity and target dose control for different fall-off rates across the two NTO configurations.

The comparison between the two NTO configurations across various fall-off values for the PTV Dmax and conformity indices are shown in Figure 4.3. Both configurations achieved excellent dose conformity, with C1 across all fall-offs. However,

NTO #1 maintained C2 over a broader fall-off range (0.15–0.4 mm^{-1}), whereas NTO #2 achieved this at higher fall-off values (0.2 – 0.4 mm^{-1}). Additionally, NTO #2 generally exhibited higher C2 values compared to NTO #1, which correlated with lower PTV Dmax values, particularly over the fall-off range of 0.1 – 0.4 mm^{-1}. This highlights a trade-off between target conformity and maximum dose control, where NTO #1 achieved lower C2 conformity with higher PTV Dmax values, and NTO #2 demonstrated superior control of PTV Dmax with higher conformity values, minimizing the risk of hot spots and ensuring safer dose delivery.

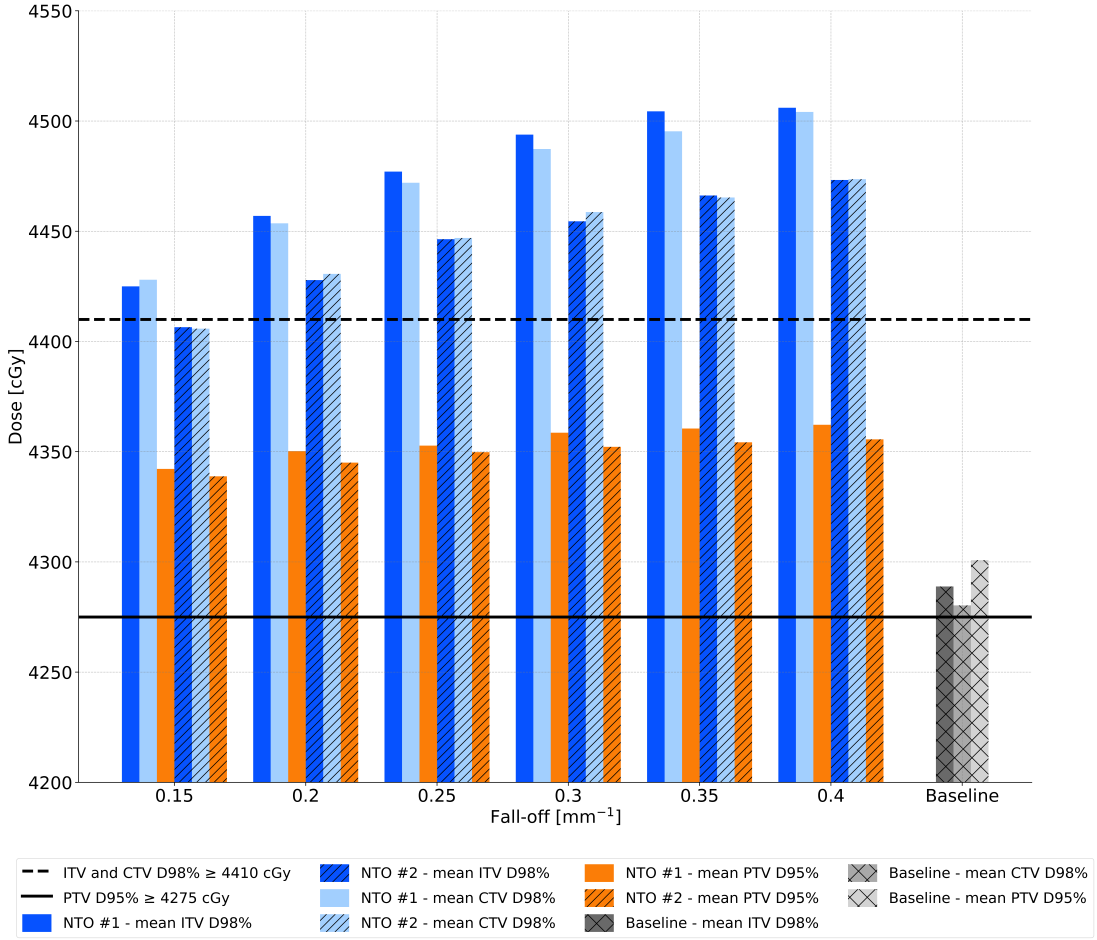

Figure 4.4: Mean doses to target across various fall-off rates using Normal Tissue Objective (NTO) configurations. Target structures include the Internal Target Volume (ITV), Clinical Target Volume (CTV), and Planning Target Volume (PTV). The dashed horizontal line indicates the clinical goal for ITV and CTV (D98% $\geq$ 4410 cGy), while the solid horizontal line represents the clinical goal for PTV (D95% $\geq$ 4275 cGy). Baseline results, included for comparison, highlight the capabilities of NTO configurations.

Figure 4.4 illustrates the mean doses for target structures using the two NTO configurations. The PTV mean dose was consistently achieved across all tested fall-off values for both configurations. However, mean doses for the ITV and CTV were achieved more efficiently with NTO #1, which consistently met the $\geq$ 4410 cGy threshold at lower fall-off values, specifically at or above 0.15 mm^{-1}. In contrast, NTO #2 required higher fall-off values, starting at 0.2 mm^{-1} or greater, to meet the same mean dose criteria for these targets. Additionally, NTO #1 generally exhibited higher mean dose values across the target volumes compared to NTO #2. This difference can be attributed to the parameter settings of NTO #1, which are designed to allow higher doses within the target structures, resulting in hotter treatment plans compared to NTO #2, which restricts higher doses more conservatively with its lower start dose.

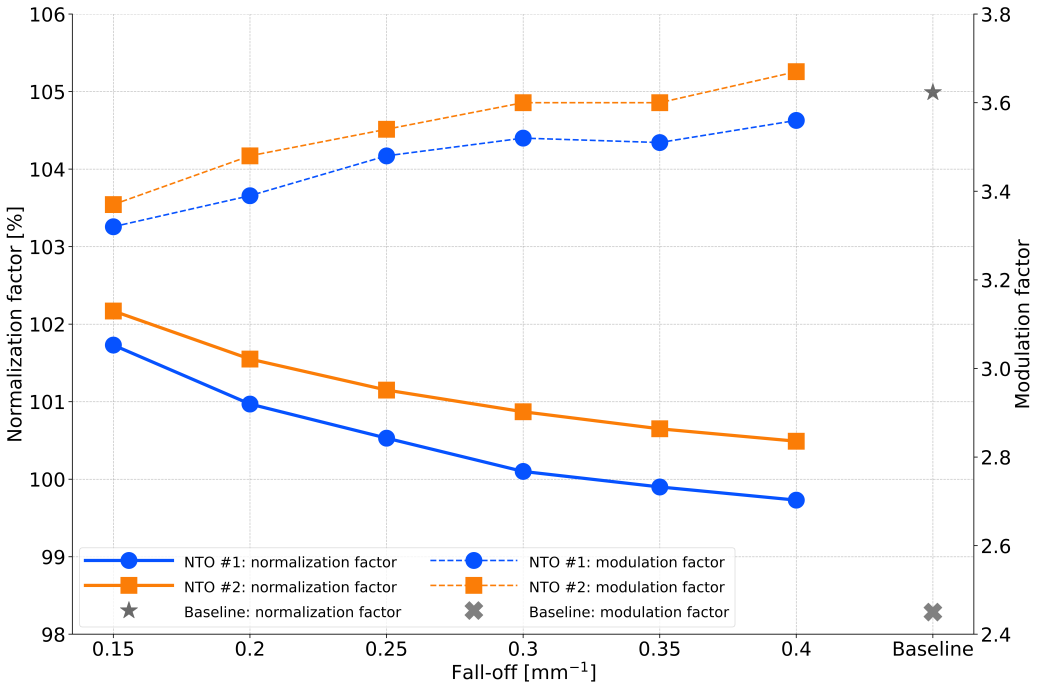

Figure 4.5: Normalization and modulation factors across various fall-off rates using Normal Tissue Objective (NTO) configurations. Mean normalization factor (%) for NTO #1 and #2 across varying fall-off rates are represented by solid lines. Mean modulation factor for NTO #1 and #2 are represented by dotted lines. Baseline results are shown as a single scatter point.

To further determine the optimal NTO configuration, plan normalization and modulation factors were analyzed, shown in Figure 4.5. As the fall-off increased,

normalization factors for both NTO configurations exhibited a decreasing trend, indicating that less dose scaling was required at higher fall-off values. This reduction plateaued around the fall-off of 0.3 mm^{-1} and beyond. In contrast, modulation factors followed an inverse trend, increasing as the fall-off value increased. This suggests that while higher fall-off reduces the need for additional dose scaling, they also introduce greater modulation complexity. NTO #1, with its higher start dose, consistently demonstrated lower normalization values compared to NTO #2, implying a more localized and hotter dose distribution that requires less overall dose scaling to achieve adequate target dose coverage. Although NTO #1 also showed lower modulation factors compared to NTO #2, the differences between the two configurations were not significant, suggesting comparable dose-shaping efficiency across both settings.

NTO #1 with a fall-off of 0.2 mm^{-1} was selected as the optimal configuration as it provided a balanced approach to achieving conformity, target doses (ITV, CTV and PTV), and PTV Dmax. At 0.15 mm^{-1}, C2 approached the conformity threshold (≤ 1.55), indicating a potential risk of insufficient dose shaping to the target, while at 0.3 mm^{-1}, the PTV Dmax exceeded safe limits, increasing the risk of potential hot spots. The fall-ff value of 0.2 mm^{-1} also ensured robust ITV and CTV dose (≥ 4410 cGy) while staying within the PTV Dmax limits. Additionally, this setting showed reasonable normalization requirements while minimizing increases in modulation, ensuring efficient dose distribution with minimal strain needed to achieve acceptable dose gradients.

4.3.2 Concentric Ring Structures (CRS) evaluations

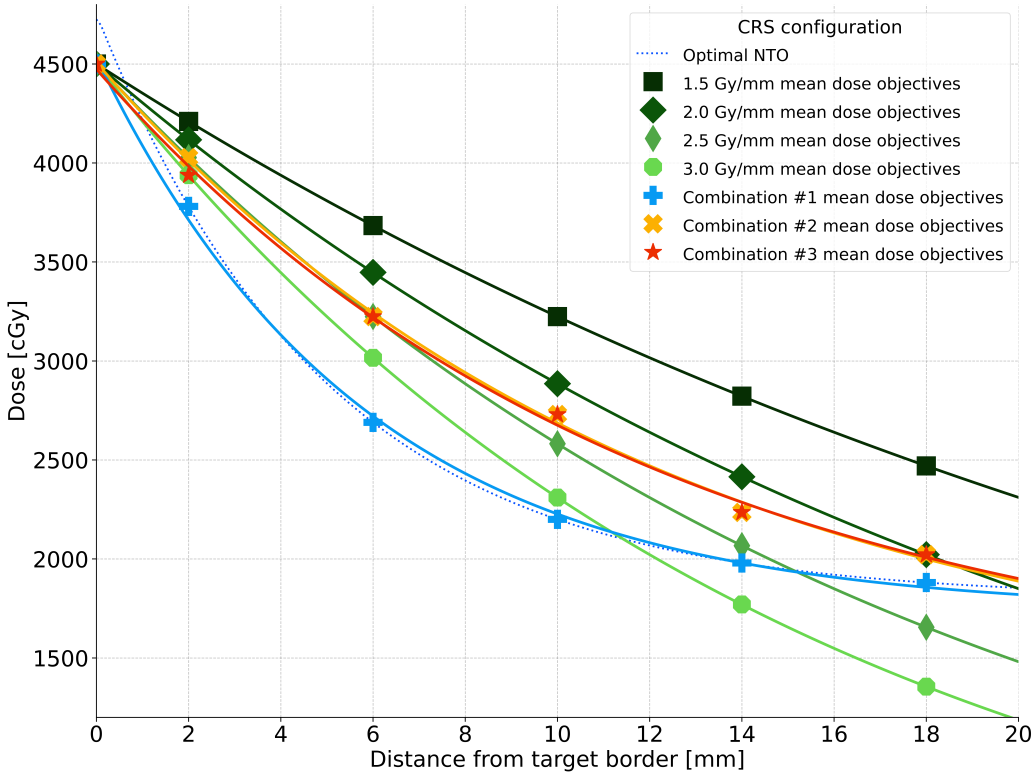

Figure 4.6: Dose profiles for various concentric ring structure (CRS) configurations. Each line represents the mean dose objective applied to each ring/distance from target border using different fall-off rates and combination strategies. The dotted line illustrates the dose profile obtained from NTO #1 to create Combination #1.

The performance of CRS using single predefined fall-offs was evaluated, revealing that while no single fall-off value achieved optimal results across all evaluation criteria, those in the 2.0 to 3.0 Gy/mm range met at least one of the criteria. Notably, fall-offs of 0.5 and 1.0 Gy/mm did not exhibit dose gradient-enhancing effects, performing comparably to baseline plans without gradient enhancing techniques. Given that no single fall-off value satisfied all evaluation criteria, combinations of specific fall-off values were used to create optimal CRS configurations, aiming to enhance conformity while mitigating hotspots within the target. Combination #1, Combination #2, and Combination #3 were designed to refine dose distribution to achieve the criteria. Their fall-off dose profiles with their corresponding mean dose objectives can be visualized in Figure 4.6, where these combinations exhibit more of an exponential

decay compared to the single fall-off dose profiles. All combinations exhibit steeper initial dose gradients near the target border compared to single fall-off values. Combination #1 has the steepest initial gradient, while Combinations #2 and #3 vary in their first ring settings. Specifically, Combination #3 achieves a steeper initial dose gradient than Combination #2, enhancing target dose delivery.

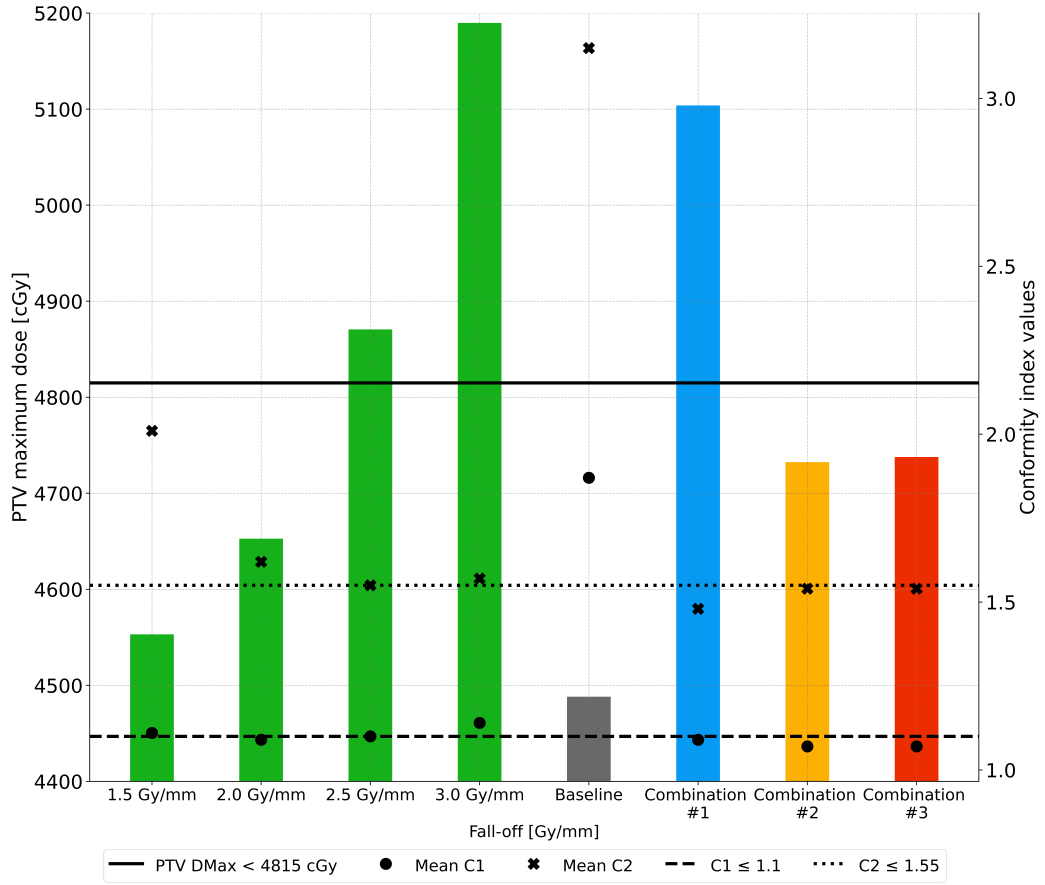

Figure 4.7: Planning target volume (PTV) maximum dose and conformity indices across various fall-off rates and combinations using concentric ring structures (CRS). Bars represent the mean PTV maximum dose across CRS configurations. Scatter points indicate conformity indices, with circles representing C1 and Xs representing C2. Clinical goals are denoted by solid and dashed lines: PTV maximum dose (< 4815 cGy), C1 (≤ 1.1), and C2 (≤ 1.55). The baseline results are shown for reference.

Figure 4.7 illustrates the PTV Dmax values and conformity indices across the CRS configurations. C1 was best achieved with fall-off values between 2.0 and 2.5G y/mm, while C2 performed optimally at 2.5 Gy/mm. However, achieving higher conformity was associated with increased PTV Dmax values, fall-off values below 2.5

Gy/mm stayed below the safe limit threshold. This highlights a trade-off between tighter conformity and limiting maximum dose. Configurations that reach optimal conformity, demonstrated by 3.0 Gy/mm and in Combination #1, resulted in elevated PTV Dmax values. These specific settings were shown to generate steeper initial dose gradients, leading to increased doses to the target and consequently yielding significantly high PTV Dmax values. Conversely, lower fall-off values (1.5 Gy/mm and 2.0 Gy/mm) maintained acceptable PTV Dmax but did not fully satisfy conformity criteria. However, Combination #2 and Combination #3 balanced these trade-offs by utilizing an initial fall-off that was less aggressive than that in Combination #1 but steep enough to improve conformity while maintaining PTV Dmax control.

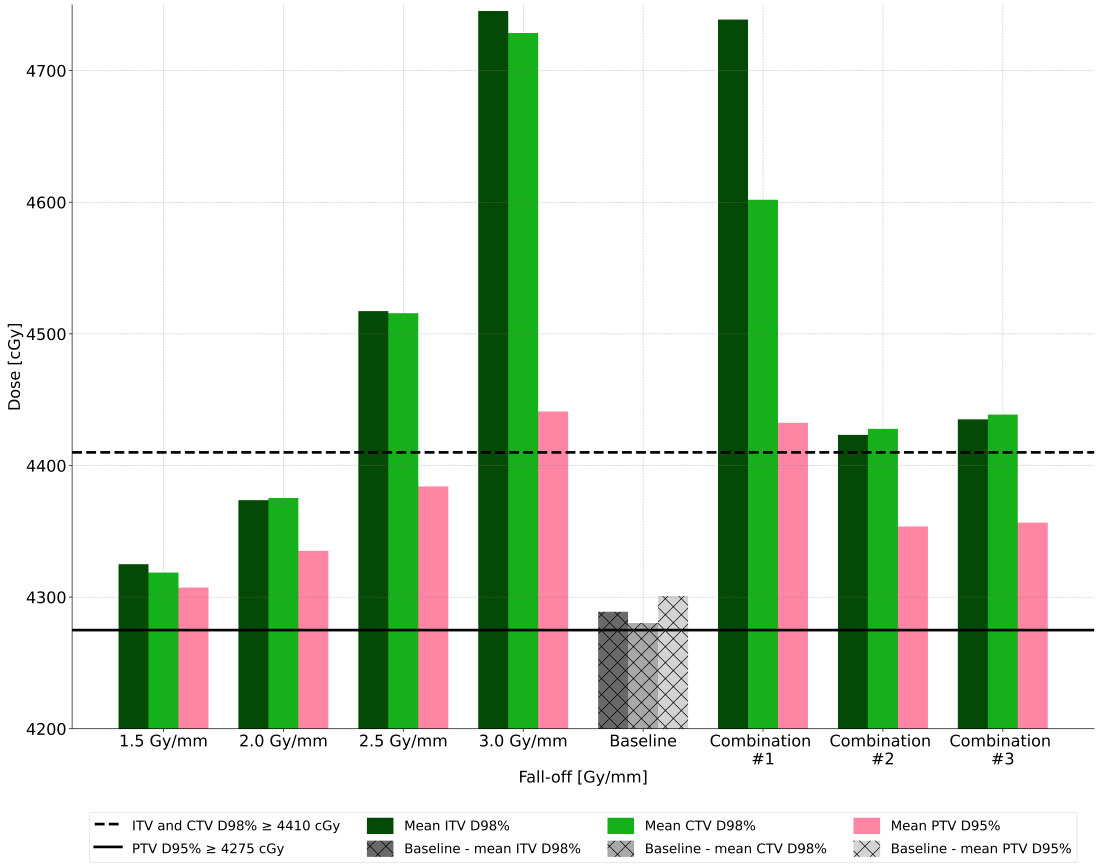

Figure 4.8: Mean dose coverage across various fall-off rates and combinations using concentric ring structures (CRS). Target structures include the Internal Target Volume (ITV), Clinical Target Volume (CTV), and Planning Target Volume (PTV). The dashed horizontal line indicates the clinical goal for ITV and CTV (D98% $\geq$ 4410 cGy), while the solid horizontal line represents the clinical goal for PTV (D95% $\geq$ 4275 cGy). Baseline results highlight the capabilities of CRS.

Figure 4.8 displays similar trends, with steeper fall-offs correlating with increased dose delivery to the target structures. Specifically, achieving the ITV and CTV mean doses required fall-off values of 2.5 Gy/mm or greater, as evidenced by higher doses in these configurations. However, the highest fall-off value of 3.0 Gy/mm resulted in excessive ITV and CTV doses, demonstrating the importance of balanced fall-off selection. Combinations #2 and #3 provided more controlled dose distributions, effectively maintaining ITV and CTV mean doses while preventing excessive dose escalation. Across all fall-off values and combinations, the PTV mean dose was consistently met.

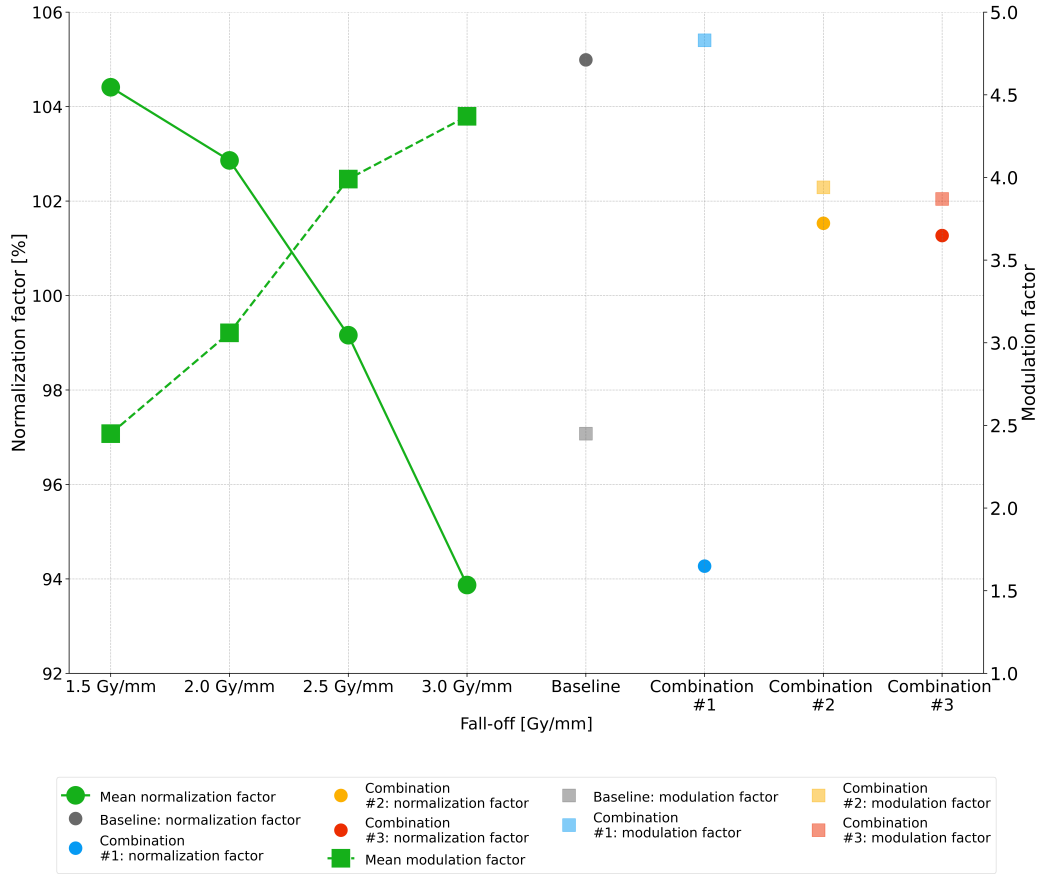

Figure 4.9: Normalization and modulation factors across various fall-off rates and combinations using concentric ring structures (CRS). Mean normalization factor (%) for single fall-off values are represented by the solid line with circle markers. Mean modulation factor for single fall-off values are represented by the dotted line with square markers. CRS using combinational fall-off values are depicted with circle markers representing normalization factor values, and square markers used to indicate modulation factors. Baseline normalization and modulation factors are shown as a grey circle and square, respectively.

Figure 4.9 demonstrates a trend where normalization factors decrease and modulation factors increase with greater fall-off values, similar to observations with increasing NTO fall-off values. This trend is evident in both individual fall-off values and combinational CRS configurations. The decline in normalization is particularly pronounced beyond 2.5 Gy/mm, where values drop below 94%. Conversely, modulation factors increased with higher fall-off values, reflecting greater intensity modulation complexity to achieve these steeper gradients. As expected, Combination #1 exhibited the highest modulation factor due to its steep initial gradient, as steeper fall-offs enhance dose conformity but require more complex intensity modulation while reducing the need for dose scaling to achieve target coverage with its high doses within target structures. In contrast, Combination #2 and Combination #3, which had less steep dose gradients than Combination #1, demonstrated greater normalization factors, indicating a higher degree of dose scaling was necessary to maintain target dose coverage while requiring less modulation to achieve their dose distributions.

The evaluation of combinational CRS configurations demonstrated varying degrees of success in achieving dose conformity, target mean doses, and PTV maximum dose control, as summarized in Table 4.4. Combination #1 excelled in ITV and CTV dose coverage, with 100% of cases achieving ITV D98% $\geq$ 4410 cGy and CTV D98% $\geq$ 4410 cGy. However, this resulted in excessive doses to these structures, leading to a high PTV Dmax (5103.85 $\pm$ 281.39 cGy), with no cases meeting the $<$ 4815 cGy threshold. The conformity was moderate, with C1 achieved in 87% of cases and C2 in 73%, indicating reasonable but suboptimal conformity.

Table 4.4: Comparison of combinational concentric ring structure configurations performance. This table presents a comparative analysis of three combinational CRS configurations.

Evaluation Criteria	Combination #1		Combination #2		Combination #3	
	Mean $\pm$ SD	Plans Achieved	Mean $\pm$ SD	Plans Achieved	Mean $\pm$ SD	Plans Achieved
C1 $\leq$ 1.1	1.09 $\pm$ 0.02	87%	1.07 $\pm$ 0.02	93%	1.07 $\pm$ 0.02	100%
C2 $\leq$ 1.55	1.48 $\pm$ 0.06	73%	1.54 $\pm$ 0.05	60%	1.54 $\pm$ 0.06	60%
PTV D_{max} $<$ 4815 cGy	5103.85 $\pm$ 281.39 cGy	0%	4732.41 $\pm$ 59.06 cGy	87%	4737.77 $\pm$ 43.09 cGy	93%
PTV $D_{95\%}$ $\geq$ 4275 cGy	4432.40 $\pm$ 30.67 cGy	100%	4353.67 $\pm$ 14.58 cGy	100%	4356.53 $\pm$ 14.40 cGy	100%
ITV $D_{98\%}$ $\geq$ 4410 cGy	4738.75 $\pm$ 92.77 cGy	100%	4423.24 $\pm$ 32.90 cGy	67%	4453.60 $\pm$ 36.65 cGy	93%
CTV $D_{98\%}$ $\geq$ 4410 cGy	4601.90 $\pm$ 565.06 cGy	100%	4427.79 $\pm$ 32.76 cGy	67%	4456.94 $\pm$ 31.40 cGy	93%

Combination #2 offered a more balanced approach, with 93% of cases achieving

C1 conformity while maintaining acceptable PTV Dmax values (4732.41 ± 59.06 cGy), and 87% of cases meeting the PTV Dmax threshold. However, C2 conformity was achieved in only 60% of cases, and ITV and CTV dose coverage was reduced, with 67% of cases meeting the D98% threshold for both the ITV and CTV. These results indicate that Combination #2 was associated with improved PTV dose control, accompanied by slight reductions in ITV and CTV dose coverage.

Combination #3 was the most aggressive in achieving C1, with 100% of cases meeting its criteria, while also achieving high PTV Dmax control (4737.77 ± 43.09 cGy), with 93% of cases staying below the threshold. However,similar to Combination #2, C2 conformity remained at 60%, indicating challenges in meeting both C1 and C2 simultaneously. Target dose coverage was improved over Combination #2, with 93% of cases achieving ITV and CTV D98% values, demonstrating a better dose distribution while avoiding the excessive dose escalation seen in Combination #1. Overall, Combination #3 provided the best balance among conformity, ITV and CTV dose coverage, and PTV Dmax control, while achieving a moderate normalization factor and avoiding excessive modulation, making it the optimal configuration for this study.

4.3.3 Evaluation of NTO and CRS

Table 4.5 shows the comparison between NTO #1 and CRS Combination #3, which were identified to be the most optimal in this study. Both configurations successfully met the evaluation criteria in terms of conformity, target dose coverage and OAR sparing, demonstrating their effectiveness in optimizing the dose gradient. However, when comparing these two dose gradient functions, statistically significant differences were observed, highlighting their distinct approaches optimizing the dose gradient.

Table 4.5: Comparison of optimal normal tissue objective configuration and optimal concentric ring structure configuration performance. A comprehensive comparison of planning evaluation results for optimal normal tissue objective (NTO) configuration and optimal concentric ring structure (CRS) configuration.

Evaluation Parameters		**Optimal NTO Function: NTO #1**	**Optimal CRS Function: Combination #3**	**P-value (Wilcoxon Signed Rank Test) NTO vs. CRS**
		mean ± standard deviation		NTO vs CRS
		Target		
Conformity Index #1	≤ 1.1	1.05 ± 0.01	1.07 ± 0.02	**<0.05**
Conformity Index #2	≤ 1.55	1.51 ± 0.06	1.54 ± 0.06	**<0.05**
PTV	Dmax <4815 cGy	4758.67 ± 30.90 cGy	4737.77 ± 43.09 cGy	**<0.05**
	D95% ≥ 4275 cGy	4350.26 ± 10.20 cGy	4356.53 ± 14.40 cGy	**<0.05**
CTV	D98% ≥ 4410 cGy	4438.68 ± 26.94 cGy	4456.94 ± 31.40 cGy	**<0.05**
ITV	D98% ≥ 4410cGy	4435.02 ± 28.22 cGy	4453.60 ± 36.65 cGy	**<0.05**
		Organs at Risk		
Bladder	V40Gy <60%	29.79 ± 9.67 %	29.96 ± 9.87 %	0.68
	V30Gy <80%	46.63 ± 10.34 %	46.20 ± 10.50 %	0.45
Bowel	V40Gy <300 cm^3	79.29 ± 56.98 cm^3	84.71 ± 60.07 cm^3	**<0.05**
	V30Gy <650 cm^3	172.66 ± 107.53 cm^3	191.44 ± 111.10 cm^3	**<0.05**
Rectum	V40Gy <75%	40.21 ± 14.20 %	40.78 ± 14.12 %	0.23
	V30Gy <95%	59.67 ± 12.59 %	59.97 ± 13.11 %	0.76
Sigmoid	V40Gy <80%	33.69 ± 23.32 %	35.23 ± 23.70 %	**<0.05**
		Other		
Normalization Factor		100.97 ± 0.72 %	101.27 ± 0.70 %	0.055
Modulation Factor		3.48 ± 0.31	3.87 ± 0.48	**<0.05**

NTO demonstrated better dose conformity, with a statistically significantly lower C1 value (1.05 ± 0.01) compared to CRS (1.07 ± 0.02) and a similarly lower C2 value (1.51 ± 0.06 vs. 1.54 ± 0.06). However, PTV Dmax values for CRS (4737.77 ± 43.09 cGy) and NTO (4758.67 ± 30.90 cGy), overlapped within one standard deviation, indicating no clear advantage in limiting maximum dose. These results highlight the trade-off between potentially improved PTV Dmax with CRS and achieving tighter dose conformity with NTO. CRS demonstrated slightly higher ITV and CTV D98% coverage, achieving 4453.60 ± 36.65 cGy (ITV) and 4456.94 ± 31.40 cGy (CTV) compared to 4435.02 ± 28.22 cGy (ITV) and 4438.68 ± 26.94 cGy (CTV) for NTO. While the differences were statistically significant ($p < 0.05$), the magnitude of the difference was small, suggesting only a marginal improvement in target doses with CRS. Additionally, PTV D95% was slightly higher with CRS (4356.53 ± 14.40 cGy) compared to NTO (4350.26 ± 10.20 cGy), with statistical significance ($p < 0.05$).

In regard to OAR dose-volume objectives, there are both similarities and key differences in dose distribution between NTO and CRS. The two configurations demonstrated comparable performance in sparing the bladder and rectum, with no statistically significant differences observed for bladder V40Gy (p = 0.68) and V30Gy (p = 0.45), or rectum V40Gy (p = 0.23) and V30Gy (p = 0.76). However, significant differences were noted for bowel sparing, where CRS resulted in higher doses. Specifically, bowel V40Gy was higher for CRS (84.71 ± 60.07 cm^3) compared to NTO (79.29 ± 56.98 cm^3), and V30Gy was also higher for CRS (191.44 ± 111.10 cm^3) than NTO (172.66 ± 107.53 cm^3) with both metrics showing statistical significance ($p < 0.05$). Similarly, sigmoid sparing showed a slight but statistically significant difference, with CRS delivering a higher dose (35.23 ± 23.70 cm^3) compared to NTO (33.69 ± 23.32 cm^3). These results suggest that while CRS is effective in delivering dose to the target structures, it may result in higher doses to the bowel and sigmoid in certain cases, indicating that NTO may be more advantageous for sparing organs at risk, especially the bowel.

Normalization factors were comparable between the two configurations (p = 0.055), with CRS having a slightly higher value (101.27 ± 0.70%) compared to NTO (100.97 ± 0.72%). Modulation factors, however, showed a statistically significant difference, with CRS exhibiting a wider range and a higher average modulation factor (3.87 ± 0.48) compared to NTO (3.48 ± 0.31). This indicates that CRS configurations involve greater complexity and may require longer treatment delivery times to achieve the desired dose distribution compared to NTO configurations.

4.4 Discussion

The objective of this study was to evaluate the effectiveness of two dose gradient optimization techniques, Normal Tissue Objective (NTO) and Concentric Ring Structures (CRS), in controlling and optimizing dose gradients outside the target to enhance OAR sparing in gynecological radiotherapy treatment planning. By systematically evaluating various parameter combinations, this study identified the most optimal settings for each method, balancing key evaluation criteria: target conformity, target dose coverage, and OAR sparing. The optimal NTO configuration within this study, was found to be NTO #1, while the optimal CRS configuration was Combination

#3. Both methods, were successful in meeting the evaluation criteria, demonstrating their ability to provide effective dose management in gynecological radiotherapy plans. This study aims to highlight the unique strengths and limitations of each method, offering insight into their applicability and effectiveness in different clinical scenarios.

4.4.1 Performance in target dose and PTV Dmax

CRS exhibited slightly improved D98% coverage for ITV and CTV, as well as enhanced PTV D95% compared to NTO, with statistical significance ($p < 0.05$) shown in Table 4.5. However, the magnitude of these differences was minimal (21.9 cGy), suggesting only a marginal enhancement in target dose coverage by CRS. Despite this, CRS can be strategically employed to ensure adequate dose delivery within the target by leveraging its precise control over the dose distribution. Its flexibility in adjusting each ring's dose objectives and priorities facilitates highly customized treatment plans, tailored specifically to meet the unique dose requirements of the target.

This was especially evident in the development of the optimal CRS combination, where the first ring of Combination #2 was adjusted to create a steeper dose gradient, directing more dose into the target area resulting in Combination #3 to achieve ITV and CTV mean doses across more patient plans. While this meticulous manipulation of dose objectives, priorities, and ring widths is time-consuming and demands considerable effort to finely balance their interplay, the precision offered by CRS proves to be particularly valuable in scenarios that demand stringent control over target dose coverage and dose gradients.

4.4.2 Performance in OAR sparing and dose conformity

The NTO and CRS differ significantly in how they manage dose distribution, with their respective strengths in achieving specific criteria detailed in Table 4.5. NTO demonstrated improved performance in sparing OARs and greater dose conformity, as evidenced by statistically significant reductions in OAR volumes, particularly for the bowel and sigmoid ($p < 0.05$). This improved sparing is attributed to the continuous

penalty function employed by NTO, which enforces a smooth and consistent reduction in dose to normal tissues beyond the target border. This approach helps maintain a uniform dose gradient, crucial for high conformity as it allows the radiation dose to be tightly confined around the target, minimizing exposure to surrounding tissues.

In contrast, CRS's optimization process does not penalize dose based on the tissues and OARs inside each ring but instead focuses solely on achieving the specified mean dose objectives for each specific ring volume. This approach offers highly flexible dose shaping, which is particularly beneficial for addressing complex geometries. As shown in Figure 4.10A, it enabled CRS to achieve lower dose levels in the concave region of the target, effectively conforming to the intricate anatomical shape. However, this same capability resulted in higher doses around the lateral regions of the target, as illustrated in Figure 4.10B. Consequently, this method can lead to OAR volumes to receive unnecessary dose due to the uneven dose distributions within the rings where higher doses compensate for lower ones. Such variability can also compromise the conformity to the target, as evidenced by the statistically significant higher conformity indices ($p < 0.05$) found with CRS. Additionally, the need to modulate doses significantly to conform to complex shapes leads to a higher modulation factor, which is statistically significant ($p < 0.05$) for CRS. This indicates that while CRS can precisely adapt to complex tumour geometries, it requires more intricate and intensive planning, potentially increasing the challenge in managing dose delivery and sparing adjacent normal tissues effectively.

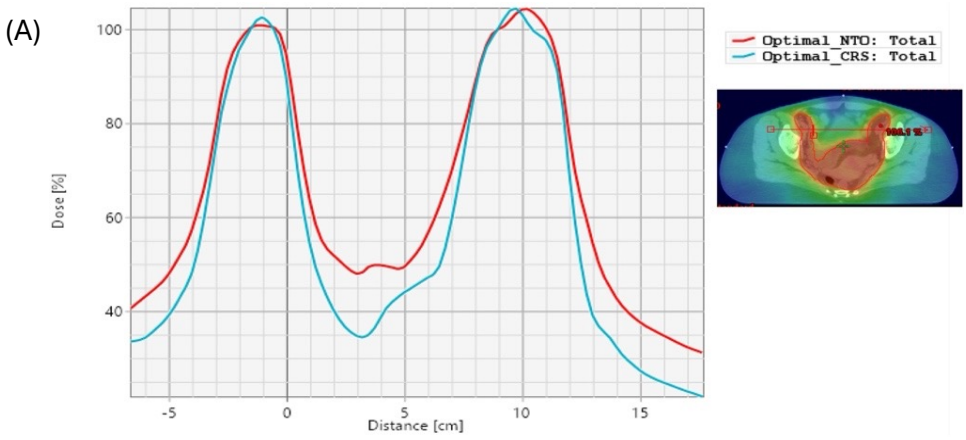

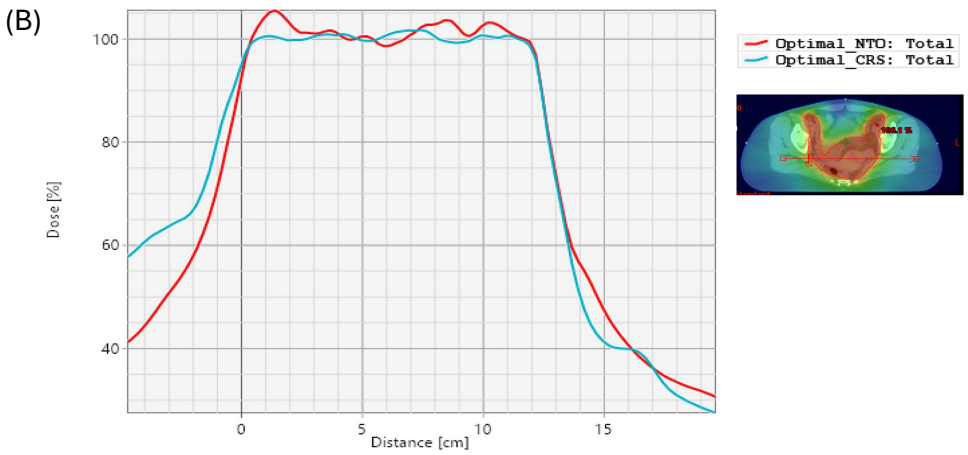

Figure 4.10: Dose gradient performance of the optimal Normal Tissue Objective (NTO) and concentric ring structure (CRS) configurations where (A) presents the dose line profile for the concave region of the target, while (B) shows the dose line profile for the lower lateral region of the target. The red line represents the optimal NTO configuration, and the blue line represents the optimal CRS configuration. This figure highlights the differences in dose gradients and distributions between the two configurations across the target.

Unlike CRS its dose variability within rings, NTO's global approach ensures a predictable and uniform dose gradient, making it particularly effective in reducing high-dose regions near critical structures. However, NTO's methodology also has limitations, particularly in cases involving multiple targets. The NTO evaluates the dose at each point in the normal tissue based on contributions from all target structures and applies penalties according to the highest dose at a given location.[78,79] While this approach ensures robust control of dose gradients, it may lead to suboptimal sparing of OARs if one target dominates the dose at certain points, potentially resulting in higher doses to nearby critical structures than expected. Despite this limitation, NTO's ability to consistently penalize dose to normal tissues remains a key strength, contributing to overall consistent dose reduction around the target emphasizing its robustness in sparing critical structures while maintaining conformity.

4.4.3 Functionality

The NTO and CRS are optimization tools that regulate the dose gradient between the target and surrounding normal tissues. While both aim to achieve steep dose fall-offs, they differ in how they apply and manage these gradients. Selecting the optimal combination of these parameters, however, can be tedious, as each parameter significantly influences the overall gradient. For the NTO, once the optimal parameter settings are identified, it can be easily implemented and consistently applied across treatment plans. Fortunately, several studies have determined optimal parameter combinations for specific tumour sites, providing a useful baseline for NTO application.[149–154] However, most studies were conducted using older versions of the Eclipse^{TM} TPS, resulting in variations in optimization processes across software versions due to differences in optimization components such as the cost function. Notably, differences in the cost function, which balances the optimization objectives alongside the NTO, are evident between versions 15.0 and 18.0.[78,79] Such variations can influence the way NTO parameters are applied and their overall effectiveness.

In contrast, CRS involves user-defined ring structures around the target, with specific dose objectives and priorities for each ring. The ability to customize these rings provides greater control over the dose gradients, enabling steep gradients near critical structures and more gradual gradients further from the target. However, the setup process for CRS is more labor-intensive, as users must define the ring widths, dose objectives, and priorities. This complexity introduces challenges, as the interaction between multiple rings and competing objectives may lead to conflicts. Additionally, the type of dose objective can influence CRS performance, as mean dose objectives may lead to inconsistent dose distributions within the rings, with higher dose regions emerging to compensate for lower dose areas. This effect was observed in Figure 4.10B, where CRS exhibited more pronounced dose gradient on one side of the target relative to the other. Studies employing CRS have explored the use of upper dose-volume objectives rather than mean dose objectives.[86,87,155] This approach aims to achieve stricter control over the dose uniformity by setting explicit constraints on maximum dose levels to a volume in the ring, potentially mitigating the variability and inconsistencies associated with mean dose objectives.

4.4.4 Clinical settings

The strengths of NTO and CRS make them suitable for different clinical scenarios. NTO excels in routine plans with single targets, where its consistent dose management and OAR sparing offer an efficient and reliable solution. Its ease of parameter configuration and ability to deliver consistent results across various treatment sites make it particularly valuable for streamlining the planning process. However, NTO's uniform application of dose penalties across all targets can limit its flexibility, making it less effective for complex geometries or cases involving multiple targets that require varying dose gradients.

In contrast, CRS offers distinct advantages due to its manual customization capabilities. This flexibility allows for precise control of dose gradients, enabling steep dose fall-offs near critical structures and more gradual gradients in less critical regions. Such adaptability shows to be beneficial in scenarios with challenging geometries, where the ability to tailor ring widths, dose objectives, and priorities can significantly enhance treatment efficacy. For complex plans involving multiple targets, the customization capabilities of CRS exceed those of NTO, which applies the same set of parameters to all target structures. CRS allows for individual optimization of dose gradients, adapting to the unique requirements of each target structure to enhance treatment efficacy. However, while CRS provides greater control, it also demands a greater investment of time and increased complexity, requiring careful meticulous adjustments of each ring.

4.4.5 Future work

While this study was limited by the time-intensive process of re-optimizing each plan using both NTO and CRS, it offers valuable insights into dose gradient optimization. As with many treatment planning studies, the sample size in this work was limited by the labor-intensive process of re-optimizing each plan using both NTO and CRS. Although a larger cohort would enhance statistical power and generalizability, the detailed nature of the re-optimization process provides meaningful insights that can inform future planning strategies. To build on these findings, future studies could explore leveraging the strengths of both CRS and NTO to further enhance treatment

planning. While this study highlights their individual advantages, the combination of CRS and NTO presents an opportunity for improved outcomes. Muthukumar et al. demonstrated the potential of such an approach, showing that integrating ring structures with NTO can enhance dose distribution, resulting in better target dose coverage and OAR sparing.[162] Additionally, incorporating optimized OAR and target objectives could enhance the effectiveness of NTO and CRS, achieving a balance between sparing critical structures and ensuring effective target coverage.[163–165] Furthermore, integrating patient-specific factors, such as anatomical variations in target and OAR size, into the dose gradient optimization processes of CRS and NTO could provide deeper insights into their capabilities, helping to refine their application and leverage their strengths in creating more personalized and effective treatment plans.[166–168]

4.5 Conclusion

The NTO and CRS were evaluated in their ability to optimize the dose gradient in gynecological radiotherapy treatment planning. By systematically analyzing various parameter combinations, the study identified optimal settings for each method. Both methods successfully met the evaluation criteria of target conformity, target dose coverage, and OAR sparing, underscoring their effectiveness in dose management. NTO demonstrated strong performance in achieving consistent OAR sparing and dose conformity ($p < 0.05$), with optimal parameters including a start dose of 105%, a distance from the target (DFT) of 0.05 cm, an end dose of 40%, a fall-off rate of 0.2 mm^{-1}, and a priority of 100. The optimal CRS configuration, utilizing five 4 mm-wide rings with progressively decreasing dose levels and various priority settings, achieved better target dose coverage and minimizing the maximum dose to the PTV ($p < 0.05$) compared to NTO. While NTO stands out for its ease of use and consistent application in routine plans, CRS offers unmatched flexibility for creating tailored dose gradients, making it particularly advantageous in complex or multi-target cases. Future work could explore the integration of NTO and CRS to leverage their combined strengths in enhancing dose gradients across various tumour sites and larger, more diverse patient populations, further optimizing radiotherapy planning and outcomes.

Chapter 5

Conclusions

The work presented in this thesis aimed to enhance clinical decision-making in radiotherapy planning for LDR prostate brachytherapy treatments and EBRT gynecological cancer treatments by evaluating and applying decision-support methodologies that improve treatment reliability, robustness, and overall quality of treatment plans. By addressing the challenge of delivering precise doses to the tumour while protecting healthy tissues and OARs, this work focused on tools and techniques to improve treatment robustness in the presence of dose variability and enhance dose distribution quality. These methodologies support clinical decision-making by providing planners with quantitative metrics and optimization strategies to assess plan reliability under uncertainty and guide planning choices in complex anatomical scenarios.

In the analysis of LDR prostate brachytherapy, an in-house dose calculation software BrachyVIC-3D was used to simulate seed positional uncertainties reflective of procedural variations encountered in the OR, in order to evaluate the statistical fluctuation and their impact on post-implant dose distributions. The BrachyVIC-3D software generated probabilities indicating the likelihood of achieving pre-implant constraints under the simulated uncertainty scenarios, in which optimal thresholds were determined using the area under the ROC curve and the Youden Index. The PTV V150% metric was used as a predictor, where its simulated probability was used to predict the achievement of the post-implant constraint, prostate D90%. For the PTV V150% probability, the optimal thresholds for predicting whether the prostate D90% constraint would be achieved were 68 $\pm$ 13% and 67 $\pm$ 24% for 2 mm and

3 mm shifts, respectively, derived from the analysis of 172 patient treatment plans. Additionally, global probabilities produced thresholds of 73 ± 12% for 2 mm shifts and 71 ± 6% for 3 mm shifts. These probability thresholds offer planners a metric assess plan robustness and make informed adjustments before finalizing the treatment plan for approval enhancing the quality of the plan too. These findings contribute not only to improving confidence in LDR brachytherapy treatment plans but also to having better understanding of the inherent uncertainties in the entire treatment process, particularly in cases where seed position variability is inevitable reducing the reliability of achieving clinical constraints. Future work in prostate LDR brachytherapy could benefit from further exploration of the outcome distribution in the current dataset, which included a greater proportion of plans that achieved the prostate D90% constraint compared to those that did not. A dataset with a greater number of patient plans, particularly one that includes a more balanced distribution between plans that achieve and do not achieve the prostate D90% constraint, may support the development of more accurate and generalizable thresholds by improving sensitivity to suboptimal plans. In addition, future analysis could investigate the spatial patterns of seed placement deviations to identify regions within the prostate that are more prone to positional uncertainty leading to under or over-dosage. This information could provide a rationale for non-planned supplemental seed (NPSS) placement and support planning strategies.

In the evaluation of EBRT for gynecological cancers, two dose gradient optimization techniques, normal tissue objective (NTO) and concentric ring structures (CRS), were assessed for their ability to shape the dose fall-off outside of the PTV and improve OAR sparing. Both methods met clinical dose-volume constraints but offer unique advantages depending on case complexity. The NTO demonstrated reliable performance and ease of implementation in routine clinical cases by applying a penalty function that produces a more uniform dose gradient around the target. However, its continuous approach is limited in its flexibility to refine its gradient, which can be important in anatomically complex scenarios. In contrast, CRS provides greater flexibility in dose shaping through manually defined ring structures with customizable objectives and parameters. While it is more adaptable, CRS requires increased planning effort and may introduce variability in the dose gradient around the target depending on objectives applied. These findings demonstrate how tailored optimization strategies can improve treatment goals and support decision-making in scenarios

where tumour proximity to OARs requires precise dose gradient control. By understanding the strengths and limitations of each method, planners can select the most appropriate optimization technique based on anatomical complexity, planning resources, and clinical priorities. Future work in gynecological EBRT treatment planning could focus on applying NTO and CRS across a wider range of clinical cases, beyond the 15 patients analyzed in this study. This could include a broader spectrum of tumour sites and anatomies involving multiple targets, such as concurrent treatment of the primary tumour and regional lymph nodes. Expanding both the number and diversity of cases would provide a more comprehensive understanding of how each optimization technique performs under varying anatomical complexities and clinical scenarios. Building on these insights, future studies could also explore the combined use of NTO and CRS, leveraging their complementary strengths to enhance dose gradient control. Furthermore, future studies could explore automation of CRS, including the generation of ring structures and the assignment of dose objectives and priority levels. Automating these components could streamline planning efforts where CRS are used. Beyond this, applying automated optimization models to iteratively refine ring parameters may allow for more efficient and adaptive gradient control tailored to patient anatomy.

Collectively, the findings presented in this thesis contribute to the ongoing advancement and refinement of radiotherapy treatment planning. Through the evaluation of robustness metrics and dose gradient optimization techniques, this work supports the strategies that allow planners to make more confident, data-driven planning decisions and improved dose distributions in complex anatomies. As radiotherapy continues to evolve, integrating these strategies into clinical workflows ensures greater consistency, efficiency and personalization in treatment delivery. By supporting more precise and reliable treatment plans, these advancements have the potential to improve outcomes, reduce side effects, and ultimately enhance the care experienced by cancer patients.

Appendix A

Additional Information

A.1 Comparison of NTO Optimization in Eclipse™ Versions

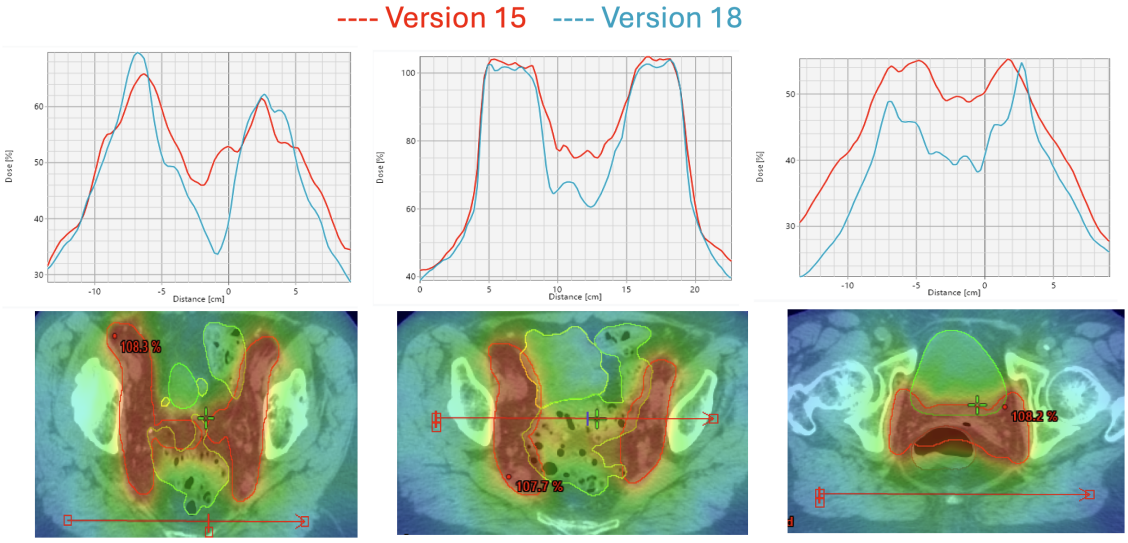

Figure A.1: Dose profiles comparing the Normal Tissue Objective (NTO) behavior between Eclipse™ Version 15.0 and Version 18.0 with Identical structures and NTO parameter settings

A.2 Comparison of CRS and NTO Optimization in Eclipse^{TM} Versions

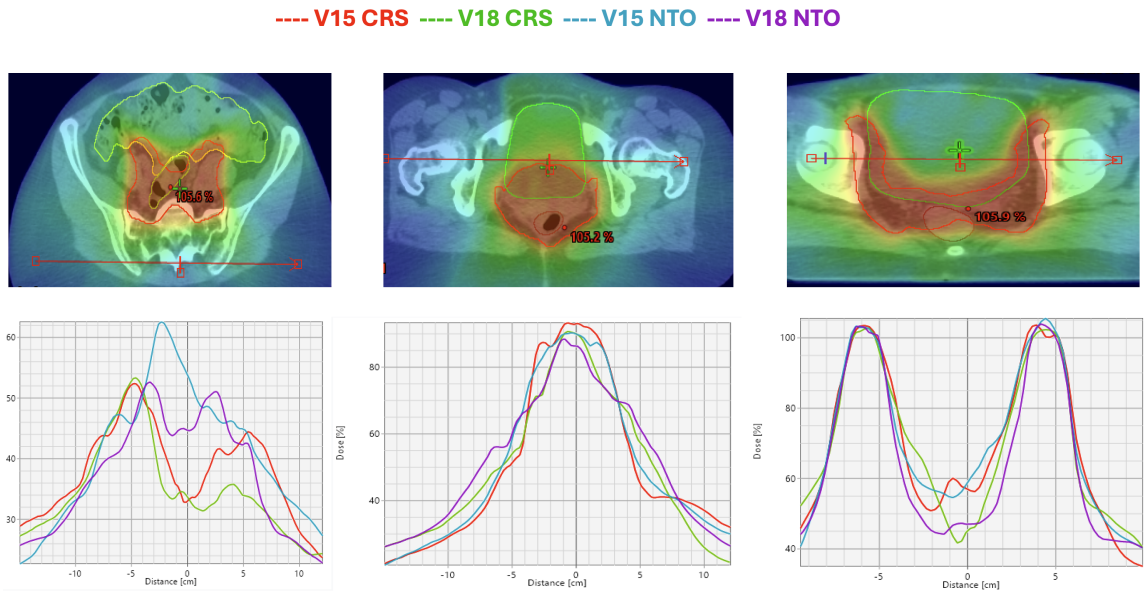

Figure A.2: Dose profiles comparing the Concentric Ring Structures (CRS) and Normal Tissue Objective (NTO) behavior between Eclipse^{TM} Version 15.0 and Version 18.0 with Identical structures and parameter settings

Bibliography

[1] Brenner Darren R., Gillis Jennifer, Demers Alain A., et al. Projected estimates of cancer in Canada in 2024 *CMAJ : Canadian Medical Association journal = journal de l'Association medicale canadienne.* 2024;196:E615-E623.

[2] Society. Canadian Cancer. Canadian cancer statistics 2024 2024.

[3] Society Canadian Cancer. Prostate cancer statistics. 2024.

[4] Marth Christian, Abreu Miguel Henriques, Andersen Klaus Kaae, et al. Real-life data on treatment and outcomes in advanced ovarian cancer: An observational, multinational cohort study (RESPONSE trial) *Cancer.* 2022;128:3080-3089.

[5] Curry Susan J., Krist Alex H., Owens Douglas K., et al. Screening for cervical cancer us preventive services task force recommendation statement *JAMA - Journal of the American Medical Association.* 2018;320:674-686.

[6] Khan Faiz M., Gibbons John P.. *The Physics of Radiation Therapy.* Philadelphia, PA: Lippincott Williams & Wilkins5th ed. 2014.

[7] Gunderson Leonard L., Tepper Joel E.. , eds.*Clinical Radiation Oncology.* Philadelphia, PA: Elsevier5th ed. 2021.

[8] Podgorsak Ervin B.. , ed.*Radiation Oncology Physics: A Handbook for Teachers and Students.* Vienna, Austria: International Atomic Energy Agency 2005.

[9] Ziessman Harvey A., O'Malley Janis P., Thrall James H.. Physics of nuclear medicine in *Nuclear Medicine* (Ziessman Harvey A., O'Malley Janis P., Thrall James H.. , eds.):20–33Philadelphia, PA: Mosby3rd ed. 2006.

[10] Mott James H., Daniel John M.. Interactions of electromagnetic radiation and subatomic particles with matter—part 2 *Clinical Oncology (Royal College of Radiologists).* 2021;33:533–538.

[11] Kim Yong Joo, Kim Chan Hyeong. Current status and future perspective of artificial intelligence in radiation therapy *Progress in Medical Physics.* 2020;31:124–134.

[12] Gianfaldoni Serena, Gianfaldoni Roberto, Wollina Uwe, Lotti Jacopo, Tchernev Georgi, Lotti Torello. An Overview on Radiotherapy: From Its History to Its Current Applications in Dermatology *Open Access Macedonian Journal of Medical Sciences.* 2017;5:521.

[13] Chargari Cyrus, Deutsch Eric, Blanchard Pierre, et al. Brachytherapy: An overview for clinicians *CA: A Cancer Journal for Clinicians.* 2019;69:386-401.

[14] Marcié S., Gerard J. P., Dejean C., et al. The inverse square law: A basic principle in brachytherapy *Cancer/Radiotherapie.* 2022;26:1075-1077.

[15] Skowronek Janusz. Current status of brachytherapy in cancer treatment – short overview *Journal of Contemporary Brachytherapy.* 2017;9:581-589.

[16] Stish Bradley J., Davis Brian J., Mynderse Lance A., McLaren Robert H., Deufel Christopher L., Choo Richard. Low dose rate prostate brachytherapy *Translational Andrology and Urology.* 2018;7:341-356.

[17] Zhang Hualin, Martin Douglas, Chiu-Tsao Sou Tung, Meigooni Ali, Thomadsen Bruce R.. A comprehensive dosimetric comparison between 131Cs and 125I brachytherapy sources for COMS eye plaque implant *Brachytherapy.* 2010;9:362-372.

[18] Chin Joseph, Rumble R. Bryan, Kollmeier Marisa, et al. Brachytherapy for patients with prostate cancer: American Society of Clinical Oncology/Cancer Care Ontario joint guideline update *Journal of Clinical Oncology.* 2017;35:1737-1745.

[19] Blasko John C., Grimm Peter D., Sylsvester John E., Cavanagh William. The role of external beam radiotherapy with I-125/Pd-103 brachytherapy for prostate carcinoma *Radiotherapy and Oncology.* 2000;57:273-278.

[20] Booher Jacquelyn, Domenig Peter, Goldman Benjamin, et al. Comparison of Three Groups of Patients Having Low Dose Rate Prostate Brachytherapy: Prostate-Specific Antigen Failure and Overall Survival *Cureus.* 2021;13:e18185.

[21] McParland Neil, Chng Nicholas, Keyes Mira. The dosimetric impact of supplementing pre-planned prostate implants with discretionary 125I seeds *Journal of Radiotherapy in Practice.* 2013;12:226-236.

[22] Cleveland Clinic . Prostate brachytherapy https://my.clevelandclinic.org/health/procedures/prostate-brachytherapy 2023. Published March 9, 2023. Accessed April 14, 2025.

[23] Nath Ravinder, Anderson Lowell L., Luxton Gary, Weaver Keith A., Williamson Jeffey F., Meigooni Ali S.. Dosimetry of interstitial brachytherapy sources: Recommendations of the AAPM Radiation Therapy Committee Task Group No. 43 *Medical Physics.* 1995;22:209-234.

[24] Metcalfe Peter, Kron Tomas, Hoban Peter, Cutajar Dean, Hardcastle Nicholas. *The Physics of Radiotherapy X-Rays and Electrons: 3rd Edition.* Medical Physics Publishing3rd ed. 2023.

[25] Söderström Svante, Eklöf Anders, Brahme Anders. Aspects on the optimal photon beam energy for radiation therapy *Acta Oncologica.* 1999;38:179-187.

[26] Elbashir Fawzia E.M., Ksouri Wassim, Habbani Farouk, El-Khayatt Ahmed M., Eisa Mohamed Hassan, Suliman Ibrahim I.. Analysis of Uncertainties in Clinical High-Energy Photon Beam Calibrations Using Absorbed Dose Standards *Applied Sciences 2022, Vol. 12, Page 3857.* 2022;12:3857.

[27] Videtic Gregory M., Vassil Andrew D., Woody Nathan M.. , eds.*Handbook of Treatment Planning in Radiation Oncology.* New York, NY: Springer Publishing Company 2020.

[28] Herman Tania De La, Schnell Erich, Young Julie, et al. Dosimetric comparison between IMRT delivery modes: Step-and-shoot, sliding window, and volumetric modulated arc therapy - For whole pelvis radiation therapy of intermediate-to-high risk prostate adenocarcinoma *Journal of Medical Physics.* 2013;38:165-172.

[29] Wolff Dirk, Stieler Florian, Welzel Grit, et al. Volumetric modulated arc therapy (VMAT) vs. serial tomotherapy, step-and-shoot IMRT and 3D-conformal RT for treatment of prostate cancer *Radiotherapy and Oncology.* 2009;93:226-233.

[30] Teoh May, Clark C. H., Wood K., Whitaker S., Nisbet A.. Volumetric modulated arc therapy: A review of current literature and clinical use in practice *British Journal of Radiology.* 2011;84:967-996.

[31] Petrović Borislava, Ivanov Olivera, Marjanović Milana, Ličina Jelena, Gencel Ivan, Golubovac Nemanja. The transition from conformal to advanced radiotherapy techniques in the treatment planning of gynecological cancer patients *Vojnosanitetski pregled.* 2022;79:951-957.

[32] Dewey Jane. Gynaecological cancers in *Radiotherapy Planning* (Hoskin Peter. , ed.):373–384Boca Raton, FL: CRC Press5th ed. 2023.

[33] Fukada Junichi, Shigematsu Naoyuki, Nakashima Jun, Ohashi Toshio, Kawaguchi Osamu, Oya Mototsugu. Predicting pubic arch interference in prostate brachytherapy on transrectal ultrasonography-computed tomography fusion images. *Journal of radiation research.* 2012;53:753-759.

[34] Solhjem Matthew C., Davis Brian J., Pisansky Thomas M., et al. Prostate volume measurement by transrectal ultrasound and computed tomography before and after permanent prostate brachytherapy *International Journal of Radiation Oncology Biology Physics.* 2004;60:767-776.

[35] Suetens Paul. *Fundamentals of Medical Imaging.* Cambridge, UK: Cambridge University Press2nd ed. 2009.

[36] Tyloch Janusz F., Wieczorek Andrzej Paweł. The standards of an ultrasound examination of the prostate gland. Part 2 *Journal of ultrasonography.* 2017;17:43-58.

[37] Singh Nidhi, Chérin Emmanuel, Roa Carlos Felipe, et al. Adaptation of a Clinical High-Frequency Transrectal Ultrasound System for Prostate Photoacoustic Imaging: Implementation and Pre-clinical Demonstration *Ultrasound in Medicine and Biology.* 2024;50:457-466.

[38] Hoskins Peter, Martin Kevin, Thrush Abigail. *Diagnostic Ultrasound: Physics and Equipment.* Cambridge, UK: Cambridge University Press2nd ed. 2010.

[39] Hoskins Peter. *Diagnostic Ultrasound: Physics and Equipment.* United Kingdom: Greenwich Medical Media 2003.

[40] Royal College of Emergency Medicine (RCEM) Learning . B-mode https://www.rcemlearning.org/modules/ultrasound-physics-and-basic-equipment-settings/lessons/types-of-ultrasound/topic/bmode/ 2025. Accessed January 8, 2025.

[41] Tatsugami Fuminari, Higaki Toru, Nakamura Yuko, Honda Yukiko, Awai Kazuo. Dual-energy CT: minimal essentials for radiologists *Japanese Journal of Radiology.* 2022;40:547-559.

[42] Michael Greg. X-ray computed tomography *Physics Education.* 2001;36:442.

[43] Nakamura Yuko, Higaki Toru, Kondo Shota, Kawashita Ikuo, Takahashi Isao, Awai Kazuo. An introduction to photon-counting detector CT (PCD CT) for radiologists *Japanese Journal of Radiology.* 2023;41:266-282.

[44] Kim M. S., Lim K. T., Kim G., Cho G.. A comparative study of scintillator combining methods for flat-panel X-ray image sensors *Nuclear Instruments and Methods in Physics Research Section A: Accelerators, Spectrometers, Detectors and Associated Equipment.* 2018;882:84-90.

[45] Jung Haijo. Basic Physical Principles and Clinical Applications of Computed Tomography *Progress in Medical Physic.* 2021;32:1-17.

[46] Bushberg Jerrold T., Seibert J. Anthony, Leidholdt Edwin M., Boone John M.. *The Essential Physics of Medical Imaging.* Philadelphia, PA: Wolters Kluwer Health3rd ed. 2011.

[47] Bushberg Jerrold T., Seibert J. Anthony, Leidholdt Edwin M. Jr., Boone John M.. *The Essential Physics of Medical Imaging.* Philadelphia, PA: Wolters Kluwer Health4th ed. 2020.

[48] Schofield R., King L., Tayal U., et al. Image reconstruction: Part 1 – understanding filtered back projection, noise and image acquisition *Journal of Cardiovascular Computed Tomography.* 2020;14:219-225.

[49] Shi Feng, Hu Weigang, Wu Jiaojiao, et al. Deep learning empowered volume delineation of whole-body organs-at-risk for accelerated radiotherapy *Nature Communications 2022 13:1.* 2022;13:1-13.

[50] Ye Xianghua, Guo Dazhou, Ge Jia, et al. Comprehensive and clinically accurate head and neck cancer organs-at-risk delineation on a multi-institutional study *Nature Communications.* 2022;13.

[51] Jones Douglas. ICRU Report 50—Prescribing, Recording and Reporting Photon Beam Therapy *Medical Physics.* 1994;21:833-834.

[52] (chair George Sgouros, Bolch Wesley E, Chiti Arturo, et al. ICRU REPORT 96, DOsImETRy-GUIDED RaDIOPhaRmaCEUTICal ThERaPy *Journal of the ICRU 2021.* 2021;21:1-212.

[53] Spadinger Ingrid. Prostate brachytherapy treatment planning procedure clinical procedure documentBC Cancer Agency 2015.

[54] Keyes Mira, Miller Stacy, Moravan Veronika, et al. Predictive Factors for Acute and Late Urinary Toxicity After Permanent Prostate Brachytherapy: Long-Term Outcome in 712 Consecutive Patients *International Journal of Radiation Oncology Biology Physics.* 2009;73:1023-1032.

[55] Tanimoto Ryuta, Bekku Kensuke, Kobayashi Yasuyuki, et al. Predictive factors for acute and late urinary toxicities after permanent prostate brachytherapy. *Journal of Clinical Oncology.* 2012;30:90-90.

[56] Moltzahn Felix, Pra Alan Dal, Furrer Marc, Thalmann George, Spahn Martin. Urethral strictures after radiation therapy for prostate cancer *Investigative and Clinical Urology.* 2016;57:309.

[57] Morita Masashi, Hiramatsu Aya, Nishimura Kota, et al. Radiation proctitis after iodine-125 low-dose-rate prostate brachytherapy utilizing SpaceOAR hydrogel *International Journal of Urology.* 2024;31:1001-1008.

[58] Verrijssen An Sofie, Opbroek Thirza, Bellezzo Murillo, et al. A systematic review comparing radiation toxicity after various endorectal techniques *Brachytherapy.* 2019;18:71-86.e5.

[59] Zwaans Bernadette M.M., Lamb Laura E., Bartolone Sarah, Nicolai Heinz E., Chancellor Michael B., Klaudia Stangel Wójcikiewicz. Cancer survivorship issues with radiation and hemorrhagic cystitis in gynecological malignancies *International Urology and Nephrology.* 2018;50:1745-1751.

[60] He Ling, Wang Zhenyu, Chen Jianhui, Chen Ling, Chen Peijuan, Cai Wenzhi. Analysis of Clinicopathological Factors Associated with Radiation-Induced Cystitis in Patients with Cervical Cancer *Journal of Healthcare Engineering.* 2022;2022:6216072.

[61] Fang Jing, Fang Jinmei, Wu Ailin, Zhao Yufei, Liu Yun. Clinical analysis of predisposing factors for radiation enteritis in patients with cervical cancer *European Journal of Gynaecological Oncology.* 2021;42:951-956.

[62] Loge L., Florescu C., Alves A., Menahem B.. Radiation enteritis: Diagnostic and therapeutic issues *Journal of Visceral Surgery.* 2020;157:475-485.

[63] Im Chan Muk, Cho Ick Joon, Yu Hyung Joo, et al. Clinical Outcome and Risk Factors of Chronic Radiation Proctitis Following Pelvic Radiation Therapy *Anticancer Research.* 2022;42:5951-5959.

[64] Rodriguez M.. Gyne adjuvant planning procedure technical reportBC Cancer-Victoria, British Columbia 2023.

[65] Rodriguez M.. Gyne EMBRACE planning procedure technical reportBC CancerVictoria, British Columbia 2023.

[66] Drzymala R. E., Mohan R., Brewster L., et al. Dose-volume histograms *International Journal of Radiation Oncology*Biology*Physics.* 1991;21:71-78.

[67] Pötter Richard, Tanderup Kari, Kirisits Christian, et al. The EMBRACE II study: The outcome and prospect of two decades of evolution within the GEC-ESTRO GYN working group and the EMBRACE studies *Clinical and Translational Radiation Oncology.* 2018;9:48-60.

[68] Cibula David, Raspollini Maria Rosaria, Planchamp François, et al. ESGO/ESTRO/ESP Guidelines for the management of patients with cervical cancer - Update 2023. *Virchows Archiv : an international journal of pathology.* 2023;482:935-966.

[69] Serban Monica, Kirisits Christian, Pötter Richard, et al. Isodose surface volumes in cervix cancer brachytherapy: Change of practice from standard (Point A) to individualized image guided adaptive (EMBRACE I) brachytherapy *Radiotherapy and Oncology.* 2018;129:567-574.

[70] European Society for Radiotherapy and Oncology (ESTRO) . *ESTRO Online Course on Image Guided Radiotherapy and Chemotherapy in Gynaecological Cancer: Focus on Cervical Cancer Course Book.* ESTROBrussels, Belgium 2020.

[71] Chargari Cyrus, Tanderup Kari, Planchamp François, et al. ESGO/ESTRO quality indicators for radiation therapy of cervical cancer *Radiotherapy and Oncology.* 2023;183.

[72] Tepper Joel E., Gunderson Leonard L.. Clinical Radiation Oncology *Clinical Radiation Oncology.* 2015:1-1648.

[73] Videtic Gregory M. M.. *Strategies for Radiation Therapy Treatment Planning.* New York, NY: Springer Publishing Company 2018.

[74] Mokhtar Maha, Attalla Ehab M, Deiab Nashaat A, Soltan Ahmed, Abou-Shady H, Amin Amr. Comparative dosimetry of forward and inverse treatment planning for Intensity-Modulated Radiotherapy of prostate cancer *IOSR Journal of Applied Physics (IOSR-JAP.* ;7:97-106.

[75] Mendes Ruheena, Lavrenkov Konstantin, Bedford James L., Henrys Anthony, Ashley Sue, Brada Michael. Comparison of forward planning with automated inverse planning for three-dimensional conformal radiotherapy of non-small cell lung cancer without IMRT *Radiotherapy and Oncology.* 2006;78:322-325.

[76] Varian Medical Systems . *VariSeed™ 9.0 Instructions for Use.* Varian Medical Systems, Inc.Palo Alto, CA 2020.

[77] Taylor A., Powell M. E.B.. Intensity-modulated radiotherapy - What is it? *Cancer Imaging.* 2004;4:68-73.

[78] Varian Medical Systems . *Eclipse Photon and Electron Algorithms 18.1 Reference Guide.* Varian Medical SystemsPalo Alto, CA 2022.

[79] Varian Medical Systems . *Eclipse Photon and Electron Algorithms 15.5 Reference Guide*. Varian Medical SystemsPalo Alto, CA 2018.

[80] Varian Medical Systems . *Eclipse Photon and Electron Algorithms Reference Guide*. Varian Medical SystemsPalo Alto, CA 2015.

[81] Murugan Perumal, Manickam Ravikumar, Rajamanickam Tamilarasan, et al. Evaluation of improvements in plan quality with Photon Optimizer v16.1 for single brain lesion SRS treatment *Reports of Practical Oncology and Radiotherapy.* 2023;28:801-808.

[82] Marcu Loredana., Allen B. J.., Bezak Eva.. *Biomedical physics in radiotherapy for cancer*. CSIRO Publishing 2024.

[83] Reynolds Tatsiana A., Jensen Andrew R., Bellairs Ellen E., Ozer Mustafa. Dose Gradient Index for Stereotactic Radiosurgery/Radiation Therapy *International Journal of Radiation Oncology Biology Physics.* 2020;106:604-611.

[84] Fuss Martin, Salter Bill J.. Intensity-modulated radiosurgery: Improving dose gradients and maximum dose using post inverse-optimization interactive dose shaping *Technology in Cancer Research and Treatment.* 2007;6:197-203.

[85] Kramer Bradley A., Wazer David E., Engler Mark J., Tsai Jen San, Ling Marilyn N.. Dosimetric comparison of stereotactic radiosurgery to intensity modulated radiotherapy *Radiation Oncology Investigations.* 1998;6:18-25.

[86] Cao Yangsen, Zhu Xiaofei, Ju Xiaoping, et al. Optimization of dose distributions of target volumes and organs at risk during stereotactic body radiation therapy for pancreatic cancer with dose-limiting auto-shells *Radiation Oncology.* 2018;13.

[87] Duan Yanhua, Gan Wutian, Wang Hao, et al. On the optimal number of dose-limiting shells in the SBRT auto-planning design for peripheral lung cancer *Journal of Applied Clinical Medical Physics.* 2020;21:134.

[88] Fan Y., Qiu G., Pan Q., Zhang F., Luan S.. A primary study on setting the limit ring in intensity-modulated radiation therapy treatment planning in lung cancer *International Journal of Radiation Research.* 2020;18:185-189.

[89] Varian Medical Systems . *VariSeed™ 9.0 Reference Guide.* Varian Medical Systems, Inc.Palo Alto, CA 2020.

[90] Saw Cheng B., Meigooni Ali S., Nath Ravinder. Review of AAPM Task Group No. 43 recommendations on interstitial brachytherapy sources dosimetry *Medical Dosimetry.* 1998;23:259-263.

[91] Ito Takaaki, Monzen Hajime, Kubo Kazuki, et al. Dose difference between anisotropic analytical algorithm (AAA) and Acuros XB (AXB) caused by target's air content for volumetric modulated arc therapy of head and neck cancer *Reports of Practical Oncology and Radiotherapy.* 2023;28:399.

[92] Yan Chenyu, Combine Anthony G., Bednarz Greg, et al. Clinical implementation and evaluation of the Acuros dose calculation algorithm *Journal of Applied Clinical Medical Physics.* 2017;18:195-209.

[93] Tajaldeen Abdulrahman, Ramachandran Prabhakar, Alghamdi S., Geso M.. On the use of AAA and AcurosXB algorithms for three different stereotactic ablative body radiotherapy (SABR) techniques: Volumetric modulated arc therapy (VMAT), intensity modulated radiation therapy (IMRT) and 3D conformal radiotherapy (3D-CRT) *Reports of Practical Oncology and Radiotherapy.* 2019;24:399-408.

[94] Chung Eugene, Stenmark Matthew H., Evans Cheryl, Narayana Vrinda, McLaughlin Patrick W.. Greater postimplant swelling in small-volume prostate glands: Implications for dosimetry, treatment planning, and operating room technique *International Journal of Radiation Oncology Biology Physics.* 2012;82:1944-1948.

[95] Taussky Daniel, Austen Lyn, Toi Ants, et al. Sequential evaluation of prostate edema after permanent seed prostate brachytherapy using CT-MRI fusion *International Journal of Radiation Oncology Biology Physics.* 2005;62:974-980.

[96] Liu Hong Wei, Malkoske Kyle, Sasaki David, et al. The dosimetric quality of brachytherapy implants in patients with small prostate volume depends on the experience of the brachytherapy team *Brachytherapy.* 2010;9:202-207.

[97] Gregory Kent J., Pattison John E., Bibbo Giovanni. Measurement uncertainty analysis of low-dose-rate prostate seed brachytherapy: post-implant dosimetry *Australasian Physical and Engineering Sciences in Medicine.* 2015;38:71-81.

[98] Han Misop, Chang Doyoung, Kim Chunwoo, et al. Geometric evaluation of systematic transrectal ultrasound guided prostate biopsy *Journal of Urology.* 2012;188:2404-2409.

[99] Brost Eric E., Stish Bradley J., Lee Christine U., Urban Matthew W., Deufel Christopher L.. Improving ultrasound-based brachytherapy needle conspicuity by applying an echogenic coating *Medical Physics.* 2023;50:1418-1427.

[100] Cui Sunan, Tseng Huan Hsin, Pakela Julia, Haken Randall K. Ten, Naqa Issam El. Introduction to machine and deep learning for medical physicists *Medical Physics.* 2020;47:e127-e147.

[101] Naqa Issam El, Das Shiva. The role of machine and deep learning in modern medical physics 2020.

[102] Preti Luigi M, Ardito Vittoria, Compagni Amelia, Petracca Francesco, Cappellaro Giulia. Implementation of Machine Learning Applications in Health Care Organizations: Systematic Review of Empirical Studies. *Journal of medical Internet research.* 2024;26:e55897.

[103] McIntosh Chris, Conroy Leigh, Tjong Michael C., et al. Clinical integration of machine learning for curative-intent radiation treatment of patients with prostate cancer *Nature Medicine 2021 27:6.* 2021;27:999-1005.

[104] Joshi Ameet V.. Machine Learning and Artificial Intelligence, Second Edition *Machine Learning and Artificial Intelligence, Second Edition.* 2022:1-271.

[105] Harrison Matt. *Machine Learning Pocket Reference: Working with Structured Data in Python.* Japan: O'Reilly Media 2019.

[106] Muraina Ibrahim. Ideal dataset splitting ratios in machine learning algorithms: general concerns for data scientists and data analysts in *7th International Mardin Artuklu Scientific Research Conference*:496–504 2022.

[107] Vujović . Classification model evaluation metrics *International Journal of Advanced Computer Science and Applications.* 2021;12:599-606.

[108] Aleem Ilyas S., Schemitsch Emil H., Hanson Beate P.. What is a clinical decision analysis study *Indian Journal of Orthopaedics.* 2008;42:137-139.

[109] Pauker Stephen G., Kassirer Jerome P.. The threshold approach to clinical decision making *New England Journal of Medicine.* 1980;302:1109-1117.

[110] Altkorn Diane. The threshold model: conceptualizing probabilities | symptom to diagnosis: an evidence-based guide, 4e | accessmedicine | McGraw Hill Medical 2020.

[111] Hoo Zhe Hui, Candlish Jane, Teare Dawn. What is an ROC curve? *Emergency Medicine Journal.* 2017;34:357-359.

[112] Unal Ilker. Defining an optimal cut-point value in ROC analysis: an alternative approach *Computational and Mathematical Methods in Medicine.* 2017;2017:3762651.

[113] Florkowski Christopher M. Sensitivity, specificity, receiver-operating characteristic (ROC) curves and likelihood ratios: communicating the performance of diagnostic tests *The Clinical Biochemist Reviews.* 2008;29:S83.

[114] Nahm Francis Sahngun. Receiver operating characteristic curve: overview and practical use for clinicians *Korean Journal of Anesthesiology.* 2022;75:25-36.

[115] Polo Tatiana Cristina Figueira, Miot Hélio Amante. Use of ROC curves in clinical and experimental studies *Jornal Vascular Brasileiro.* 2020;19:e20200186.

[116] Carter Jane V., Pan Jianmin, Rai Shesh N., Galandiuk Susan. ROC-ing along: Evaluation and interpretation of receiver operating characteristic curves *Surgery (United States).* 2016;159:1638-1645.

[117] Kerem Çorbacıoğlu , Aksel Gökhan. Receiver operating characteristic curve analysis in diagnostic accuracy studies: A guide to interpreting the area under the curve value *Turkish Journal of Emergency Medicine.* 2023;23:195-198.

[118] Youden W. J.. Index for rating diagnostic tests *Cancer.* 1950;3:32-35.

[119] Taira Al V., Merrick Gregory S., Butler Wayne M., et al. Long-term outcome for clinically localized prostate cancer treated with permanent interstitial brachytherapy *International Journal of Radiation Oncology Biology Physics.* 2011;79:1336-1342.

[120] Voršilák Milan, Kolář Michal, Čmelo Ivan, Svozil Daniel. SYBA: Bayesian estimation of synthetic accessibility of organic compounds *Journal of Cheminformatics.* 2020;12:1-13.

[121] Canadian Cancer Society . Prostate cancer statistics 2023. Accessed February 15, 2024.

[122] Hayashi Narihiko, Izumi Koji, Sano Futoshi, et al. Ten-year outcomes of I125 low-dose-rate brachytherapy for clinically localized prostate cancer: a single-institution experience in Japan *World Journal of Urology.* 2015;33:1519-1526.

[123] Sanda Martin G., Dunn Rodney L., Michalski Jeff, et al. Quality of life and satisfaction with outcome among prostate-cancer survivors *New England Journal of Medicine.* 2008;358:1250-1261.

[124] Thaker Nikhil G., Pugh Thomas J., Mahmood Usama, et al. Defining the value framework for prostate brachytherapy using patient-centered outcome metrics and time-driven activity-based costing *Brachytherapy.* 2016;15:274-282.

[125] Blanchard Pierre, Davis John W., Frank Steven J., et al. Quality of life after brachytherapy or bilateral nerve-sparing robot-assisted radical prostatectomy for prostate cancer: a prospective cohort *BJU International.* 2018;121:540-548.

[126] Nath Ravinder, Bice William S., Butler Wayne M., et al. AAPM recommendations on dose prescription and reporting methods for permanent interstitial brachytherapy for prostate cancer: Report of Task Group 137 *Medical Physics.* 2009;36:5310-5322.

[127] Yu Yan, Anderson Lowell L., Li Zuofeng, et al. Permanent prostate seed implant brachytherapy: Report of the American Association of Physicists in Medicine Task Group No. 64 *Medical Physics.* 1999;26:2054-2076.

[128] Kupelian Patrick A., Langen Katja M., Zeidan Omar A., et al. Daily variations in delivered doses in patients treated with radiotherapy for localized prostate cancer *International Journal of Radiation Oncology Biology Physics.* 2006;66:876-882.

[129] Chen Lili, Paskalev Kamen, Xu Xiu, et al. Rectal dose variation during the course of image-guided radiation therapy of prostate cancer *Radiotherapy and Oncology.* 2010;95:198-202.

[130] Peng Cheng, Ahunbay Ergun, Chen Guangpei, Anderson Savannah, Lawton Colleen, Li X. Allen. Characterizing interfraction variations and their dosimetric effects in prostate cancer radiotherapy *International Journal of Radiation Oncology Biology Physics.* 2011;79:909-914.

[131] Thor Maria, Bentzen Lise, Hysing Liv B., et al. Prediction of rectum and bladder morbidity following radiotherapy of prostate cancer based on motion-inclusive dose distributions *Radiotherapy and Oncology.* 2013;107:147-152.

[132] Wahl Michael, Descovich Martina, Shugard Erin, et al. Interfraction anatomical variability can lead to significantly increased rectal dose for patients undergoing stereotactic body radiotherapy for prostate cancer *Technology in Cancer Research and Treatment.* 2017;16:178-187.

[133] Smith Ryan P., Beriwal Sushil, Komanduri Krishna, Gibbons Erin, Benoit Ronald. Planning based on postneedle volume with early dosimetric assessment is beneficial for Cesium-131 permanent prostate seed implantation *Brachytherapy.* 2008;7:237-241.

[134] Chira Ciprian, Delouya Guila, Larrivée Sandra, Carrier Jean Francois, Taussky Daniel. Prostate volume changes during permanent seed brachytherapy: an analysis of intra-operative variations, predictive factors and clinical implication *Radiation Oncology (London, England).* 2013;8:177.

[135] Yin Jingjing, Tian Lili. Joint confidence region estimation for area under ROC curve and Youden index *Statistics in Medicine.* 2014;33:985-1000.

[136] Talavera Jesus E., Torres-Malca Jenny Raquel. Diagnostic performance of lipid accumulation indices and triglyceride and glucose index for metabolic syndrome in a sample of Peruvian adult population. *Revista de la Facultad de Medicina Humana.* 2021;22:42-49.

[137] Wang Jianhua, Chen Zeguo, Wang Liheng, et al. A new model based inflammatory index and tumor burden score (TBS) to predict the recurrence of hepatocellular carcinoma (HCC) after liver resection *Scientific Reports 2022 12:1.* 2022;12:1-11.

[138] Hicks Steven A., Strümke Inga, Thambawita Vajira, et al. On evaluation metrics for medical applications of artificial intelligence *Scientific Reports.* 2022;12.

[139] Su Yi, Davis Brian J., Furutani Keith M., Herman Michael G., Robb Richard A.. Dosimetry accuracy as a function of seed localization uncertainty in permanent prostate brachytherapy: Increased seed number correlates with less variability in prostate dosimetry *Physics in Medicine and Biology.* 2007;52:3105-3119.

[140] Morris W. James, Spadinger Ingrid, Keyes Mira, Hamm Jeremy, McKenzie Michael, Pickles Tom. Whole prostate D90 and V100: A dose-response analysis of 2000 consecutive 125I monotherapy patients *Brachytherapy.* 2014;13:32-41.

[141] Todor Dorin A., Anscher Mitchell S., Hagan Michael P.. Examining the relationship between pre- and postimplant geometry in prostate low-dose-rate brachytherapy and its correlation with dosimetric quality using the similarity concept *Brachytherapy.* 2014;13:471-480.

[142] Canadian Cancer Society . Cervical cancer statistics 2025. Accessed January 18, 2025.

[143] Franzese Ciro, Tomatis Stefano, Bianchi Sofia Paola, et al. Adaptive volumetric-modulated arc radiation therapy for head and neck cancer: evaluation of benefit on target coverage and sparing of organs at risk *Current Oncology 2023, Vol. 30, Pages 3344-3354.* 2023;30:3344-3354.

[144] Nagarajan M, Banu R, Sathya B, Sundaram T, Chellapandian TP. Dosimetric evaluation and comparison between volumetric modulated arc therapy (VMAT) and intensity modulated radiation therapy (IMRT) plan in head and neck cancers. *The Gulf Journal of Oncology.* 2020:45-50.

[145] Grégoire Vincent, Guckenberger Matthias, Haustermans Karin, et al. Image guidance in radiation therapy for better cure of cancer *Molecular Oncology.* 2020;14:1470-1491.

[146] Jadon R., Pembroke C. A., Hanna C. L., et al. A systematic review of organ motion and image-guided strategies in external beam radiotherapy for cervical cancer *Clinical Oncology.* 2014;26:185-196.

[147] Yan Huamei, Wu Manya, Wang Wan, et al. Dosimetry and acute radiation enteritis comparison between prone and supine position in IMRT for gynecological cancers *Journal of Applied Clinical Medical Physics.* 2023;24:e14135.

[148] Boisbouvier S., Boucaud A., Tanguy R., Grégoire V.. Upright patient positioning for pelvic radiotherapy treatments *Technical Innovations and Patient Support in Radiation Oncology.* 2022;24:124-130.

[149] Bell James P., Patel Pretesh, Higgins Kristin, McDonald Mark W., Roper Justin. Fine-tuning the normal tissue objective in eclipse for lung stereotactic body radiation therapy *Medical Dosimetry.* 2018;43:344-350.

[150] Indrayani Liza, Anam Choirul, Sutanto Heri, Subroto Rinarto, Dougherty Geoff. Normal tissue objective (NTO) tool in Eclipse treatment planning system for dose distribution optimization *Polish Journal of Medical Physics and Engineering.* 2022;28:99-106.

[151] Serarslan Alparslan, Aksu Telat, Daştan Yalçın, et al. Normal tissue objective tool in radiotherapy planning for endometrial cancer: a dosimetric study *Turkish Journal of Oncology.* 2024;39:167-175.

[152] Athulya P., Manna S., Singh S.. Assessment of normal tissue objectives in RapidArc treatment for cervical cancer *Journal of Radiotherapy in Practice.* 2024;23:e14.

[153] Caldeira Ademar, Trinca William Correia, Flores Thais Pires, et al. The influence of normal tissue objective in the treatment of prostate cancer *Journal of Medical Imaging and Radiation Sciences.* 2020;51:312-316.

[154] indrayani , Anam Choirul, Sutanto Heri, Subroto Rinarto. Determination of optimal normal tissue objective settings for radiation therapy planning of brain tumor *International Journal of Progressive Sciences and Technologies.* 2022;31:61-69.

[155] Grams Michael P., Owen Dawn, Park Sean S., et al. VMAT grid therapy: a widely applicable planning approach *Practical Radiation Oncology.* 2021;11:e339-e347.

[156] Huang B., Fang Z., Huang Y., Lin P., Chen Z.. A dosimetric analysis of volumetric-modulated arc radiotherapy with jaw width restriction vs 7 field intensity-modulated radiotherapy for definitive treatment of cervical cancer *The British Journal of Radiology.* 2014;87:20140183.

[157] Sharfo Abdul Wahab M., Voet Peter W.J., Breedveld Sebastiaan, Mens Jan Willem M., Hoogeman Mischa S., Heijmen Ben J.M.. Comparison of VMAT and IMRT strategies for cervical cancer patients using automated planning *Radiotherapy and Oncology.* 2015;114:395-401.

[158] Narayanasamy Ganesh, Desai Dharmin, Maraboyina Sanjay, Penagaricano Jose, Zwicker Robert, Johnson Ellis. A dose falloff gradient dtudy in rapidarc planning of lung stereotactic body radiation therapy *Journal of Medical Physics.* 2018;43:147.

[159] Ishibashi Akihiko, Kurosaki Hiromasa, Miura Kosei, Utsumi Nobuko, Sakurai Hideyuki. Influence of modulation factor on treatment plan quality and irradiation time in hippocampus-sparing whole-brain radiotherapy using tomotherapy *Technology in Cancer Research Treatment.* 2021;20:15330338211045497.

[160] Sandison G.A., Lehnert A., Miyaoka R.S., et al. A novel approach to support quality assurance (QA) of intensity modulated neutron therapy (IMNT) *International Journal of Radiation Oncology*Biology*Physics.* 2023;117:e714.

[161] Lee Jonny, Dean Christopher, Patel Rushil, Webster Gareth, Eaton David J.. Multi-center evaluation of dose conformity in stereotactic body radiotherapy *Physics and Imaging in Radiation Oncology.* 2019;11:41.

[162] Muthukumar S, Navitha S, Nigam J, Silambarasan N, Kumar P. Impact on undefined normal tissue by using different combination of normal tissue objective and dose control ring in IMRT plans for cervix cancer *International Journal of Medical Research and Review.* 2022;10:69-74.

[163] Tol Jim P., Dahele Max, Peltola Jarkko, Nord Janne, Slotman Ben J., Verbakel Wilko F.A.R.. Automatic interactive optimization for volumetric modulated arc therapy planning *Radiation Oncology.* 2015;10:1-12.

[164] Banaei Amin, Hashemi Bijan, Bakhshandeh Mohsen, Mofid Bahram. Trade-off between the conflicting planning goals in correlation with patient's anatomical parameters for intensity-modulated radiotherapy of prostate cancer patients *Journal of Radiotherapy in Practice.* 2019;18:232-238.

[165] Wang Hanlin, Wang Ruoxi, Liu Jiacheng, et al. Tree-based exploration of the optimization objectives for automatic cervical cancer IMRT treatment planning *The British Journal of Radiology.* 2021;94:20210214.

[166] Mohamadian Niloofar, Nasseri Shahrokh, Hosseini Sare, et al. Dosimetric impact of bladder volume on organs at risk during external beam radiotherapy of cervical cancer *Radiation Protection Dosimetry.* 2023;199:1351-1356.

[167] Hwang Woo Yeon, Kim Ju Hyun, Suh Dong Hoon, Kim Kidong, No Jae Hong, Kim Yong Beom. The upper limit of optimal tumor size in patients with FIGO 2018 stage IB2 cervical cancer undergoing radical hysterectomy *International Journal of Gynecological Cancer.* 2020;30:975-980.

[168] Lee Kyu Chan, Kim Hun Jung, Sung Kihoon, et al. The Predictive Value of Tumor Size, Volume, and Markers during Radiation Therapy in Patients with Cervical Cancer *International Journal of Gynecological Cancer.* 2017;27:123-130.